Democratic and Popular Republic of Algeria

Ministry of High Education and Scientific Research

Ferhat Abbas University - Setif 1

THESIS

Presented at Faculty of Sciences

Department of Physics

To obtain the degree of

Doctor of Science

Option: Materials Physics

By

KHIREDDINE Abderrazek

Title

Ab initio study of physical properties of some solid materials

Discussed publicly at 27/04/2024 with the board of examiners:

Mr. T. CHIHI	Professor	Univ. F. Abbas Setif 1	Chairman
Mr. A. BOUHEMADOU	Professor	Univ. F. Abbas Setif 1	Supervisor
Mr. N. GUCHI	Professor	Univ. F. Abbas Setif 1	Co-supervisor
Mr. S. SAAD ESSAOUD	M.C.A	Univ. M. Boudiaf M'sila	Examiner
Mr. M. RADJAI	M.C.A	Univ. Y. Fares Medea	Examiner
Mr. D. ALLALI	M.C.A	Univ. M. Boudiaf M'sila	Examiner


بسم الله الرحمن الرحيم

الملخص

تمت دراسة الخواص البنيوية، الالكترونية، الضوئية، المرونية و الكهروحرارية لمواد زنتل الثلاثية Sr_3GaAs_3 و Ba_3GaAs_3 و Ba_2ZnP_2 باستعمال طريقتين متكاملتين من طرق المبادئ الأولى في الحساب هما طريقة الأمواج المستوية مع الكمون الكاذب (PP-PW) و طريقة الأمواج المستوية المزادة خطياً مع الكمون الكامل (FP-LAPW) في إطار نظرية دالية الكثافة. يتبلور المركبين Sr_3GaAs_3 و Ba_3GaAs_3 في بنية معينية قائمة، الزمرة الفضائية Pnma (رقم 62 في الجداول البلورية)، بينما يتبلور Ba_2ZnP_2 في بنية معينية قائمة، الزمرة الفضائية Ibam (رقم 72 في الجداول البلورية). استعملت ال GGA-PBEsol لمعالجة كمون التبادل و الترابط (XC) لحساب الخواص البنيوية و الميكانيكية. و استعملت الGGA-PBEsol اضافة إلى ال TB-mBJ في دراسة الخواص الإلكترونية والضوئية. تتوافق قيم معاملات البنية البلورية (ثوابت الشبكة البلورية و حجم الخلية الاساسية) المحسوبة للحالة الاساسية مع النتائج التجريبية المتوفرة. مما يشير إلى موثوقية نتائجنا. لقد قدرنا عدديًا ثوابت المرونة والخواص المرتبطة بها (ثوابت المرونة C_{ij}، معامل يونغ E، معامل القص G، معامل بواسون σ و درجة حرارة ديباي θ_D) لأحادي البلورة و متعدد البلورات تحت الضغط المعدوم و سرعات الصوت المتباينة الخواص. بينت نتائج الحسابات أن المواد المدروسة تنتمي لعائلة أنصاف النواقل بموانع طاقة أساسية مباشرة للمركبين Sr_3GaAs_3 و Ba_3GaAs_3 قيمتهما 1.271 إلكترون فولت و 1.285 إلكترون فولت على التوالي، ومانع طاقي أساسي غير مباشر قيمته 1.24 إلكترون فولت ل-Ba_2ZnP_2. قمنا بتحليل الحالات الإلكترونية لنطاقات الطاقة باستخدام مخططات كثافة الحالات الجزئية. تم حساب الثوابت الضوئية في مجال طاقوي من 0 إلى 30 إلكترون فولت. بينت نتائج الحسابات تزايد ثابت العزل الساكن $\varepsilon_1(0)$ مع تناقص موانع الطاقة للمركبات المدروسة. تمت دراسة الثوابت الكهروحرارية للمركبات باستعمال نظرية النقل بولتزمان شبه-الكلاسيكية. تشير نتائجنا إلى أن Ba_2ZnP_2 يتمتع بأفضل رقم جدارة (ZT) بلغ 1.77 عند 300 كلفن، مما يجعله مرشحًا محتملاً للتطبيقات الكهروحرارية.

الكلمات المفتاحية: نظرية دالية الكثافة (DFT)، مركبات زنتل الثلاثية، حسابات المبادئ الأولى (ab initio) ؛ الهيكلة الإلكترونية، الكتل الفعالة، الخصائص الكهروضوئية، ثوابت المرونة، المعاملات الكهروحرارية.

Abstract

The structural, electronic, optical, elastic and thermoelectric properties of the ternary Zintl compounds Sr_3GaAs_3, Ba_3GaAs_3 and Ba_2ZnP_2 were studied using two complementary first-principles calculation methods, the pseudopotentials plane waves (PP-PW) and the full potential Linearized Augmented Plane wave (FP-LAPW) methods within the density function theory framework. Sr_3GaAs_3 and Ba_3GaAs_3 crystallize in an orthorhombic system, space group Pnma (no 62), while Ba_2ZnP_2 crystallizes in an orthorhombic system, space group Ibam (no 72). GGA-PBEsol was used to treat the exchange and correlation potential (XC) to calculate the structural and elastic properties. GGA-PBEsol and TB-mBJ were used to study its electronic and optical properties. The values of structural parameters (the parameters and volume of primitive cell) calculated agreed well with available experimental data. This indicates the reliability of our results. We have numerically estimated the elastic constants and associated properties (elastic constants C_{ij}, Young's modulus E, shear modulus G, Poisson's modulus σ and Debye temperature θ_D) for single-crystal and polycrystalline under zero pressure and anisotropic sound velocities. The calculation results showed that the studied compounds belong to the semiconductor family, with direct band gaps for the compounds Sr_3GaAs_3 and Ba_3GaAs_3, valued at 1.271 eV and 1.285 eV, respectively, and an indirect band gap energy with a value of 1.24 eV for Ba_2ZnP_2. We analysed the electronic states of the energy bands using partial density diagrams of states. Optical constants were calculated in an energy range from 0 to 30 MeV. The results of the calculations showed an increase in the static dielectric constant $\varepsilon_1(0)$ with a decrease in the energy impedances of the studied compounds. The thermoelectric constants of the compounds were studied using semi-classical Boltzmann transport theory. Our results indicate that Ba_2ZnP_2 has a best figure of merit (ZT) of 1.77 at 300 K, making it a potential candidate for thermoelectric applications.

Keywords: Density functional theory (DFT); Ternary Zintl phases; First-principles (ab initio) calculations; Electronic structure; Effective masses; Optoelectronic properties; Elastic constants; Thermoelectric coefficients.

Résumé

Les propriétés structurelles, électroniques, optiques, élastiques et thermoélectriques des composés ternaires Zintl Sr_3GaAs_3, Ba_3GaAs_3 et Ba_2ZnP_2 ont été étudiées à l'aide de deux méthodes de calcul complémentaires de principes premiers, les ondes planes pseudo potentielles (PP-PW) et l'onde plane augmentée linéarisée à plein potentiel (FP-LAPW) dans le cadre de la théorie de la fonction de densité. Sr_3GaAs_3, Ba_3GaAs_3 cristallisent dans un système orthorhombique, groupe spatial Pnma (no 62), tandis que Ba_2ZnP_2cristallise dans un système orthorhombique, groupe spatial Ibam (no 72). GGA-PBEsol a été utilisé pour traiter le potentiel d'échange et de corrélation (XC) afin de calculer les propriétés structurelles et élastiques. GGA-PBEsol et TB-mBJ ont été utilisés pour étudier ses propriétés électroniques et optiques. Les valeurs des paramètres structurels (les paramètres et le volume de la cellule primitive) calculées concordaient bien avec les données expérimentales disponibles. Cela indique la fiabilité de nos résultats. Nous avons estimé numériquement les constantes élastiques et les propriétés associées (constantes élastiques Cij, module d'Young E, module de cisaillement G, module de Poisson σ et température de Debye θ_D) pour les monocristallin et polycristallins sous pression nulle et vitesses sonores anisotropes. Les résultats des calculs ont montré que les composés étudiés appartiennent à la famille des semi-conducteurs, avec des bandes interdites directes pour les composés Sr_3GaAs_3, Ba_3GaAs_3, évaluées respectivement à 1.271 eV et 1.285 eV, et une énergie de bande interdite indirecte d'une valeur de 1,24 eV pour Ba_2ZnP_2. Nous avons analysé les états électroniques des bandes d'énergie à l'aide de diagrammes de densité partielle d'états. Les constantes optiques ont été calculées dans une plage d'énergie de 0 à 30 MeV. Les résultats des calculs ont montré une augmentation de la constante diélectrique statique $\varepsilon_1(0)$ avec une diminution des impédances énergétiques des composés étudiés. Les constantes thermoélectriques des composés ont été étudiées à l'aide de la théorie semi-classique du transport de Boltzmann. Nos résultats indiquent que Ba_2ZnP_2 a un meilleur facteur de mérite (ZT) de 1.77 à 300 K, ce qui en fait un candidat potentiel pour les applications thermoélectriques.

Mots-clés: Théorie de la fonctionnelle de la densité (DFT); Phases ternaires de Zintl; Calculs de première-principes (ab initio); Structure électronique; Masses effectives; Propriétés optoélectroniques; Constantes élastiques; Coefficients thermoélectriques

تشكرات

الحمد لله رب العالمين والصلاة والسلام على من أرسله الله رحمة للعالمين وعلى آله وصحبه وإخوانه إلى يوم الدين، أما بعد:

فنحمد الله ونشكره على منه وإكرامه -ونعمه لا تحصى، قال عز من قائل **" وإن تعدوا نعمة الله لا تحصوها"**- إذ وفقني إلى هذا العمل العلمي وأعانني عليه وأسأله عز وجل أن يتقبله مني ويضع له القبول في الأرض وأن ينفع به غيري من الطلاب وأن يجعله ذخرا لي يوم لقائه، أنه ولي ذلك والقادر عليه.

ثم أتقدم بالشكر الجزيل إلى أستاذي الفاضل **بوحمادو عبد المجيد** -أستاذ باحث بجامعة فرحات عباس 1- على إشرافه و تأطيره لهذا العمل ومتابعته طول فترة التكوين وتحمل التقصير مني صابرا على بناء طلبة على أسس صحيحة متفوقين في الفيزياء الحسابية، إذ قال رسول الله صلى الله عليه وسلم **" لا يشكر الله من لا يشكر الناس"**.

كما أتقدم بالشكر إلى الأستاذ **قشي نصير** الذي كان مساعدا لي في إنجاز العمل واللجنة التي تشرفت بمناقشة مذكرتي برئاسة **شيحي الطيب** والأساتذة الممتحنون **ساعد سعود صابر و علالي جمال ميسوم راجي**

ولا أنسى أن أوجه الشكر إلى **والدي العزيزين** الذين كان لهما الفضل الأول بعد الله في جميع مسيراتي العلمية، وإلى كل من مد لي يد العون الحسي أو المعنوي في إتمام هذا العمل المتواضع من العائلة الصغيرة (**زوجتي**) والكبيرة والزملاء والأصدقاء.

وآخر دعونا أن الحمد لله رب العالمين، وصلى الله على نبينا محمد وعلى آله وصحبه وإخوانه إلى يوم الدين، وسلم تسليما.

Research Activities

International Publications

1- First-principles predictions of the structural, electronic, optical and elastic properties of the Zintl-phases AE_3GaAs_3 (AE = Sr, Ba) Solid State Sci. 114 (2021) 1-12.

2- Elastic, electronic, optical and thermoelectric properties of the novel Zintl-phase Ba_2ZnP_2 Solid State Sci. 128 (2022) 106893.

International Communications

1- First-principles predictions of the electronic, optical and thermoelectric properties of the new Zintl-phase Sr_2CdAs_2 ICCAP Blida Algeria 26-28 September 2021.

2- First-principles predictions of the electronic, optical and thermoelectric properties of the new Zintl-phase Ba_2CdAs_2 ICTN-KLC New Delhi India 22-24 August 2021.

Abbreviations

Ab initio: A Latin term that translates to "from the beginning" in English, it is mean **First Principles**

AM05: Armiento-Mattsson 2005

B86, B88: Becke

BFGS: Broyden-Fletcher-Goldfarb-Shannon

BJ: Becke and Johnson

BLYP: Becke exchange and Lee-Yang-Parr correlation

BZ: Brillouin zone

CAM: Laming-Termath-Handy

CBM: Conduction band minimum

CFCs: Chlorofluorocarbons

COHP: Crystal Orbital Hamilton Population

CSTA: Constant scattering time approximation

DFT: Density functional theory

DOS: Density of states

DP: Deformation potential

FP-L/APW + lo: Full-potential linearized/augmented plane wave plus local orbitals

GGA-PBE, GGA96: Generalized Gradient Approximation Perdew-Burke-Ernzerhof

GGA-PBEsol, GGA08: Generalized Gradient Approximation Perdew-Burke-Ernzerhof revised for solids

HEG: Homogeneous electron gas

HP: Hartree Product

KS-DFT: Kohn-Sham density-functional theory

LDA: Local density approximation

mBJ: modified Becke-Johnson

m_h^*, m_e^***:** Hole effective mass and electron effective mass

P86: Perdew 86

PBE: Perdew-Burke-Ernzerhof

PBEsol: Perdew-Burke-Ernzerhof revised for solids

PDOS: partial density of states

PP-PW: Pseudopotential plane-wave

PW91: Perdew-Wang 91

RPBE: revised Perdew-Burke-Ernzerhof

TB-LMTO: Tight-binding linear muffin-tin orbital

TB-mBJ: Tran- Blaha modified Becke-Johnson

TDOS: Total density of states

TE: Thermoelectric

TF: Thomas and Fermi model

VBM: Valence band maximum

XC: Exchange correlation

ZT: Figure of merit

Contents of summary

CHAPTER 2: PSEUDOPOTENTIAL PLANE-WAVE METHOD

CHAPTER 3
FULL-POTENTIAL LINEARIZED AUGMENTED PLANE-WAVE METHOD

PART 2
RESULTS AND DISCUSSION

CHAPTER 1
THE STRUCTURAL, ELECTRONIC, ELASTIC, OPTICAL AND THERMOELECTRIC PROPERTIES OF THE ZINTL-PHASES AE_3GaAs_3 (AE = Sr, Ba)

CHAPTER 2
THE STRUCTURAL, ELECTRONIC, ELASTIC, OPTICAL AND THERMOELECTRIC PROPERTIES OF THE ZINTL-PHASE Ba_2ZnP_2

List of figures

Part 1

Chapter 1

Chapter 2

Chapter 3

Part 2

Chapter 1

Chapter 2

List of Tables

Part 2

Chapter 1

Chapter 2

GENERAL INTRODUCTION

1. Preamble

Physical properties of solid materials include mechanical, thermal, electrical, magnetic, optical properties, and many others. These are essential in determining the suitability of a material for a particular application. For example, mechanical properties such as elasticity, strength, and hardness are critical in the design of materials for engineering applications, including construction, aerospace, and automotive industries. Thermal properties such as thermal conductivity and specific heat are critical in the design of materials for heat transfer applications. Electrical and magnetic properties of solid materials are essential in designing materials for electronic and magnetic applications, such as magnetic refrigeration devices [1], magnetic resistors. Optical properties such as refractive index, absorption, and reflection are crucial in designing materials for optical applications, including lenses, mirrors, and fibre optics.

The study of physical properties of solid materials is essential in the development of new materials with improved properties and applications. It enables researchers to understand the fundamental principles that govern the behaviour of materials under different conditions, which is critical in the design of new materials for specific applications. The advancements in technology have led to the development of new materials with unique physical properties. The study of physical properties of these materials has opened up new frontiers in various fields, including renewable energy, biomedicine, and electronics. For example, the discovery of materials with high-temperature superconductivity has led to the development of new technologies that could revolutionize energy transmission and storage and a some of discoveries related to material properties are driven by the objective of enhancing the efficiency, performance, and, notably, the environmental and health aspects of devices, while also extending their lifespan.

In summary, the study of physical properties of solid materials is of critical importance in understanding the fundamental principles that govern the behaviour of materials under different conditions. It is essential in the design of new materials with improved properties and applications, which has significant implications in various fields, including engineering, materials science, physics, chemistry, and many others.

Solids' physical properties are closely related to the behavior of their electrons. As a result, the primary goal of condensed matter theory is to solve the problem of solid electronic structure. The theory of electronic structure is useful for understanding and interpreting experimental results, as well as for prediction. Theorists have developed semi-empirical

models to gain a fundamental understanding of electronic structure and thus material properties. Such models frequently include a large number of parameters that can be adjusted based on experimental data. Other methods of calculation that are more rigorous and sophisticated are ab initio methods, which are based on fundamental quantum theory and use only atomic constants as input parameters to solve the Schrödinger equation. These methods are now used to study structural, electronic, mechanical, and optical properties of atoms, molecules, and materials. They are also an excellent tool for studying specific effects that are difficult or impossible to determine experimentally such as very high temperature and pressure, as well as for predicting new materials, and they can sometimes replace costly or even impossible experiments in the laboratory. The power of ab-initio calculations stems from the density functional theory (DFT) formalism and its two-exchange energy and correlation approximations: the local density approximation (LDA) and the generalized gradient approximation (GGA). The basic formalism of the DFT is based on Hohenberg and Kohn's (1964) theorem [2], which states that the total energy of a system is a functional of the electron density. Density Functional Theory (DFT) is a powerful theoretical framework used to study the physical properties of materials. DFT is a quantum mechanical approach that allows for the prediction of properties such as electronic structure, atomic and molecular interactions, and the thermodynamics of materials. It has revolutionized the field of material science by providing a way to study the behavior of materials at the atomic and molecular level. One of the major advantages of DFT is that it is computationally efficient and allows for the investigation of large systems, such as complex molecules and nanoparticles, which would be impossible to study experimentally. By using DFT, researchers can understand the structure and properties of materials on a microscopic scale, which is essential for designing new materials with specific properties. DFT has been used to study a wide range of materials, from metals and semiconductors to organic compounds and biological molecules. It has provided insight into the properties of materials such as their electronic structure, bonding, and reactivity, and has led to the discovery of new materials with unique properties. For example, DFT was used to predict the properties of graphene, a two-dimensional material with remarkable electrical and mechanical properties, long before it was ever synthesized.

In conclusion, DFT is a fundamental tool for the study of materials science, providing researchers with a way to understand the properties of materials at the atomic and molecular level. Its impact has been significant, leading to new discoveries and advances in the field of materials science, and it will continue to be an essential tool in the design and development of new materials with specific properties.

2. Statement of the problem and objectives of the thesis

In recent years, there has been significant interest among energy researchers in the development and application of new and renewable energy sources [3-8]. The latter hold a key position in combating environmental pollution, improving the global economy, and offering various advantages compared to other direct current power sources. One such renewable energy is thermoelectricity, which involves the conversion of heat into electricity (Seebeck effect 1821 [9]) and electricity into cold (Peltier effect 1834) [10]. Materials involved in this process are referred to as thermoelectric (TE) materials. One of the most significant compounds used to achieve this objective are thermoelectric (TE) materials, which are applied to power generation and device cooling to phase out chlorofluorocarbons (CFCs) and exploit low-level waste heat. TE materials generate electricity from thermal energy (heat) with high efficiency. When two ends of a conductor are at different temperatures, they produce a voltage difference between the two substances, resulting in an electric current (Seebeck effect 1821, also known as a Seebeck generator) [9]. The heat drives the free carriers (electrons in the n-type or holes in the p-type) to cold points, while the reverse phenomenon (Peltier effect 1834) [10] is used in device cooling (heat pumps).

Zintl phases are a promising class of chemical compounds for thermoelectric (TE) applications due to their high efficiency. Typically, they are composed of alkali or alkaline-earth (s-block) and post-transition (d-block) elements, or other metals or semimetals (p-block), where the most electronegative element takes the valence electrons of the more electropositive elements within to create a covalent bond that satisfies the octet rule. Binary compounds consist of polyionic structures, while ternary, quaternary, and even quinary compounds can have a metal, semimetal, or small-gap semiconductor structure. Eduard Zintl [11] was the first to establish this concept, which was later expanded by William Klemm [12]. However, the non-classical Zintl concept involves complex compounds between transition and rare-earth elements, with both ionic and covalent bonds playing a role in the structural requirements of this concept [13].

Newly synthesized Zintl phases exhibit a wide range of interesting physical properties such as thermoelectricity [14], metallic/semi-metallic superconductivity [15]; magnetic order [16], semiconductor colossal natures [17], magnetoresistance [18], photovoltaics [14], energy storage [19], energy conversion [20], energy-related applications, and mixed-valence [21], among others. Zintl compounds are still being developed through scientific research to

improve their figure of merit ZT in thermoelectric applications. The best-performing Zintl compounds with ZT>1 have been observed in various materials such as $Yb_{14}MnSb_{11}$ [22], $Ca_5Al_2Sb_6$ [13], and $Ba_8Ga_{16}Ge_{30}$ [23], among others. Recently, Stoyko et al, [24] reported on the synthesis and crystal structures of the ternary gallium-arsenide Zintl phases Sr_3GaAs_3 and Ba_3GaAs_3, with a preliminary ab initio calculation of the band structure of Ba_3GaAs_3 revealing its semiconducting nature. However, there are no prior reports on in-depth theoretical or experimental studies of the basic physical properties of the AE_3GaAs_3 (AE = Sr, Ba) compounds, such as elastic constants, charge carrier effective masses, optical properties, and anisotropy of physical properties, except for Stoyko et al.'s work. Therefore, the present study aims to conduct a comprehensive investigation of the structural, electronic, optical, and elastic properties of Sr_3GaAs_3 and Ba_3GaAs_3 using density functional theory (DFT)-based first-principles calculations for both fundamental physics and application perspectives. The study also aims to assess the potential applications of these Zintl phases.

Furthermore, a novel Zintl compound, dibarium zinc diphosphide (Ba_2ZnP_2), has been synthesized for the first time by A. Balvanz et al [25].Using the Pb flux technique. This compound crystallizes under the K_2SiP_2 structure type (orthorhombic, space group *Ibma* no. 72), and its electronic properties were calculated using the tight-binding linear muffin-tin orbital (TB-LMTO) method within DFT framework with local density approximation (LDA), revealing its semiconducting nature. However, there is no literature on the physical properties of Ba_2ZnP_2, except for its band structure within electronic structures of band engineering strategies for Ba_2CdP_2 in Supporting Information, based on the Yb_2CdSb_2 structure type. Therefore, this study is dedicated to investigating the structural, elastic, optical, and thermoelectric properties of Ba_2ZnP_2 via DFT calculations, with a focus on its potential applications. The main goal of computational physics is to identify materials that are worthy of experimental research and to evaluate their potential for applications.

3. Organization of the thesis

The thesis is structured as follows:

- The first part includes the theoretical framework containing three chapters, the first provides an overview of ab-initio calculations methods and discusses single particle self-consistent field methods, namely Hartree and Hartree-Fock, as approximations of the multi-body Schrödinger equation. The Hohenberg-Kohn-Sham formulation of the functional theory of density is also introduced. The second and third chapters related the details of the pseudopotential plane-wave and the full-potential linearized/augmented plane wave plus local orbitals methods, respectively.
- The second part includes the chapters one and two and will concentrate on the computational tools used in this study, namely the pseudopotential plane-wave (PP-PW) method with the GGA-PBEsol functional for treating exchange-correlation effects, as implemented in the CASTEP code, and the full-potential linearized/augmented plane wave plus local orbitals (FP-L/APW + lo) method with both the GGA-PBEsol and Tran-Blaha modified Becke-Johnson (TB-mBJ) potential, as implemented in the WIEN2k package. The results of the calculations, which determine the properties of the ternary Zintl phases gallium arsenides (AE_3GaAs_3, AE= Sr, Ba) and the dibarium zinc diphosphide (Ba_2ZnP_2), are presented.
- Finally, the Conclusion chapter summarizes the work, and the results of the calculations that determine the structural, elastic, electronic, optical, and thermoelectric properties of Sr_3GaAs_3, Ba_3GaAs_3, and Ba_2ZnP_2 are presented.

References

[1] R. Bjørk, C. R. H. Bahl, A. Smith, N. Pryds, Review and comparison of magnet designs for magnetic refrigeration, *Int. J. Refrig.* vol 33 2010, pp 437-448. doi.org/10.1016/j.ijrefrig.2009.12.012

[2] V. Sahni, "The Hohenberg-Kohn Theorems and Kohn-Sham Density Functional Theory," in *Quantal Density Functional Theory*, V. Sahni, Ed., Berlin, Heidelberg: Springer, 2004, pp. 99–123. doi: 10.1007/978-3-662-09624-6_4.

[3] Z.-G. Chen, G. Han, L. Yang, L. Cheng, and J. Zou, "Nanostructured thermoelectric materials: Current research and future challenge," *Prog. Nat. Sci. Mater. Int.*, vol. 22, no. 6, pp. 535–549, Dec. 2012, doi: 10.1016/j.pnsc.2012.11.011.

[4] A. Bejan, *Advanced engineering thermodynamics*, Fourth edition. Hoboken, New Jersey: John Wiley & Sons Inc, 2016.

[5] V. K. Gupta, G. Shanker, B. Saraf, and N. K. Sharma, "Experiment to verify the second law of thermodynamics using a thermoelectric device," *Am. J. Phys.*, vol. 52, no. 7, pp. 625–628, Jul. 1984, doi: 10.1119/1.13582.

[6] R. Venkatasubramanian, E. S2vola, T. Colpitts, and B. O'Quinn, "Thin-film thermoelectric devices with high room-temperature figures of merit," *Nature*, vol. 413, no. 6856, Art. no. 6856, Oct. 2001, doi: 10.1038/35098012.

[7] B. C. Sales, "Smaller Is Cooler," *Science*, vol. 295, no. 5558, pp. 1248–1249, Feb. 2002, doi: 10.1126/science.1069895.

[8] L. Yan, M. Shao, H. Wang, D. Dudis, A. Urbas, and B. Hu, "High Seebeck Effects from Hybrid Metal/Polymer/Metal Thin-Film Devices," *Adv. Mater.*, vol. 23, no. 35, pp. 4120–4124, Sep. 2011, doi: 10.1002/adma.201101634.

[9] T. J. Seebeck, "Magnetic polarization of metals and minerals," *Abh. Dtsch. Akad. Wiss.*, vol. 265, 1823.

[10] J. C. Peltier, "Nouvelle experieces sur la caloricite des courans electrique," *Ann Chim*, vol. 371, 1834.

[11] E. Zintl, "Intermetallische Verbindungen," *Angew. Chem.*, vol. 52, no. 1, pp. 1–6, 1939, doi: 10.1002/ange.19390520102.

[12] W. Klemm, “Einige Probleme aus der Physik und der Chemie der Halbmetalle und der Metametalle,” *Angew. Chem.*, vol. 62, no. 6, pp. 133–142, 1950, doi: 10.1002/ange.19500620602.

[13] E. S. Toberer, A. Zevalkink, N. Crisosto, and G. J. Snyder, “The Zintl Compound $Ca_5Al_2Sb_6$ for Low-Cost Thermoelectric Power Generation,” *Adv. Funct. Mater.*, vol. 20, no. 24, pp. 4375–4380, 2010, doi: 10.1002/adfm.201000970.

[14] A. Khireddine, A. Bouhemadou, S. Maabed, S. Bin-Omran, R. Khenata, and Y. Al-Douri, “Elastic, electronic, optical and thermoelectric properties of the novel Zintl-phase Ba_2ZnP_2,” *Solid State Sci.*, vol. 128, p. 106893, Jun. 2022, doi: 10.1016/j.solidstatesciences.2022.106893.

[15] T. F. Fässler and C. Kronseder, “BaSn3: A Superconductor at the Border of Zintl Phases and Intermetallic Compounds. Real-Space Analysis of Band Structures,” *Angew. Chem. Int. Ed. Engl.*, vol. 36, no. 23, pp. 2683–2686, 1997, doi: 10.1002/anie.199726831.

[16] J. Jiang *et al.*, “Complex Magnetic Ordering in Eu_3InP_3: A New Rare Earth Metal Zintl Compound,” *Inorg. Chem.*, vol. 44, no. 7, pp. 2189–2197, Apr. 2005, doi: 10.1021/ic048507o.

[17] A. Khireddine *et al.*, “First-principles predictions of the structural, electronic, optical and elastic properties of the zintl-phases AE_3GaAs_3 (AE = Sr, Ba),” *Solid State Sci.*, vol. 114, p. 106563, Apr. 2021, doi: 10.1016/j.solidstatesciences.2021.106563.

[18] J. Y. Chan, S. M. Kauzlarich, P. Klavins, R. N. Shelton, and D. J. Webb, “Colossal Magnetoresistance in the Transition-Metal Zintl Compound Eu14MnSb11,” *Chem. Mater.*, vol. 9, no. 12, pp. 3132–3135, Dec. 1997, doi: 10.1021/cm9704241.

[19] J. Xie, L. Sun, Y. Liu, X. Xi, R. Chen, and Z. Jin, “SiOx/C-Ag nanosheets derived from Zintl phase $CaSi_2$ via a facile redox reaction for high performance lithium storage,” *Nano Res.*, vol. 15, no. 1, pp. 395–400, Jan. 2022, doi: 10.1007/s12274-021-3491-z.

[20] S. Baranets and S. Bobev, “$Ca_{14}AlBi_{11}$—a new Zintl phase from earth-abundant elements with a great potential for thermoelectric energy conversion,” *Mater. Today Adv.*, vol. 7, p. 100094, Sep. 2020, doi: 10.1016/j.mtadv.2020.100094.

[21] S. Margadonna, K. Prassides, M. Chondroudi, J. R. Salvador, and M. G. Kanatzidis, “Temperature-induced abrupt volume inflation in the mixed-valence ternary Zintl phase

$Yb_8Ge_3Sb_5$," *Chem. Commun.*, no. 46, pp. 5754–5756, Nov. 2005, doi: 10.1039/B511606F.

[22] S. R. Brown, S. M. Kauzlarich, F. Gascoin, and G. J. Snyder, "Yb $_{14}$ MnSb $_{11}$: New High Efficiency Thermoelectric Material for Power Generation," *Chem. Mater.*, vol. 18, no. 7, pp. 1873–1877, Apr. 2006, doi: 10.1021/cm060261t.

[23] Y.-H. Hou and L.-S. Chang, "Optimization on the figure-of-merit of P-type $Ba_8Ga_{16}Ge_{30}$ Type-I clathrate grown via the Bridgman method by fine tuning Ga/Ge ratio," *J. Alloys Compd.*, vol. 736, pp. 108–114, Mar. 2018, doi: 10.1016/j.jallcom.2017.11.059.

[24] S. S. Stoyko, L. H. Voss, H. He, and S. Bobev, "Synthesis, Crystal and Electronic Structures of the Pnictides AE_3TrPn_3 (AE = Sr, Ba; Tr = Al, Ga; Pn = P, As)," *Crystals*, vol. 5, no. 4, Art. no. 4, Dec. 2015, doi: 10.3390/cryst5040433.

[25] A. Balvanz, S. Baranets, and S. Bobev, "Synthesis, structural characterization, and electronic structure of the novel Zintl phase Ba_2ZnP_2," *Acta Crystallogr. Sect. C Struct. Chem.*, vol. 76, no. 9, Art. no. 9, Sep. 2020, doi: 10.1107/S2053229620010827.

PART 1

THEORETICAL FRAMEWORK

CHAPTER 1

DENSITY FUNCTIONAL THEORY

Douglas Rayner Hartree (27 March 1897 – 12 February 1958) was an English mathematician and physicist. He is known for his development of numerical analysis and its application to atomic physics.

Erwin Rudolf Josef Alexander Schrödinger (August 12, 1887 in Vienna – January 4, 1961) was an Austrian physicist and scientific theorist. winner of the Nobel Prize in Physics in 1933).

Walter Kohn (March 9, 1923 in Vienna, Austria) is an Austrian physicist, naturalized American. He is the winner of the 1998 Nobel Prize in Chemistry.

Lewellyn Hilleth Thomas is a physicist and applied mathematician born October 21, 1903 and died April 20, 1992, he is known by the Thomas-Fermi model.

J. Lu. Sham born in Colombia, Hong Kong on April 28, 1938. He is a Chinese physicist best known for his work with Walter Kohn on the Kohn-Sham equations.

Pierre C. Hohenberg (born October 3, 1934 in Neuilly-sur-Seine) is a French-American theoretical physicist, who works mainly on statistical mechanics.

John Clarke Slater, born December 22, 1900 in Oak Park, Illinois and died July 25, 1976 in Sanibel, Florida, is an American theoretical physicist and chemist, who made major contributions to the theory of the electronic structure of atoms, molecules and solids.

Enrico Fermi (September 29, 1901 in Rome) is an Italian-American physicist whose research served as a basis for the exploitation of nuclear energy. He won the 1938 Nobel Prize in Physics "for his demonstration of the existence of new elements radioactive".

Max Born (December 11, 1882 in Breslau, German Empire – January 5, 1970) was a German, then British, physicist. He won half of the 1954 Nobel Prize in Physics for his work on quantum theory.

Julius Robert Oppenheimer (April 22, 1904 in New York – February 18, 1967 at Princeton, New Jersey, United States) is an American physicist who distinguished himself in theoretical physics. He is regularly nicknamed the father of the bomb atomic".

Vladimir A.Fock was born on December 22, 1898 in Strasterburg and died on December 27, 1974, he was a teacher at the University of Saint Petersburg, he made fundamental contributions to quantum theory.

1.1 Introduction

The advancement in computational power and calculation methods has enabled the determination of material properties with high accuracy through ab initio (first-principles) methods of electronic structure, without any reliance on experimental parameters. This has not only facilitated the explanation of known material properties but also enabled the prediction of properties suitable for new materials, thus replacing expensive and impractical laboratory experiments [1, 2]. As a result, basic computational methods have become increasingly important in materials science, and are now considered essential complements to experimental research techniques in various fields [3].

Calculation methods refer to the mathematical and computational techniques used to predict, simulate, or analyse various physical, chemical, or biological phenomena. There are several calculation methods used in various scientific fields, including:

1. Quantum Mechanics: It is a branch of physics that deals with the behavior of matter and energy at the atomic and subatomic level. Quantum mechanics calculations are used to predict the behavior of atoms, molecules, and solids. The commonly used quantum mechanical calculation methods include Density Functional Theory (DFT), Hartree-Fock (HF), and Configuration Interaction (CI).

2. Molecular Dynamics: Molecular dynamics (MD) is a simulation method used to predict the time evolution of a molecular system. MD calculations are used to study the behavior of complex biological molecules, such as proteins and nucleic acids. The commonly used molecular dynamics calculation methods include classical MD, ab initio MD, and coarse-grained MD.

3. Monte Carlo: The Monte Carlo method is a statistical calculation method used to simulate the behavior of a system based on random sampling. Monte Carlo calculations are used in various fields, such as physics, chemistry, finance, and engineering. The commonly used Monte Carlo calculation methods include Metropolis-Hastings algorithm, Gibbs sampling, and Importance sampling.

4. Finite Element Method: The Finite Element Method (FEM) is a numerical calculation method used to solve differential equations by dividing the problem into smaller, finite elements. FEM calculations are used in various fields, such as civil engineering, mechanical engineering, and aerospace engineering.

5. Computational Fluid Dynamics: Computational Fluid Dynamics (CFD) is a numerical calculation method used to simulate fluid flow and heat transfer in a system. CFD calculations are used in various fields, such as aerospace engineering, automotive engineering, and chemical engineering.

These are just a few examples of the many calculation methods used in various scientific fields. Each method has its own strengths and limitations, and the appropriate method is chosen based on the specific research question and available computational resources.

Ab initio calculations have gained increasing interest among physicists and chemists due to their potential to reduce costs and accelerate results. These first-principles methods aim to calculate the physical and chemical properties of materials without relying heavily on approximations, using the fundamental equations of quantum mechanics. Complex interactions related to the structural and chemical properties of materials lead to a range of functional properties, making accurate and quantitative insight into such properties critical for optimizing and understanding material behavior. First-principles calculations based on Density Functional Theory (DFT) have resulted in significant advancements in our understanding of the underlying physics of such systems. DFT is a widely used approach for studying electronic structure by minimizing the one-body density functional to determine the system's ground-state energy, with the electronic charge density being a crucial factor. DFT has been successful in describing the structural and electronic properties of a broad range of materials, and complementary implementations such as calculating polarization using the Berry phase formalism and merging with perturbation theory (DFPT) have expanded its application and success. Additionally, DFT is computationally efficient and well-implemented in a range of codes. The following sections provide an overview of DFT and related implementations utilized throughout this thesis.

1.2 Equation of Schrödinger and Many-Body problem

In order to practically apply the density functional approach, the methodology relies on solving the one-electron Schrödinger equation using a local effective potential to investigate the ground-state properties of many-electron systems. In the presence of N nuclei, each with Z electrons (where Z represents the atomic number), this leads to a many-body problem. To study a system at the atomic level, one must initially consider the interactions between electrons and electrons, electrons and nuclei, and nuclei and nuclei. This is achieved through solving the generalized Schrödinger equation.

$$\hat{H}\Psi = i\partial\Psi / \partial t \qquad (1.1)$$

In this context, $\hat{H}$ refers to the quantum Hamiltonian operator, *i* represents the imaginary unit, and Ψ denotes the wave function of the quantum system.

The time dependent Schrödinger equation is:

$$\hat{H}(t)\left|\Psi(t)\right\rangle = i\hbar\frac{d}{dt}\left|\Psi(t)\right\rangle \qquad (1.2)$$

In this context, $\hbar$ is the reduced Planck constant.

For a non-relativistic system, independent of time, we write the Schrödinger equation as follows:

$$\hat{H}\Psi = E\Psi \qquad (1.3)$$

In this context, *E* is the total energy and the quantum Hamiltonian operator is written as:

$$\hat{H} = \hat{T}_e + \hat{T}_n + \hat{V}_{ee} + \hat{V}_{en} + \hat{V}_{nn} \qquad (1.4)$$

In this context, $\hat{T}_e, \hat{T}_n, \hat{V}_{ee}, \hat{V}_{en}, \hat{V}_{nn}$ and $\hat{V}_{nn}$ are the kinetic energy operator of electrons, the kinetic energy operator of nuclei, the potential of electron-electron Coulomb interactions, the potential of electron-nucleus Coulomb interactions and the potential of nucleus -nucleus Coulomb interactions, respectively.

So, for more details:

$$\hat{H} = -\frac{\hbar^2}{2m_e}\sum_i \nabla_{\vec{r}_i}{}^2 - \frac{\hbar^2}{2m_n}\sum_i \nabla_{\vec{R}_i}{}^2 + \frac{\hbar^2}{8\pi\varepsilon_0}\sum_{i\neq j}\frac{e^2}{\left|\vec{r}_i - \vec{r}_j\right|} - \frac{\hbar^2}{4\pi\varepsilon_0}\sum_{i,j}\frac{z_i e^2}{\left|\vec{R}_i - \vec{r}_j\right|} + \frac{\hbar^2}{8\pi\varepsilon_0}\sum_{i\neq j}\frac{z_i z_j e^2}{\left|\vec{R}_i - \vec{R}_j\right|} \qquad (1.5)$$

In this context, m_n and m_e are the mass of the nucleus and electrons, $\vec{R}_i$ and $\vec{r}_i$, are the positions of nuclei and electrons, respectively.

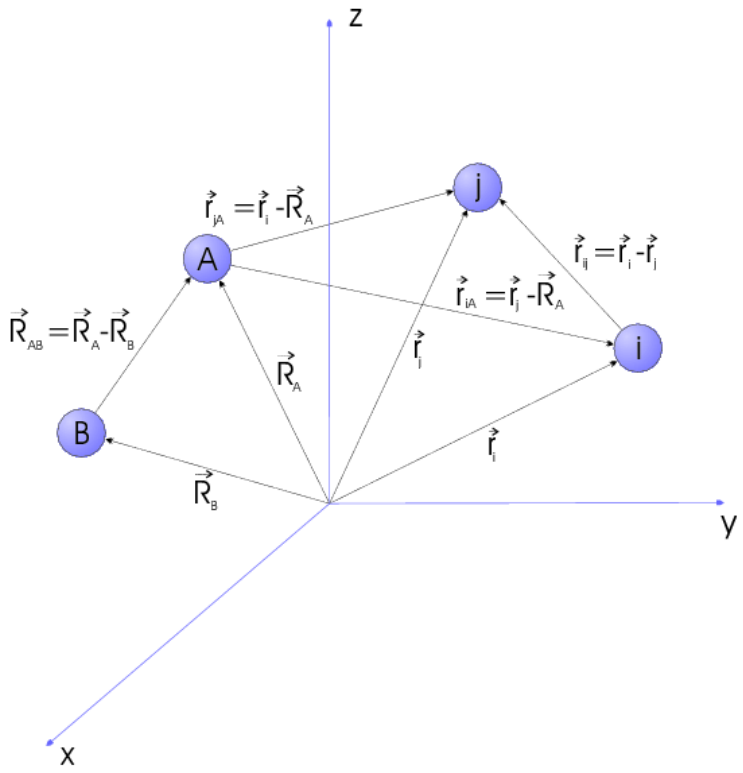

Fig. 1.1: The nucleus and electrons dependent to the positions $\vec{R}_i$ and $\vec{r}_i$.

Finally, depending on the system under consideration, the two types of particles can couple to an external electromagnetic field [4]:

$$\hat{V}_{n-field}=\sum_i\left[Z_i e\Phi_{ext}\left(R_i t\right)+i\frac{Z_i e\hbar}{M_i c}A_{ext}\left(R_i t\right).\nabla_{Ri}-I_i.B_{ext}\left(R_i t\right)\right] \qquad (1.6)$$

So, $\hat{H}=\hat{T}_e+\hat{T}_n+\hat{V}_{ee}+\hat{V}_{en}+\hat{V}_{nn}+\hat{V}_{n-field}+\hat{V}_{e-field}$ (1.7)

In this context, Φ_{ext} and A_{ext} are the potentials corresponding to the electromagnetic field

$E_{ext}\left(rt\right)=-\nabla\Phi_{ext}\left(rt\right)-\frac{1}{c}\frac{\partial A_{ext}\left(rt\right)}{\partial t}$, and $B_{ext}\left(rt\right)=\nabla.A_{ext}\left(rt\right)$, I_i characterizes the magnetic moment of the nucleus *i*, μ_B is the Bohr magneton, $\mu_B=\frac{e\hbar}{2mc}$, and σ_j is the spin operator corresponding to the electron *j*. Practically, for many-body systems, this task will be done in following levels.

It is out of question to solve the Equation of Schrödinger for Many-Bodies exactly. In order to find acceptable approximate eigen-states, we will need to make approximations at 3 different levels.

1.2.1 LEVEL 1: Born-Oppenheimer approximation

One year following the publication of the Schrödinger equation, Max Born and Robert Oppenheimer discussed the significant discrepancy in mass between two distinct types of particles in their oft-cited but less-read publication of 1927 [5]. This approach enables scientists to differentiate between the motions of electrons and nuclei, thereby simplifying the mathematical solution of the Schrodinger equation. The separation is predicated on the fundamental reality that the nuclei masses are considerably larger than the electrons masses [6]. Therefore, the kinetic energy of the nuclei is typically ignored in this approximation ($\hat{T}_n = 0$), allowing for the nuclei to be treated as static at their respective positions.

What are the implications of using the Born-Oppenheimer approximation on the Hamiltonian in equation 1.3? As a result of the approximation, the nuclei are considered stationary, which means that their kinetic energy becomes zero and the first term of the Hamiltonian disappears. The last term is reduced to a constant value. This leaves us with the kinetic energy of the electron system, the potential energy resulting from electron-electron interactions, and the potential energy of the electrons within the external potential of the nuclei. This can be expressed formally as: $\hat{H} = \hat{T} + \hat{V} + \hat{V}_{ext}$ (1.8)

$$\hat{H}_e = \hat{T}_e + \hat{V}_{ee} + \hat{V}_{en} = -\frac{\hbar^2}{2m_e}\sum_i \nabla_{\vec{r}_i}{}^2 + \frac{\hbar^2}{8\pi\varepsilon_0}\sum_{i\neq j}\frac{e^2}{\left|\vec{r}_i - \vec{r}_j\right|} - \frac{\hbar^2}{4\pi\varepsilon_0}\sum_{i,j}\frac{z_i e^2}{\left|\vec{R}_i - \vec{r}_j\right|} \qquad (1.9)$$

$$H_e\Psi = E_e\Psi \qquad (1.10)$$

An interesting observation to make is that the kinetic and electron-electron terms $(\hat{T} + \hat{V})$ in equation 1.9 are solely dependent on the fact that we are dealing with a many-electron system, making them **universal**. On the other hand, system-specific information such as which nuclei are involved and their positions are entirely provided by the potential energy term ($\hat{V}_{ext}$).

If spin-orbit (SO) effects are deemed significant, they can be incorporated for every nuclear configuration using the following approach [7]:

$$\hat{H}_0 = \hat{H}_e + \hat{H}_{SO} \qquad (1.11)$$

$$\hat{H}_0 \Psi = E_0 \Psi \qquad (1.12)$$

To resolve the intricate many-body problem of electrons, which entails a vast quantity of particles and intricate electron-electron interactions, additional approximations must be implemented.

1.2.2 LEVEL 2: Density Functional Theory

After applying the initial level of approximation, known as the Born-Oppenheimer approximation, the resulting quantum many-body problem becomes less complex than its original form but still proves to be excessively intricate to resolve. Numerous techniques exist to simplify equation 1.9 into an approximate yet manageable form. One historically significant method is the Hartree-Fock (HF) method, elucidated in various condensed matter textbooks, which demonstrates exceptional performance in the context of atoms and molecules and is thus frequently employed in quantum chemistry. Nonetheless, its precision is comparatively lower when applied to solids. In this context, we will not delve into the intricacies of the HF method but rather explicate a more contemporary and potent method - Density Functional Theory (DFT).

1.2.2.1 The theorems of Hohenberg and Kohn

In 1964, a significant paper was published by Hohenberg and Kohn in the Physical Review [8], which gave birth to Density Functional Theory (DFT). This seminal report presented the fundamental theorems that serve as the key theoretical foundations for all contemporary DFT approaches. These theorems form the fundamental pillars upon which the entire DFT framework is constructed [9]

Hohenberg and Kohn formulated two theorems that establish density functional theory (DFT) as a rigorous quantum physical approach. DFT takes into account the interactions between electrons, as well as their interaction with an external potential, by using the ground-state electron density. This external potential is the attraction of the electrons to the nuclei, and its determination relies on knowledge of the charges and positions of the nuclei in the real system. Once the number of electrons is integrated into the density, the external potential can be uniquely determined by the ground-state electron density.

First theorem: *There is a one-to-one correspondence between the ground-state electron density* $\rho(\vec{r})$ *of a many-electron system, such as an atom, molecule, or solid, and the external potential* V_{ext}*. As a direct result of this theorem, the expectation value of any observable* $\hat{O}$ *in the exact ground state of the system is uniquely determined by the ground-state electron density:* $<\psi|\hat{O}|\psi> = O[\rho]$

Second theorem: For $\hat{O}$ being $\hat{H}$, the ground-state total energy functional $H[\rho] \equiv E_{V_{ext}}[\rho]$ is of the form:

$$\begin{cases} E_{V_{ext}}[\rho] = <\psi|\hat{T}+\hat{V}|\psi> + <\psi|\hat{V}_{ext}|\psi> \\ \qquad\qquad = F_{HK}[\rho] + \int \rho(\vec{r}) V_{ext}(\vec{r}) d\vec{r} \end{cases} \qquad (1.13)$$

With the context, the Hohenberg-Kohn density functional $F_{HK}[\rho] = <\psi|\hat{T}+\hat{V}|\psi>$ is universal for any many-electron system.

$E_{V_{ext}}[\rho]$ reaches its minimal value (equal to the ground-state total energy) for the ground-state density corresponding to V_{ext}.

The one-to-one correspondence between ground-state density and external potential $(\rho \leftrightarrow V_{ext})$ is a fascinating concept. It is evident that every many-electron system possesses a unique external potential, which, when applied in conjunction with the Hamiltonian and Schrödinger's equation, results in a unique many-particle wave function for the ground state. The corresponding electron density can be effortlessly derived from this wave function. Thus, an external potential unequivocally leads to a unique ground-state density that corresponds to it. However, it appears intuitively that the density carries less information than the wave function. If this were the case, it would not be possible to determine a unique external potential with only a ground-state density. Remarkably, the first theorem of Hohenberg and Kohn establishes that this is indeed possible. The density contains just as much information as the wave function does, which is to say that it encapsulates all of the knowledge that could be acquired about an atom, molecule, or solid. Hence, all measurable quantities can be obtained in a unique manner from the density alone, that is, they can be expressed as functionals of the density.

The universality of $F_{HK}[\rho] = <\psi|\hat{T}+\hat{V}|\psi>$ is noteworthy. Equation 1.13 can be easily derived using the density operator, and with the knowledge of the ground-state density, the contribution to the total energy resulting from the external potential can be calculated with

precision. Despite the absence of an explicit expression for the Hohenberg-Kohn functional $F_{HK}[\rho]$, it is a universal functional for any many-electron system since it does not contain information regarding the nuclei and their positions. As a result, an expression for $F_{HK}[\rho]$ exists in theory, which can be applied to any atom, molecule, or solid.

The second theorem enables the use of the Rayleigh-Ritz variational principle [10] to determine the ground-state density. Among the infinite possible densities, the one that minimizes $E_{V_{ext}}[\rho]$ is considered the ground-state density, which corresponds to the external potential $V_{ext}(\vec{r})$. However, this process can only be carried out if an approximation of $F_{HK}[\rho]$ is available. Once the density ρ is obtained, all information about the system becomes accessible.

It is important to emphasize the significance of the energy functional $E_{V_{ext}}[\rho]$. When the density ρ is evaluated for the specific V_{ext} of a solid, it provides the ground state energy. However, if it is evaluated for any other density, the resulting number has no physical significance.

1.2.2.2 The Kohn-Sham equations

The Kohn-Sham equations, which were introduced in 1965, have made density functional theory (DFT) a practical tool for determining the ground state density. The equations provide a practical procedure for obtaining the ground state density by rewriting the Hohenberg-Kohn functional. In this functional, the correlation energy is defined as the difference between the total energy in the exact solution and the Hartree-Fock solution. The total energy functionals, denoted as $E_e[\rho]$ and $E_{HF}[\rho]$, correspond to the exact and Hartree-Fock Hamiltonians, respectively, are [9]:

$$E_e = T + V \quad (1.14) \qquad \text{and} \qquad E_{HF} = T_0 + \underbrace{(V_H + V_x)}_{V} \quad (1.15)$$

In the context of the Kohn-Sham density functional theory, the exact kinetic and electron-electron potential energy functionals are denoted as T and V, respectively, while T_0 represents the functional for the kinetic energy of a non-interacting electron gas. Additionally, V_H stands for the Hartree contribution to the potential energy, and V_x represents the exchange contribution. Subtracting the expression for the Hartree potential energy from the total potential energy gives the expression for the exchange-correlation potential energy. By

subtracting the equation for the Hartree potential energy (1.15) from the total potential energy (1.14), the functional for the correlation contribution to the potential energy can be obtained.

$$V_c = T - T_0 \qquad (1.16)$$

The exchange contribution to the total energy refers to the component that is present in the Hartree-Fock solution but is absent in the Hartree solution. It is worth noting that the Hartree functional can be expressed as: $E_H = T_0 + V_H$ (1.17)

So, V_x can be defined as follows: $V_x = V - V_H$ (1.18)

Within this context, the Hohenberg-Kohn functional can be rewritten as follows:

$$\begin{aligned} E_{HK} &= T + V = T + V + T_0 - T_0 \\ &= T_0 + V + \underbrace{(T - T_0)}_{V_c} \\ &= T_0 + V + V_c + V_H - V_H \\ &= T_0 + V_H + V_c + \underbrace{(V - V_K)}_{V_x} \\ &= T_0 + V_H + \underbrace{(V_x + V_c)}_{V_{xc}} \end{aligned}$$

In this context, V_{xc} refers to the exchange-correlation energy functional, which incorporates the challenging exchange and correlation contributions. However, it is formally unknown to us. Assuming, for the moment, that we do have knowledge of V_{xc}, we can explicitly represent the energy functional [9]:

$$E_{V_{ext}}[\rho] = T_0[\rho] + V_H[\rho] + V_{xc}[\rho] + V_{ext}[\rho] \qquad (1.19)$$

One could potentially apply the second Hohenberg-Kohn theorem to determine the ground state density, but this would not be beneficial to the transformation we have made. Alternatively, the above expression can be viewed as the energy functional of a non-interacting classical electron gas, subject to two external potentials: one originating from the nuclei, and the other from exchange and correlation effects. The corresponding Hamiltonian, referred to as the Kohn-Sham Hamiltonian, is defined as follows:

$$\hat{H}_{KS} = \hat{T}_0 + \hat{V}_H + \hat{V}_{xc} + \hat{V}_{ext} \qquad (1.20)$$

$$= \frac{\hbar^2}{2m_e}\vec{\nabla}_i + \frac{e^2}{4\pi\varepsilon_0}\int \frac{\rho(\vec{r}\,')}{|\vec{r} - \vec{r}\,'|} d\vec{r}\,' + V_{xc} + V_{ext} \qquad (1.21)$$

The Kohn-Sham theorem can be expressed in the following manner: The ground-state density of a system with N electrons, denoted by $\rho(\vec{r})$, is equal to:

$$\rho(\vec{r}) = \sum_{i=1}^{N} \phi_i(\vec{r}) * \phi_i(\vec{r}) \qquad (1.22)$$

Where the N lowest-energy solutions of the Kohn-Sham equation, represented by the single-particle wave functions $\phi_i(\vec{r})$, are used. The Kohn-Sham equation can be defined as:

$$\hat{H}_{KS}\phi_i = \varepsilon_i\phi_i \qquad (1.23).$$

Now, the second Hohenberg-Kohn theorem is no longer necessary to determine the ground-state density. Instead, we can solve non-interacting single-particle equations that resemble the Schrödinger equation. This approach is more feasible than using the regular Schrödinger equation, which would involve solving a complex system of coupled differential equations due to the electron-electron interaction. The advantage of relying on the non-interacting single-particle equations lies in their simplicity, which enables us to determine the ground-state density efficiently. This approach has revolutionized the study of electronic structure in materials science by providing a more practical method for calculating electronic properties of materials.

It's important to note that the single-particle wave functions $\phi_i(\vec{r})$ are not equivalent to the wave functions of individual electrons. Instead, they represent mathematical quasi-particles that do not have a direct physical interpretation. The overall density of these quasi-particles is the only quantity that can be guaranteed to match the true electron density. Furthermore, the single-particle energies ε_i do not correspond to the energies of individual electrons. Rather, they represent the energies of these quasi-particles. While this may seem like a subtle distinction, it is a crucial aspect of the Kohn-Sham approach that allows for efficient calculations of electronic properties in materials. The use of quasi-particles has become a powerful tool in modern condensed matter physics, and has led to significant advancements in our understanding of materials at the atomic scale.

Both the Hartree operator V_{H} and the exchange-correlation operator V_{xc} are dependent on the density $\rho(\vec{r})$, which, in turn, depends on the single-particle wave functions $\phi_i(\vec{r})$. This leads to a self-consistency problem where the solutions ($\phi_i(\vec{r})$) determine the original equation (V_H and V_{xc} in H_{KS}), and the equation cannot be solved until its solution is known. An iterative procedure is required to overcome this paradox, as shown in **Fig. 1.2**. The iterative procedure starts with a guessed density ρ_0, which is used to construct a Hamiltonian,

denoted by H_{KS1}. The eigenvalue problem is then solved, yielding a set of ϕ_1 from which a density ρ_1 can be derived. Typically, ρ_0 and ρ_1 will differ from each other. The density ρ_1 is then used to construct H_{KS2}, which generates a new density ρ_2, and so on. This procedure can be repeated until a final density ρ_f is reached, which generates a H_{KSf} that yields the same density ρ_f as its solution. This final density is consistent with the Hamiltonian.

This iterative approach allows us to solve the self-consistency problem and determine an accurate ground-state density for the system. The Kohn-Sham approach has become a powerful tool for calculating electronic properties in materials science, and its success is largely due to its ability to solve the self-consistency problem efficiently.

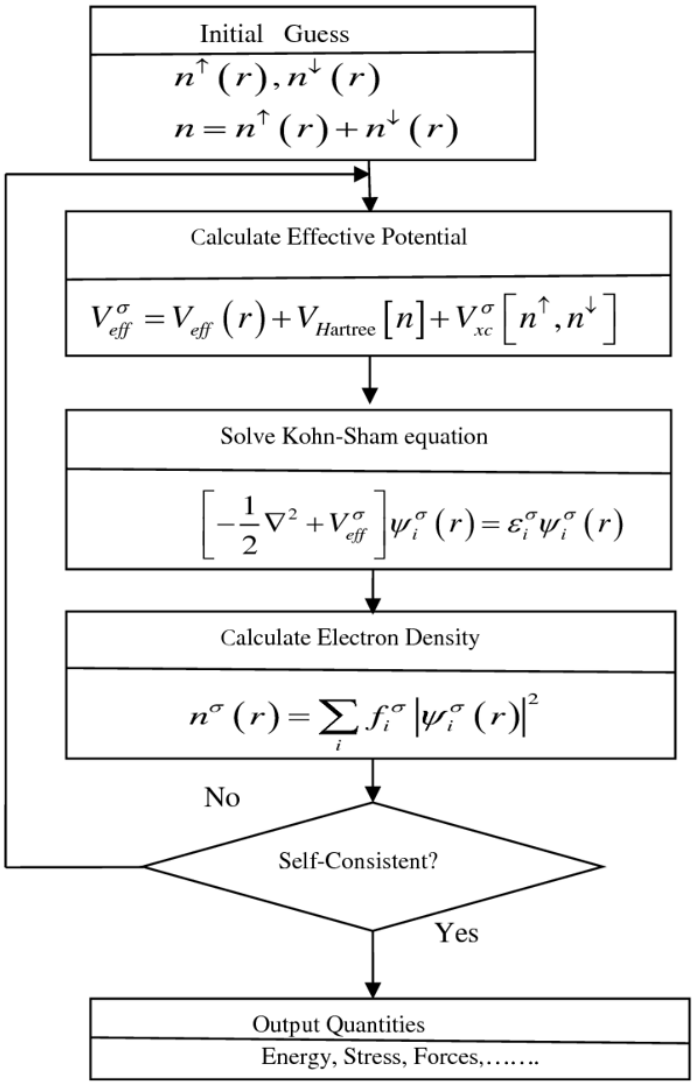

Fig. 1.2: Flow chart outlining the iterative self-consistency procedure for solving the Hartree-Fock or Kohn-Sham equations [11].

1.2.2.3 Approximations for the Exchange-Correlation energy

The accurate and reliable description of the electronic structure of atoms, molecules, and materials is a fundamental goal in theoretical chemistry, condensed matter physics, and materials science. One of the most successful and widely used methods for this purpose is density functional theory (DFT), which reduces the many-body problem to the calculation of the electronic density and solves it via the Kohn-Sham equations. However, the practical implementation of DFT requires the specification of an essential ingredient, namely, the exchange-correlation energy functional E_{xc}, which describes the non-classical many-electron interactions that are not accounted for by the classical Coulomb interactions. Unfortunately, the exact form of E_{xc} is not known and may never be known, which poses a major challenge to the accuracy and applicability of DFT. To overcome this challenge, various approximations for E_{xc} have been proposed since the inception of DFT, ranging from simple and efficient to complex and accurate. These approximations are usually expressed in terms of explicit or implicit functionals of the electronic density, which are often parameterized by empirical or non-empirical methods. Recently, Perdew has introduced a useful and insightful classification scheme for the many and varied E_{xc} functionals that exist, based on a metaphorical ladder with rungs that correspond to different levels of approximation and accuracy. The lowest rung is the Hartree approximation, which neglects the exchange-correlation effects entirely and reduces E_{xc} to zero. The highest rung is the exact exchange-correlation functional, which incorporates all the non-classical many-electron interactions exactly, but is practically unknown and computationally infeasible. The intermediate rungs include various levels of approximation, such as the local density approximation, the generalized gradient approximation, the meta-generalized gradient approximation, the hybrid functionals, and the range-separated functionals. These approximations are classified into non-empirical and empirical categories, depending on whether they are derived from first principles or fitted to experimental or theoretical data. The Jacob's ladder classification scheme [12] provides a systematic and intuitive way of comparing and selecting different E_{xc} functionals for specific applications, depending on the desired level of accuracy and computational cost. Furthermore, the choice of E_{xc} functional depends on the physical and chemical properties of the system under investigation, such as the electronic structure, bonding, reactivity, spectroscopy, and thermodynamics. For example, some E_{xc} functionals may be suitable for describing the ground-state properties of isolated atoms or small molecules, but not for extended or complex systems, while others may be better for capturing the dynamic and excited-state properties of molecules or materials. Therefore, it is important to test and validate the accuracy and

reliability of different E_{xc} functionals for a given system and property of interest, and to account for the limitations and uncertainties associated with the approximations and assumptions made. In recent years, there have been significant advances in the development and assessment of new and improved E_{xc} functionals, based on machine learning, data mining, quantum chemistry, and many other techniques. These advances have opened up new opportunities and challenges for the application and interpretation of DFT in various fields of science and technology, ranging from catalysis and energy storage to materials design and drug discovery.

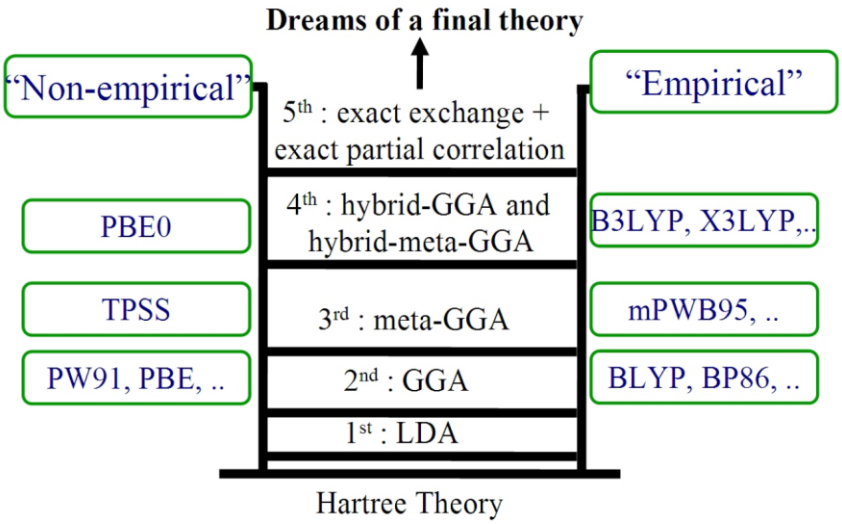

Fig. 1.3: Schematic diagram of "Jacob's ladder" of exchange-correlation functionals proposed by J. P. Perdew [12].

1.2.2.3.1 Local Density Approximation

The Local Density Approximation (LDA) is a widely used approximation for the exchange-correlation interaction in quantum mechanics. It is regarded as one of the earliest and most conventional approximations in the field. The fundamental concept behind LDA is that the exchange-correlation energy of a system is assumed to be equivalent to that of a homogeneous electron gas possessing the same density. The exchange-correlation energy of this homogeneous electron gas has been accurately defined and characterized by previous research. Specifically, LDA assumes that the exchange-correlation energy of a non-uniform electron system can be approximated by integrating the exchange-correlation energy density of the electron gas over the density distribution of the non-uniform system. This approximation has proved to be successful in various fields of research, including condensed

matter physics, materials science, and quantum chemistry. The exact expression of the exchange-correlation energy of such a homogeneous electron gas is known:

$$E_{xc}[\rho] = \int \rho(r)\varepsilon_{xc}^{\text{hom}}[\rho(r)]dr \qquad (1.24)$$

In this context, $\varepsilon_{xc}^{\text{hom}}$ is the exchange-correlation energy per electron of a homogeneous electron gas of density ρ. $\varepsilon_{xc}^{\text{hom}}$ can be expressed in various analytical parameterized forms, among which one finds those by Hedin-Lundqvist [13], Barth-Hedin [14], Vosko-Wilk-Nusair [15], Ceperley-Alder [16], Perdew-Zunger [17]. In practice, exchange and correlation are calculated separately. The analytical expression for the exchange energy is known exactly:

$$E_x^{LDA}[\rho] = -\frac{3}{4}\left(\frac{3}{\pi}\right)^{1/3}\int \rho^{4/3}(r)dr \qquad (1.25)$$

Strictly, the LDA is valid only for slowly varying densities. Experience with calculations of atoms, molecules, and solids shows that penultimate equation can in general also be applied to these systems. Indeed, LDA works surprisingly well, especially for metals. A partial explanation for this success of the partial LDA is systematic error cancelation: Typically, in inhomogeneous systems LDA underestimates correlation but overestimates exchange, resulting in unexpectedly good values of E_x^{LDA}. This error cancelation is not accidental, but systematic, and caused by the fact that for any density the LDA satisfies a number of so-called sum rules [18], [19]. The expression of correlation energy has been estimated by means of different numerical parameterizations [17] and [20]. All of which leads to very similar total energy results [21].

Despite the shortcomings found in LDA, it achieved good results in several areas, including the following:

Firstly, the structural, elastic, and vibrational properties often good enough

1. Crystal bulk lattice constants accurate to within 3%, usually underestimated.
2. Bulk moduli somewhat too large, > 10% error not uncommon for d metals.
3. Phonons somewhat too stiff.

Secondly, binding energies are too negative (overbinding), up to several eV

1. Cohesive energies of solids, but formation enthalpies often o.k.
2. Molecular atomization energies, mean error ≈ 3 eV

Thirdly, activation energies in chemical reactions unreliable

1. Too small/absent, e.g., for H_2 on various surfaces (Al, Cu, Si, ...).

Fourthly, relative stability of crystal bulk phases can be uncertain

1. SiO_2 high pressure phase more stable than zero pressure phase
2. Underestimated transition pressure e.g., for diamond β-tin phase transitions in Si & Ge.
3. Magnetic phases.

Fifthly, electronic structure can be usefully interpreted (density of states, band structures), except for band gaps (a more fundamental issue than LDA!) [22].

1.2.2.3.2 Generalized gradient approximation

The Generalized Gradient Approximation (GGA) is a widely used method in computational chemistry and physics that improves upon the Local Density Approximation (LDA) by incorporating the density gradient in the exchange-correlation contribution. This allows for a more accurate description of the electronic structure of molecules and materials. GGA functionals are designed to calculate the exchange-correlation contribution of each infinitesimal volume based not only on the local density in that volume, but also on the density in neighboring volumes. This is accomplished by including the gradient of the density in the calculation. Because of this input, the method is called the Generalized Gradient Approximation. While there is only one LDA exchange-correlation functional due to a unique definition of the exchange-correlation energy, there is some freedom in incorporating the density gradient into the calculation, resulting in several versions of GGA functionals. However, the parameters for these functionals must be carefully chosen and are often based on experimental data, which means that GGA calculations are not strictly speaking ab initio. Despite these drawbacks, much progress has been made in developing successful GGA functionals over the years. Some of the most commonly used GGA functionals include Perdew 86 (P86) [23], Becke (B86, B88) [24], Perdew-Wang 91 (PW91) [25], Laming-Termath-Handy (CAM), Perdew-Burke-Ernzerhof (PBE)[25], revised Perdew-Burke-Ernzerhof (RPBE) [26], Perdew-Burke-Ernzerhof revised for solids (PBEsol) [27], Becke exchange and Lee-Yang-Parr correlation (BLYP) [28], and Armiento-Mattsson 2005 (AM05) [29]. As an example of the applications of GGA functionals, PW91 is widely used for modelling metallic surfaces, while PBE and RPBE are often applied to study metal oxides in

heterogeneous catalysis research [30]. These functionals have been shown to provide more accurate predictions for total energies, atomization energies, and structural properties than LDA functionals, but they still have limitations, such as their inability to describe van der Waals interactions and their tendency to underestimate barrier heights. The exchange-correlation functional $E_{xc}[\rho]$ within GGAs is typically approximated by a specific mathematical form [31]:

$$E_{xc}^{GGA}[\rho_\uparrow, \rho_\downarrow] = \int dr\, f(\rho_\uparrow, \rho_\downarrow, \nabla\rho_\uparrow, \nabla\rho_\downarrow) \qquad (1.26)$$

Here, f is a parameterized analytic functions

The GGAs are called "semi-local" functionals due to their dependence on $\nabla\rho(r)$. For many properties, for example geometries and ground state energies of molecules and solids, GGAs can yield better results than the LDAs. Especially for covalent bonds and weakly bonded systems, many GGAs are far superior to LDA. The functional form of $f(\rho_\uparrow, \rho_\downarrow, \nabla\rho_\uparrow, \nabla\rho_\downarrow)$ is taken as a correction to the LDA exchange and correlation while (again) ensuring consistency with known sum rules. In fact, some of these functionals are not even based on any physical model. In other words, the actual form of GGA E_X and GGA E_C usually does not assist the understanding of the physics these functionals try to describe.

Within GGA the exchange energy takes the form [32]:

$$E_x^{GGA} = E_x^{LDA} - \sum_\sigma \int F(s_\sigma)\rho_\sigma^{4/3}(r)dr \quad (1.27)$$

The argument of the function F is the reduced density gradient for spin σ

$$s_\sigma(r) = \frac{|\nabla\rho_\sigma(r)|}{\rho_\sigma^{4/3}(r)} \qquad (1.28)$$

s_σ is to be understood as a local inhomogeneity parameter.

For the function F two main classes of realizations have been put forward (see in particular Adamo, di Matteo, and Barone, 1999). The first one is based on a GGA exchange functional developed by Becke, 1988b. As outlined above, this functional is abbreviated simply as B (sometimes one also finds B88) [32]:

$$F^{B88} = \frac{\beta s_\sigma^2}{1 + 6\beta s_\sigma \sinh^{-1} s_\sigma} \qquad (1.29)$$

β is an empirical parameter that was determined to 0.0042 by a least-squares fit to the exactly known exchange energies of the rare gas atoms He through Rn. In addition to the sum rules, this functional was designed to recover the exchange energy density asymptotically far from a finite system.

The second class of GGA exchange functionals use for F a rational function of the reduced density gradient. Prominent representatives are the early functionals by Becke, 1986 (B86) and Perdew, 1986 (P), the functional by Lacks and Gordon, 1993 (LG) or the recent implementation of Perdew, Burke, and Ernzerhof, 1996 (PBE). As an example, we explicitly write down F of Perdew's 1986 exchange functional, which, just as for the more recent PBE functional, is free of semi-empirical parameters [32]:

$$F^{P86} = \left(1 + 1.296\left(\frac{s_\sigma}{(24\pi^2)^{1/3}}\right)^2 + 14\left(\frac{s_\sigma}{(24\pi^2)^{1/3}}\right)^4 + 0.2\left(\frac{s_\sigma}{(24\pi^2)^{1/3}}\right)^6\right)^{1/15} \qquad (1.30)$$

We finally note a semantic detail. GGA functionals are frequently termed *non-local* functionals in the literature. This is a somewhat misleading and actually sloppy terminology that should be avoided.

1.2.2.3.3 Meta-generalized gradient approximation and hybrid functionals

Meta-GGAs typically improve upon the accuracy of GGAs as they additionally take into account the local kinetic energy density. This allows meta-GGAs to more accurately treat different chemical bonds (eg. covalent, metallic, and weak) compared to LDAs and GGAs (Examples include TPSS, revTPSS, M06L, MBJ, SCAN, MS0, MS1, MS2, RSCAN and R2SCAN etc.).

The meta-GGA can be written as [33]:

$$E_{xc}^{mGGA}[\rho,\tau] = \int d^3r f(\rho(r), \nabla\rho(r), \tau(r)) \qquad (1.31)$$

where the kinetic energy density is defined as the following summation over all occupied Kohn-Sham orbitals (r) [33]:

$$\tau(r) = \frac{1}{2}\sum_i^{OCC} (\nabla\varphi_i(r))^2 \qquad (1.32)$$

a) Modified Becke-Johnson

Here we will be interested in one meta-GGA functional, the modified Becke-Johnson (mBJ) XC potential, which has been optimized for the description of electronic band gaps of homogeneous solids. Various comparisons show that the mBJ is the best semilocal approximation to determine band gaps, achieving on average an accuracy even better than the one of hybrid functionals[34] and at a much lower computational price.

Becke and Johnson [35] proposed an exchange potential, which was designed to reproduce the exact exchange potential in atoms. The Becke and Johnson (BJ) potential, which does not contain any empirical parameter, where [36]:

$$V_x^{BJ}(r) = V_x^{BR}(r) + \frac{1}{\pi}\sqrt{\frac{5}{12}}\sqrt{\frac{2t(r)}{\rho(r)}} \qquad (1.33)$$

Where:

$$t(r) = \frac{1}{2}\sum_{i=1}^{N}\nabla\psi_i^*(r)\nabla\psi_i(r) \qquad (1.34)$$

$t(r)$ is the KS kinetic-energy density, and

$$V_x^{BR}(r) = -\frac{1}{b(r)}\left(1 - e^{-x(r)} - \frac{1}{2}x(r)e^{-x(r)}\right) \qquad (1.35)$$

and

$$b = [x^3 e^{-x} / (8\pi\rho)]^{1/3} \qquad (1.36)$$

$V_x^{BR}(r)$ is the Becke-Roussel [37] exchange potential.

x is determined from a nonlinear equation involving.

There is a simple modification of the BJ potential (called TB-mBJ) was proposed,

$$V_x^{TB-mBJ}(r) = CV_x^{BR}(r) + (3C-2)\frac{1}{\pi}\sqrt{\frac{5}{12}}\sqrt{\frac{2t(r)}{\rho(r)}} \qquad (1.37)$$

Where

$$C = A + B\sqrt{\bar{g}} \qquad (1.38)$$

and

$$\bar{g} = \frac{1}{V_{cell}} \int_{cell} \frac{1}{2} \left(\frac{\left|\nabla \rho^{\uparrow}(r)\right|}{\rho^{\uparrow}(r)} + \frac{\left|\nabla \rho^{\downarrow}(r)\right|}{\rho^{\downarrow}(r)} \right) d^3 r \qquad (1.39)$$

is the average of $g = |\nabla\rho|/\rho$ in the unit cell of volume V_{cell}.

A and B are two free parameters whose values are $A = -0.012$ and $B = 1.023$ bohr$^{1/2}$ according to a fit to the experimental band gaps. The TB-mBJ potential is as accurate as the much more expensive hybrid methods.

b) Hybrid functionals

Hybrid functionals, which combine some exact exchange with a GGA, are another class of methods used in computational chemistry and physics. The most widely used hybrid functional is B3LYP. By incorporating a small fraction of exact exchange (about 20%) into the calculation, hybrid functionals can mimic the effects of static correlation and produce highly accurate results. However, the cost of computing hybrid functionals is higher than that of standard GGAs, as exact exchange is non-local and depends not only on the electron density but also on the density matrix. This means that additional approximations cannot be utilized as efficiently. Meta-GGAs are a newer class of functionals that aim to achieve similar levels of accuracy to hybrid functionals, but without the higher computational cost. The goal is to design functionals that perform almost as well as hybrid functionals but can be computed more efficiently.

References

[1] V. Sahni, "The Hohenberg-Kohn Theorems and Kohn-Sham Density Functional Theory," in *Quantal Density Functional Theory*, V. Sahni, Ed., Berlin, Heidelberg: Springer, 2004, pp. 99–123. doi: 10.1007/978-3-662-09624-6_4.

[2] Z.-G. Chen, G. Han, L. Yang, L. Cheng, and J. Zou, "Nanostructured thermoelectric materials: Current research and future challenge," *Prog. Nat. Sci. Mater. Int.*, vol. 22, no. 6, pp. 535–549, Dec. 2012, doi: 10.1016/j.pnsc.2012.11.011.

[3] A. Bejan, *Advanced engineering thermodynamics*, Fourth edition. Hoboken, New Jersey: John Wiley & Sons Inc, 2016.

[4] E. Engel and R. M. Dreizler, *Density Functional Theory: An Advanced Course*. in Theoretical and Mathematical Physics. Berlin, Heidelberg: Springer Berlin Heidelberg, 2011. doi: 10.1007/978-3-642-14090-7.

[5] M. Born and R. Oppenheimer, "Zur Quantentheorie der Molekeln," *Ann. Phys.*, vol. 389, no. 20, pp. 457–484, 1927, doi: 10.1002/andp.19273892002.

[6] F. Fernández, *The Born-Oppenheimer approximation*, Argentina 1900 La Plata, 2019. doi: 10.13140/RG.2.2.21650.91840.

[7] C. D. Sherrill, *The Born-Oppenheimer Approximation*, Georgia Institute of Technology, 2005.

[8] M. Ernzerhof and G. E. Scuseria, "Perspective on 'Inhomogeneous electron gas,'" *Theor. Chem. Acc.*, vol. 103, no. 3, pp. 259–262, Feb. 2000, doi: 10.1007/s002149900030.

[9] S. Cottenier, "*Density Functional Theory and the Family of (L)APW-methods: a step-by-step introduction*" Instituut voor Kern- en Stralingsfysica, 2002.

[10] E. K. Gross, L. N. Oliveira, W. Kohn, *Rayleigh-Ritz variational principle for ensembles of fractionally occupied states*, Phys. Rev. A: At., Mol., Opt. Phys. 1988, 37, 2805

[11] R. M. Martin, *Electronic Structure: Basic Theory and Practical Methods*. Cambridge University Press, 2004.

[12] M. R. Dreizler and E. K. U. Gross, in Density Functional Theory and Its Application to Materials, edited by V. Van Doren (AIP Press, Melville, New York), 2001.

[13] L. Hedin and B. I. Lundqvist, "Explicit local exchange-correlation potentials," *J. Phys. C Solid State Phys.*, vol. 4, no. 14, p. 2064, Oct. 1971, doi: 10.1088/0022-3719/4/14/022.

[14] U. von Barth and L. Hedin, "A local exchange-correlation potential for the spin polarized case. i," *J. Phys. C Solid State Phys.*, vol. 5, no. 13, p. 1629, Jul. 1972, doi: 10.1088/0022-3719/5/13/012.

[15] S. H. Vosko, L. Wilk, and M. Nusair, "Accurate spin-dependent electron liquid correlation energies for local spin density calculations: a critical analysis," *Can. J. Phys.*, vol. 58, no. 8, pp. 1200–1211, Aug. 1980, doi: 10.1139/p80-159.

[16] D. M. Ceperley, B. J. Alder, The ground state of the electron gas by a stochastic method. *Phys. Rev. Lett.* 1980, *45*, 566–569.

[17] J. P. Perdew and Y. Wang, "Accurate and simple analytic representation of the electron-gas correlation energy," *Phys. Rev. B*, vol. 45, no. 23, pp. 13244–13249, Jun. 1992, doi: 10.1103/PhysRevB.45.13244.

[18] O. Gunnarsson and B. I. Lundqvist, "Exchange and correlation in atoms, molecules, and solids by the spin-density-functional formalism," *Phys. Rev. B*, vol. 13, no. 10, pp. 4274–4298, May 1976, doi: 10.1103/PhysRevB.13.4274.

[19] K. Burke, J. P. Perdew, and M. Ernzerhof, "Why semilocal functionals work: Accuracy of the on-top pair density and importance of system averaging," *J. Chem. Phys.*, vol. 109, no. 10, pp. 3760–3771, Sep. 1998, doi: 10.1063/1.476976.

[20] E. J. Baerends, "Perspective on 'Self-consistent equations including exchange and correlation effects,'" in *Theoretical Chemistry Accounts*, C. J. Cramer and D. G. Truhlar, Eds., Berlin, Heidelberg: Springer Berlin Heidelberg, 2000, pp. 265–269. doi: 10.1007/978-3-662-10421-7_30.

[21] M. C. Payne, M. P. Teter, D. C. Allan, T. A. Arias, and J. D. Joannopoulos, "Iterative minimization techniques for ab initio total-energy calculations: molecular dynamics and conjugate gradients," *Rev. Mod. Phys.*, vol. 64, no. 4, pp. 1045–1097, Oct. 1992, doi: 10.1103/RevModPhys.64.1045.

[22] M. Fuchs, “Comparison of exchange-correlation functionals: from LDA to GGA and beyond”.

[23] A. D. Becke, “Density functional calculations of molecular bond energies,” *J. Chem. Phys.*, vol. 84, no. 8, pp. 4524–4529, Apr. 1986, doi: 10.1063/1.450025.

[24] P. Elliott and K. Burke, “Non-empirical derivation of the parameter in the B88 exchange functional,” *Can. J. Chem.*, vol. 87, no. 10, pp. 1485–1491, Oct. 2009, doi: 10.1139/V09-095.

[25] J. P. Perdew, K. Burke, and M. Ernzerhof, “Generalized Gradient Approximation Made Simple,” *Phys. Rev. Lett.*, vol. 77, no. 18, pp. 3865–3868, Oct. 1996, doi: 10.1103/PhysRevLett.77.3865.

[26] B. Hammer, L. B. Hansen, and J. K. Nørskov, “Improved adsorption energetics within density-functional theory using revised Perdew-Burke-Ernzerhof functionals,” *Phys. Rev. B*, vol. 59, no. 11, pp. 7413–7421, Mar. 1999, doi: 10.1103/PhysRevB.59.7413.

[27] J. P. Perdew *et al.*, “Restoring the Density-Gradient Expansion for Exchange in Solids and Surfaces,” *Phys. Rev. Lett.*, vol. 100, no. 13, p. 136406, Apr. 2008, doi: 10.1103/PhysRevLett.100.136406.

[28] E. A. McCullough, E. Aprà, and J. Nichols, “Comparison of the Becke−Lee−Yang−Parr and Becke−Perdew−Wang Exchange-Correlation Functionals for Geometries of Cyclopentadienyl−Transition Metal Complexes,” *J. Phys. Chem. A*, vol. 101, no. 13, pp. 2502–2508, Mar. 1997, doi: 10.1021/jp963430d.

[29] R. Armiento and A. E. Mattsson, “Functional designed to include surface effects in self-consistent density functional theory,” *Phys. Rev. B*, vol. 72, no. 8, p. 085108, Aug. 2005, doi: 10.1103/PhysRevB.72.085108.

[30] J. B. Krieger, J. Chen, G. J. Iafrate, and A. Savin, “Construction of An Accurate Self-interaction-corrected Correlation Energy Functional Based on An Electron Gas with A Gap,” in *Electron Correlations and Materials Properties*, A. Gonis, N. Kioussis, and M. Ciftan, Eds., Boston, MA: Springer US, 1999, pp. 463–477. doi: 10.1007/978-1-4615-4715-0_28.

[31] J. P. Perdew and K. Burke, "Comparison shopping for a gradient-corrected density functional," *Int. J. Quantum Chem.*, vol. 57, no. 3, pp. 309–319, 1996, doi: 10.1002/(SICI)1097-461X(1996)57:3<309::AID-QUA4>3.0.CO;2-1.

[32] W. Koch and M. C. Holthausen, *A Chemist's Guide to Density Functional Theory*, 1st ed. Wiley, 2001. doi: 10.1002/3527600043.

[33] C. Adamo, M. Ernzerhof, and G. E. Scuseria, "The meta-GGA functional: Thermochemistry with a kinetic energy density dependent exchange-correlation functional," *J. Chem. Phys.*, vol. 112, no. 6, pp. 2643–2649, Feb. 2000, doi: 10.1063/1.480838.

[34] P. Borlido, T. Aull, A. W. Huran, F. Tran, M. A. L. Marques, and S. Botti, "Large-Scale Benchmark of Exchange–Correlation Functionals for the Determination of Electronic Band Gaps of Solids," *J. Chem. Theory Comput.*, vol. 15, no. 9, pp. 5069–5079, Sep. 2019, doi: 10.1021/acs.jctc.9b00322.

[35] A. D. Becke and E. R. Johnson, "A simple effective potential for exchange," *J. Chem. Phys.*, vol. 124, no. 22, p. 221101, Jun. 2006, doi: 10.1063/1.2213970.

[36] D. Koller, F. Tran, and P. Blaha, "Improving the modified Becke-Johnson exchange potential," *Phys. Rev. B*, vol. 85, no. 15, p. 155109, Apr. 2012, doi: 10.1103/PhysRevB.85.155109.

[37] A. D. Becke and M. R. Roussel, "Exchange holes in inhomogeneous systems: A coordinate-space model," *Phys. Rev. A*, vol. 39, no. 8, pp. 3761–3767, Apr. 1989, doi: 10.1103/PhysRevA.39.3761.

CHAPTER 2

PSEUDOPOTENTIAL PLANE-WAVE METHOD

2.1 Introduction

During the early 1980s, the electronic structure literature was dominated by plane wave-based pseudopotential methods, despite the emergence of density functional calculations and ab initio total energy methods. Today, a similar parallel can be observed with the advent of ab initio molecular dynamics using the Car-Parrinello (CP) method [1], which significantly enhances plane wave-based density functional methods, allowing the solution of previously challenging problems. However, there has been limited application of these ideas to non-plane wave-based methods. This early dominance of plane wave methods was primarily due to the simplicity of plane waves, making their development and implementation straightforward, even though other methods may have offered computational advantages. As non-plane wave CP-like codes are developed, new possibilities may emerge, but their impact on certain problems, such as high-temperature superconductors, is yet to be seen. This chapter aims to stimulate efforts to explain the PW, providing a review of plane wave pseudopotential and CP methods as groundwork for further research. For more detailed information, readers are referred to existing literature, including the reviews of *Payne et al* [2]. (For CP and related methods) and Pickett [3] and Cohen [4], as well as relevant papers [5] on planewave pseudopotential methods.

2.2 Plane Waves

2.2.1 Bloch's theorem

With Bloch's theorem, we can describe electronic states in a crystalline material by considering a plane wave with a crystal momentum k modulated by a periodic function with the same periodicity as the lattice. The periodicity ensures that the wave functions retain their form within each unit cell, facilitating the understanding of electronic properties in periodic systems. This fundamental theorem has been instrumental in shaping the field of condensed matter physics and understanding the electronic structure of crystalline materials.

Bloch's theorem, based on the periodicity of the crystal lattice, establishes the crystal momentum k as a conserved quantum number and provides the boundary condition for the single-particle wave functions:

$$\varphi_k(r + R_L) = e^{ik.R_L}\varphi_k(r) \qquad (2.1)$$

Were R_L is a direct lattice vector. The most general solution that satisfies this boundary condition is

$$\varphi_k(r) = e^{ikr}\sum_G c_G(k)e^{iGr} = e^{ikr}\omega(k,r) \qquad (2.2)$$

Where the *G* are reciprocal lattice vectors.

The Fermi liquid theory (FLT) explains how electrons and nuclei strongly interact through the Coulomb potential in solids. However, FLT suggests that near the Fermi energy, electrons in metals behave as independent particles called quasi particles, with renormalized masses and intensities but no interactions at low energies. This theory is foundational in understanding metals and guiding band structure methods. The pseudopotential approximation deals with the strong interactions of core electrons and nuclei. It replaces the strong core potential with a pseudopotential that mimics the all-electron valence wave function outside a selected core radius. While this simplifies calculations, generating and using pseudopotentials adds complexity to the method. The frozen core approximation is generally reliable, except for elements with extended core states.

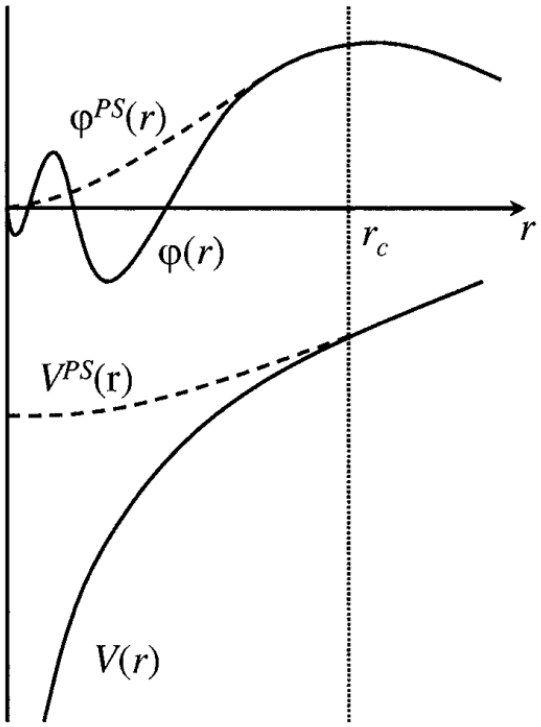

Fig. 2.1: Schematic illustration of the replacement of the all-electron wave function and core potential by a pseudo-wave function and pseudopotential [6].

2.2.2 *Cut-off* energy

When using a PW-DFT code, there is a parameter within the input file that enables you to define an energy cut-off. This cut-off is essential due to the impracticality of achieving a full expansion encompassing an infinite number of plane waves. Nonetheless, it can be demonstrated that the influence of higher-frequency plane waves is overshadowed by that of the lower-frequency ones. Hence, it becomes a feasible approach to implement a certain cut-off, selecting only those wave vectors that meet the criteria. The reciprocal lattice vectors residing within this sphere are included in the basis set. Instead of using K_{max}, the *cut-off* energy is frequently designated as the free electron energy corresponding to K_{max}

$$E_{cut} = \frac{\hbar^2 K_{\max}^2}{2m_e} \qquad (2.3)$$

Limiting the plane-wave basis set using a finite cut-off energy introduces an error in the calculated total energy. Nonetheless, elevating the cut-off energy can mitigate this error. In theory, by expanding the basis set with a larger energy cut-off, the error can be minimized extensively, showcasing a primary benefit of plane wave bases. Conversely, a drawback of these bases involves their demand for numerous plane waves to depict localized states characterized by intense wave function oscillations. To address this challenge, the pseudopotential approximation can be employed.

2.3 Pseudopotentials

2.3.1 The Phillips-Kleinman Construction

The pseudopotential approach started with the orthogonalized plane wave (OPW) method [7]. This method expanded valence wave functions using orthogonalized plane waves to the core states, φ_c .

$$\phi_{OPW}(k+G) = \phi_{PW}(k+G) - \sum_{\alpha,c} < \varphi_c \left| \phi_{PW}(k+G) > \varphi_{\alpha,c} \right. \qquad (2.4)$$

Where ϕ_{PW} and ϕ_{OPW} is a plane wave and the corresponding OPW, respectively, and the sum is over core states and atoms.

A pseudopotential related to this approach, may be constructed as follows: Let *H* be the original Hamiltonian with core and valence wave functions, φ_c and φ_v respectively,

meanwhile $\varepsilon_{\alpha,c}$ and ε_v are the core and valence eigenvalues, respectively, the pseudo states satisfy a Schrodinger-like equation with an additional contribution, V^R to the Hamiltonian:

$$V^R = \sum_{\alpha,c} (\varepsilon_v - \varepsilon_{\alpha,c}) \left| \varphi_{\alpha,c} > < \varphi_{\alpha,c} \right| \qquad (2.5)$$

Where the Phillips-Kleinman [8] pseudopotential, V^{PK} is yielded from where V^R (it differs from a normal potential term in that it is energy dependent through ε_v) and the original potential, V

$$V^{PK} = V + V^R \qquad (2.6)$$

Beyond the core region, V^{PK} approaches V as the core wave functions disappear, indicating a certain radius, r_c around an atom where the atom's contribution to V^R becomes negligible. The construction is linear, with each atom α a making a distinct and independent additive contribution. Importantly, due to the additional repulsive contribution in the core, the pseudopotential is generally significantly weaker than the original potential, leading to a reasonable convergence of plane wave expansions for the pseudo-wave functions.

2.3.2 Norm Conserving Pseudopotentials

Significant advancements have taken place in the sophistication and effectiveness of pseudopotentials since the Phillips-Kleinman construction. This progression has largely been influenced by the following objectives:

1 Primarily, the aim is to ensure that the pseudopotential possesses maximum softness, facilitating the expansion of valence pseudo-wave functions using minimal plane waves.

2 Additionally, it should exhibit a high degree of transferability, ensuring accurate reproduction of other atomic configurations. This quality is particularly crucial for ensuring reliability in solid-state applications, where the crystal potential differs inherently from the atomic potential.

3 Moreover, the precision of reproducing the valence charge density is a key consideration in constructing the pseudo-charge density from pseudo-wave functions.

The notion of norm-conservation [9,10] has played a pivotal role in harmonizing these competing objectives. Norm-conserving pseudopotentials represent a significant advancement in this regard. In these pseudopotentials, the pseudo-wave functions and potential are designed to match the actual valence wave functions and potential beyond a specific core

radius, denoted as r_c. Within the radius r_c, the pseudo-wave functions diverge from the true wave functions, while still maintaining the same norm constraint. That is

$$\int_0^{r_c} dr\ r^2 \varphi^{PS*}(r)\varphi^{PS}(r) = \int_0^{r_c} dr\ r^2 \varphi^{*}(r)\varphi(r) \qquad (2.7)$$

The atomic reference state is characterized by wave functions, with enforced spherical symmetry. It's important to note that these wave functions and eigenvalues differ across various angular momenta, denoted as *l*. This distinction highlights the necessity for the pseudopotential to be *l*-dependent. Such pseudopotentials are commonly termed semi-local. A way to gauge transferability involves examining the logarithmic derivatives at r_c of both the all-electron and pseudo-wave functions, namely φ and φ^{PS}. By equating these derivatives for $r > r_c$ it is ensured that the logarithmic derivatives at r_c also match for the atomic reference configuration.

$$\frac{1}{\varphi^{PS}(r_c,E)}\frac{d\varphi^{PS}(r_c,E)}{dr} = \frac{1}{\varphi(r_c,E)}\frac{d\varphi(r_c,E)}{dr} \qquad (2.8)$$

In the context where E represents the reference energy, the final equation remains valid only when E corresponds precisely to the atomic reference eigenvalue. The extent of validity of this last equation is determined by the range of E values for which it remains applicable. This determination involves the application of Green's theorem, as elaborated in the work by Shaw and Harrison [11].

$$-\frac{\partial}{\partial E}\frac{\partial}{\partial r}\ln\varphi(r_c,E) = \frac{1}{r_c^2\varphi^{*}(r_c,E)\varphi(r_c,E)}\int_0^{r_c} dr\ r_c^2\varphi^{*}(r_c,E)\varphi(r_c,E) \qquad (2.9)$$

Consequently, the application of norm-conservation not only guarantees the matching of logarithmic derivatives between the pseudo- and all-electron wave functions at the reference energy but also ensures alignment in the first derivative concerning *E*. As a result, the disparity in logarithmic derivative between pseudo- and all-electron forms becomes a second-order effect in the deviation from the reference point, contributing to the establishment of transferability for norm-conserving pseudopotentials. Approaches for constructing soft-core, semi-local norm-conserving pseudopotentials were pioneered by *Hamann et al*.[12], and subsequently refined by *Bachelet et al.* [13] (BHS), who compiled precise pseudopotential data for all periodic table elements. An alternative methodology was presented by Kerker [14], yielding pseudopotentials of similar quality. This technique

employs uncomplicated analytical representations for the pseudo-wave functions within a specific range r_c. Troullier and Martins [15], [16] further enhanced this method, which is widely employed today for generating norm-conserving pseudopotentials used in practical computations.

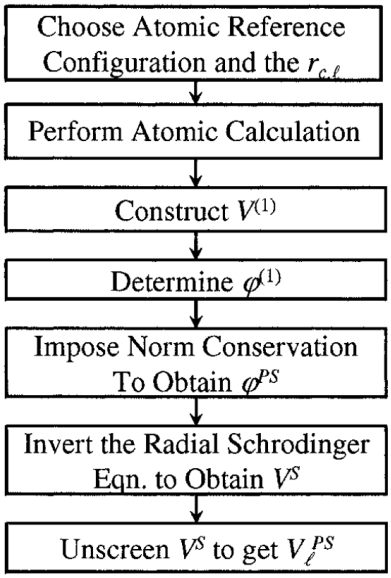

Fig. 2.2: Bachelet, Hamann and Schluter procedure for generating norm-conserving pseudopotentials [6].

The significant achievement of BHS tabulation was the separation of ab initio calculations from the process of pseudopotential generation. This separation greatly reduced the initial difficulty of entering the field. This change is likely one of the reasons for the subsequent uptick in activity within plane wave pseudopotential investigations of solids.

2.3.3 The Kleinman-Bylander Transformation

The challenge with above pseudopotentials: one radial variable for plane waves, separate evaluation of angular integrals. The fully nonlocal approach separates integrals. Transformation starts from semilocal form with V_l. Pseudo wave functions φ_l^{PS} match potential. New pseudopotential has local (V_L) and nonlocal (V_{NL}) parts. V_{NL} localized after subtracting local [17].

$$\hat{V}_{NL} = \sum_l \hat{V}_l^{NL} = \sum_{lm} \frac{\left|\hat{V}_l^{SL}\varphi_{lm}^{PS}\right\rangle\left\langle\varphi_{lm}^{PS}\hat{V}_l^{SL}\right|}{\left\langle\varphi_{lm}^{PS}\left|\hat{V}_l^{SL}\right|\varphi_{lm}^{PS}\right\rangle} \qquad (2.10)$$

With

$$\hat{V}_l^{NL}\left|\varphi_{lm}^{PS}\right\rangle = \hat{V}_l^{SL}\left|\varphi_{lm}^{PS}\right\rangle \qquad (2.11)$$

To observe this, let's employ this operator on the pseudo wave function. Within the plane wave representation, we can examine any arbitrary matrix element of the Kleinman-Bylanderized pseudopotential.

$$\left\langle \vec{q}\left|\hat{V}_l^{NL}\right|\vec{q}'\right\rangle = \sum_{lm}\frac{\left\langle \vec{q}\left|\hat{V}_l\varphi_{lm}^{PS}\right\rangle\left\langle\hat{V}_l\varphi_{lm}^{PS}\right|\vec{q}'\right\rangle}{\left\langle\varphi_{lm}^{PS}\left|\hat{V}_l\right|\varphi_{lm}^{PS}\right\rangle} \qquad (2.12)$$

2.3.4 Ultrasoft pseudopotentials

In 1990, Vanderbilt introduced an innovative and revolutionary approach to creating pseudopotentials by loosening the norm-conservation limitation. Pseudopotentials produced using this method (owing to their pliancy) necessitate a significantly reduced plane wave cut-off and consequently fewer plane waves. Hence, they are commonly referred to as "ultrasoft" pseudopotentials [18]. The total energy with the inclusion of ultrasoft pseudopotentials is formulated as follows:

$$E_e = \sum_i\sum_i\left\langle\varphi_i\left|-\frac{1}{2}\nabla^2+V_{NL}\,\varphi_i\right\rangle\right. + \frac{1}{2}\int\int d\vec{r}d\vec{r}'\,\frac{n(\vec{r})n(\vec{r}')}{\left|\vec{r}-\vec{r}'\right|} + E_{XC}[n] + \int d\vec{r}'V_{loc}(\vec{r})n(\vec{r}) \qquad (2.13)$$

The customary structure encompasses the Hartree, exchange-correlation, local, and kinetic components. Conversely, the nonlocal segment of the pseudopotential is presented utilizing a novel collection of projection operators:

$$V_{NL} = D_{nm}^{(0)}\left|\beta_n^I\right\rangle\left\langle\beta_m^I\right| \qquad (2.14)$$

where the superscript *I* denotes the atom around which the projector is centred. The strict adherence to the norm-conserving condition is eased by incorporating a comprehensive orthonormality requirement using the overlap matrix S

$$\left\langle\varphi_i\left|S\right|\varphi_j\right\rangle = \delta_{ij} \qquad (2.15)$$

Where

$$S = 1+\sum_{nm,I} q_{nm}\left|\beta_n^I\right\rangle\left\langle\beta_m^I\right| \qquad (2.16)$$

With

$$q_{nm} = \int d\vec{r} Q_{nm}(\vec{r}) \qquad (2.17)$$

Commencing with the density, even though it offers the advantage of crafting milder pseudopotentials, it unavoidably leads to heightened intricacy in the Kohn-Sham equations. The variational differentiation of the density concerning the orbitals is:

$$\frac{\delta n(\vec{r}')}{\delta \varphi_i^*(\vec{r})} = \varphi(\vec{r})\delta(\vec{r}-\vec{r}') + \sum_{nm,I} Q_{nm}^I(\vec{r}')\beta_n^I(\vec{r})\left\langle \beta_m^I \middle| \varphi_i \right\rangle \qquad (2.18)$$

We arrive at the modified Kohn-Sham equations

$$\frac{\delta E_e}{\delta \varphi_i^*} = \int d\vec{r}' \frac{\delta E_e}{\delta n(\vec{r}')}\frac{\delta n(\vec{r}')}{\delta \varphi_i^*(\vec{r})} = \left[-\frac{1}{2}\nabla^2 + V_{eff} + \left(D_{nm}^{(0)} + \int d\vec{r}' V_{eff}(\vec{r}') Q_{nm}(\vec{r}') \right) \middle| \beta_n^I \right\rangle \left\langle \beta_m^I \middle| \right] \middle| \varphi_i \right\rangle \qquad (2.19)$$

Where V_{eff} is the regular potential

$$V_{eff} = V_H + V_{loc} + V_{XC} \qquad (2.20)$$

As evident from the altered Kohn-Sham equations, in contrast to norm-conserving pseudopotentials, the coefficients of the projectors in the nonlocal segment of the pseudopotential are consistently adjusted during each iteration in a self-consistent fashion. While this does add a minor computational burden, the benefits in the plane wave expansion outweigh the resultant drawback.

References

[1] R. Car and M. Parrinello, "Unified Approach for Molecular Dynamics and Density-Functional Theory," *Phys. Rev. Lett.*, vol. 55, no. 22, pp. 2471–2474, Nov. 1985, doi: 10.1103/PhysRevLett.55.2471.

[2] M. C. Payne, M. P. Teter, D. C. Allan, T. A. Arias, and J. D. Joannopoulos, "Iterative minimization techniques for ab initio total-energy calculations: molecular dynamics and conjugate gradients," *Rev. Mod. Phys.*, vol. 64, no. 4, pp. 1045–1097, Oct. 1992, doi: 10.1103/RevModPhys.64.1045.

[3] W. E. Pickett, "Pseudopotential methods in condensed matter applications," *Comput. Phys. Rep.*, vol. 9, no. 3, pp. 115–197, Apr. 1989, doi: 10.1016/0167-7977(89)90002-6.

[4] M. L. Cohen, "Electronic structure of solids," *Phys. Rep.*, vol. 110, no. 5, pp. 293–309, Aug. 1984, doi: 10.1016/0370-1573(84)90192-3.

[5] J. T. Devreese and P. Van Camp, Eds., *Electronic Structure, Dynamics, and Quantum Structural Properties of Condensed Matter*. Boston, MA: Springer US, 1985. doi: 10.1007/978-1-4757-0899-8.

[6] D. J. Singh , L. Nordström, *Planewaves, Pseudopotentials and the LAPW Method*. Springer US, 2006. doi: 10.1007/978-0-387-29684-5.

[7] C. Herring, "A New Method for Calculating Wave Functions in Crystals," *Phys. Rev.*, vol. 57, no. 12, pp. 1169–1177, Jun. 1940, doi: 10.1103/PhysRev.57.1169.

[8] J. C. Phillips and L. Kleinman, "New Method for Calculating Wave Functions in Crystals and Molecules," *Phys. Rev.*, vol. 116, no. 2, pp. 287–294, Oct. 1959, doi: 10.1103/PhysRev.116.287.

[9] W. C. Topp and J. J. Hopfield, "Chemically Motivated Pseudopotential for Sodium," *Phys. Rev. B*, vol. 7, no. 4, pp. 1295–1303, Feb. 1973, doi: 10.1103/PhysRevB.7.1295.

[10] Th. Starkloff and J. D. Joannopoulos, "Local pseudopotential theory for transition metals," *Phys. Rev. B*, vol. 16, no. 12, pp. 5212–5215, Dec. 1977, doi: 10.1103/PhysRevB.16.5212.

[11] R. W. Shaw and W. A. Harrison, "Reformulation of the Screened Heine-Abarenkov Model Potential," *Phys. Rev.*, vol. 163, no. 3, pp. 604–611, Nov. 1967, doi: 10.1103/PhysRev.163.604.

[12] D. R. Hamann, M. Schlüter, and C. Chiang, "Norm-Conserving Pseudopotentials," *Phys. Rev. Lett.*, vol. 43, no. 20, pp. 1494–1497, Nov. 1979, doi: 10.1103/PhysRevLett.43.1494.

[13] G. B. Bachelet, D. R. Hamann, and M. Schlüter, "Pseudopotentials that work: From H to Pu," *Phys. Rev. B*, vol. 26, no. 8, pp. 4199–4228, Oct. 1982, doi: 10.1103/PhysRevB.26.4199.

[14] G. P. Kerker, "Non-singular atomic pseudopotentials for solid state applications," *J. Phys. C Solid State Phys.*, vol. 13, no. 9, p. L189, Mar. 1980, doi: 10.1088/0022-3719/13/9/004.

[15] N. Troullier and J. L. Martins, "Efficient pseudopotentials for plane-wave calculations," *Phys. Rev. B*, vol. 43, no. 3, pp. 1993–2006, Jan. 1991, doi: 10.1103/PhysRevB.43.1993.

[16] N. Troullier and J. L. Martins, "Efficient pseudopotentials for plane-wave calculations. 2. Operators for fast iterative diagonalization," *Phys. Rev. B*, vol. 43, no. 11, pp. 8861–8869, Apr. 1991, doi: 10.1103/PhysRevB.43.8861.

[17] L. Kleinman and D. M. Bylander, "Efficacious Form for Model Pseudopotentials," *Phys. Rev. Lett.*, vol. 48, no. 20, pp. 1425–1428, May 1982, doi: 10.1103/PhysRevLett.48.1425.

[18] D. Vanderbilt, "Soft self-consistent pseudopotentials in a generalized eigenvalue formalism," *Phys. Rev. B*, vol. 41, no. 11, pp. 7892–7895, 1990, doi: 10.1103/PhysRevB.41.7892.

CHAPTER 3

FULL-POTENTIAL LINEARIZED AUGMENTED PLANE-WAVE METHOD

3.1 Introduction

When selecting a basis set, there are two objectives to pursue. Firstly, it's advantageous for the basis functions to possess maximum mathematical simplicity. This simplification aids in streamlining the calculation of matrix elements. Conversely, the second significant criterion, which can sometimes appear contradictory to the first, involves having basis functions that are adept at representing the specific system in question. Consequently, a trade-off arises between solving a greater number of relatively straightforward equations or dealing with fewer yet more intricate ones.

3.2 The Augmented Plane wave (APW) method

The LAPW method represents a modification of Slater's original augmented plane wave (APW) approach [1]. Therefore, prior to delving into an explanation of the LAPW method, we will revisit the pertinent components of the APW method and the rationale behind its transformation into the LAPW method. Additional insights into the APW method can be obtained from Loucks' book [2], which includes reprints of several initial papers detailing the formulation and application of this technique. Within the interstitial space separating the atoms, both the potential and wave functions exhibit smoother behaviours. As a result, space is divided into distinct regions, and distinct basis expansions are employed within these regions: for the inner non-overlapping atom-centered spheres, radial solutions of Schrödinger's equation are employed, while plane waves are used in the remaining interstitial region **(Fig. 3.1**).

$$\varphi(r) = \begin{cases} \Omega^{-1/2} \sum_G C_G e^{i(G+k)r} & \text{r}\in\text{I} \\ \sum_{lm} A_{lm} u_l(r) Y_{lm}(r) & \text{r}\in S \end{cases} \qquad (3.1)$$

Where φ is a wave function, Ω is the cell volume, $u_l(r)$ is

$$\left[-\frac{d^2}{dr^2} + \frac{l(l+1)}{r^2} + V(r) - E_l \right] r u_l(r) = 0 \qquad (3.2)$$

In this context, the expansion coefficients are denoted as C_G and A_{lm}, while E_l represents a parameter. V stands for the spherical segment of the potential within the sphere, and all values are assumed to be in Rydberg units. The radial functions, as defined by last equation, possess inherent orthogonality with respect to any eigenstate of the identical Hamiltonian that becomes zero at the boundary of the sphere [3]. This characteristic is illustrated by observing

its origin in Schrödinger's equation.

$$(E_2 - E_1) r u_1(r) u_2(r) = u_2 \frac{d^2 r u_1(r)}{dr^2} - u_1 \frac{d^2 r u_2(r)}{dr^2} \qquad (3.3)$$

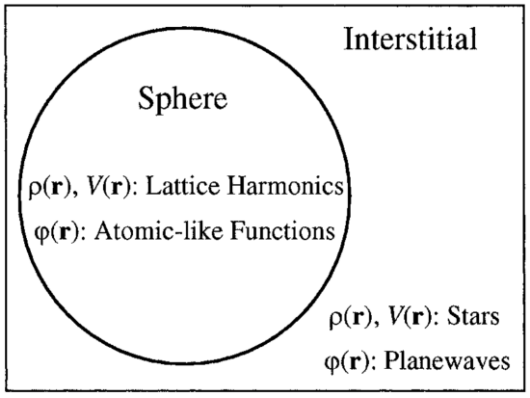

Fig. 3.1: The dual representation of the APW and LAPW methods. Stars and lattice harmonics are symmetrized plane waves and spherical harmonics used to represent the density and potential [4].

The radial solutions, represented as $u_1(r)$ and $u_2(r)$, correspond to different energies E_1 and E_2, respectively. The construction of the overlap involves utilizing this relationship and employing integration by parts. If either $u_1(r)$ or $u_2(r)$ vanishes at the sphere boundary, the surface terms disappear, and the remaining terms cancel out. Slater justifies the selection of these specific functions by observing that plane waves serve as solutions to Schrödinger's equation within a constant potential, while the radial functions act as solutions within a spherical potential, given that E_l matches the eigenvalue. Although this approximation of the potential is rough, it remains viable in certain scenarios. Notably, the muffin-tin (MT) approximation, widely employed in APW codes, has been instrumental in elucidating properties of transition metals and compounds. This approximation performs excellently for densely packed materials like face-centered cubic (*fcc*) and those with an ideal *c/a hcp*. For materials with a body-centered cubic (*bcc*) or related structures such as CsCl, the MT approximation is less precise but still viable [5]. As the symmetry of sites and coordination diminishes, the reliability of this approximation progressively wanes. An additional aspect to consider is the continuity of the dual representation defined by Eqn. (3.1) at sphere boundaries, a requisite for well-defined kinetic energy. Thus, imposing this constraint becomes necessary. In the APW method, achieving this is accomplished by defining the coefficients A_{lm} through the spherical harmonic expansion of plane waves, with each *lm* component's coefficient matching at the sphere boundary

$$A_{lm} = \frac{4\pi i^l}{\Omega^{1/2} u_l(R)} \sum_G C_G j_l(|k+G|R) Y_{lm}^*(k+G) \qquad (3.4)$$

The centre of the sphere serves as the reference origin, with the sphere radius denoted as *R*. Consequently, the determination of A_{lm} relies entirely on the coefficients of planewaves denoted as C_G and the energy parameters labeled as E_l. These coefficients and parameters represent the variational components within the APW method. The specific functions, characterized by the label *G*, are composed of individual plane waves in the interstitial region, harmonized with radial functions within the spheres. These merged plane waves are referred to as augmented plane waves or APWs.

In the scenario where E_l is considered a constant parameter rather than a variable coefficient, the APW method would essentially entail utilizing the APWs as a foundational basis. While the APWs offer solutions to Schrödinger's equation within the spheres, these solutions are limited to the energy E_l. They lack the flexibility required for accommodating changes in the wave function as the band energy deviates from this reference value. Consequently, E_l must be equated with the band energy, implying that energy bands (at a fixed k-point) cannot be derived through a simple diagonalization process. Another challenge associated with the APW method pertains to its extension to a broader crystal potential, surpassing the constraints of the muffin-tin approximation (utilizing a general potential in the interstitial region while retaining a spherical potential within the spheres). This complexity arises because the optimal variational selection of E_l no longer aligns with setting E_l to the band energy. Specifically, various bands are likely to possess distinct orbital characteristics within the sphere (e.g., d_{z^2} versus $d_{x^2} - d_{y^2}$). However, under non-spherical potentials, these orbitals encounter varying effective potentials, which deviate from the spherical average utilized for determining the radial function. Despite these challenges, it's worth noting that extending the APW method beyond the warped muffin-tin approximation is not entirely impossible and has been explored in some instances [5,6].

An additional, less severe issue with the APW technique involves the so-called asymptote problem. Within the formula (Eqn. 3.4) for the matching coefficient, the term A_{lm}, $u_l(R)$ emerges in the denominator. Nonetheless, there exist instances of the energy parameter, E_l, for which u_l becomes negligible at the boundary of the sphere. At these specific energy levels, the interplay between plane waves and radial functions becomes disconnected. In the vicinity of this asymptotic scenario, the relationship between A_{lm}, the Clebsch-Gordan coefficients C_G,

and consequently the secular determinant, exhibits significant fluctuations. This phenomenon leads to computational challenges when energy bands align closely with an asymptote. Moreover, caution is essential in the proximity of an asymptote to guarantee accurate counting of eigenvalues. Various modifications to the APW approach were proposed before 1975 to tackle these challenges. Bross and colleagues [7] presented an altered APW technique, where multiple radial functions selected to possess identical logarithmic derivatives are matched with plane waves. This matching necessitates continuity in both the wave function's value and its first derivative. This strategy, akin to the LAPW method, enables the determination of all band energies through a single diagonalization process. Koelling introduced an alternative, yet related, approach utilizing two radial functions. One function assumes a zero value at the sphere boundary, while the other has zero slope [8]. These functions, derived by solving the radial equation subject to these boundary conditions, are then matched to plane waves to ensure continuity of the basis functions and their first derivatives. A potential challenge with this method arises from the fact that enforcing the boundary conditions at the sphere radius can result in basis functions that blend regular and irregular solutions, potentially failing to meet the physical boundary conditions at the nucleus. Nonetheless, Koelling demonstrated that this approach improves convergence for d-bands of transition metals. Similar to the Bross procedure, the asymptote problem does not manifest here. Other enhancements were explored by Marcus. Andersen [3], [9] extended this work by proposing a method in which the basis functions and their derivatives achieve continuity by matching to a radial function at a fixed E_l along with its derivative with respect to E_l. This choice effectively addressed the aforementioned issues with the APW method and additionally provided a flexible and accurate technique for modelling band structures. This method is known as the LAPW method. As expected, initial LAPW computations [9] were conducted within the muffin-tin (MT) approximation and employed a model potential. However, shortly thereafter, fully self-consistent codes were developed for both slab [10-12] and bulk [13] systems, eliminating any approximation to the charge density or potential (referred to as full-potential). This ushered in a phase of general potential calculations [13-19]. During this period, the method's power and accuracy were showcased primarily through a series of electronic structure calculations involving surfaces and adsorbates (for a comprehensive review, refer to *Wimmer et al*. [20]). These demonstrations firmly established the LAPW method as the preferred choice for precise electronic structure calculations in materials containing transition metal atoms.

3.3 The Linearized Augmented Plane wave (LAPW) method

The LAPW method, a conventional approach to linearize the APW method, emerged in the early 1970s [3,4]. In this strategy, the expansion of basis functions occurs in a manner akin to Eq. (3.1) in the interstitial region. However, within the muffin tin, these basis functions are influenced not only by $u_l(r)$ but also by its derivative.

$$u_l(r) \equiv \partial u_l / \partial E$$

$$\varphi(r) = \begin{cases} \Omega^{-1/2} \sum_G C_G e^{i(G+k)r} & r \in I \\ \sum_{lm} [A_{lm} u_l(r) + B_{lm} \dot{u}_l(r)] Y_{lm}(r) & r \in S \end{cases} \qquad (3.5)$$

This results in the LAPW approach being more versatile than the APW approach. This is due to its capability to approximate the radial function $u_l(r)$ through a Taylor expansion when dealing with linearization energies E_l that are only marginally distinct from the actual eigenenergy E.

$$u_l(r,E) = u_l(r,E_l) + (E - E_l) u_l(r,E) + O((E - E_l)^2) \qquad (3.6)$$

The introduction of an additional term $O((E - E_l)^2)$ leads to a second-order error in the wave function and a fourth-order error in the eigenenergy. However, the coefficients A_{lm}, B_{lm} are not determined by the Taylor expansion, but by ensuring both the value and slope of the augmented function match a plane wave at R_{MT}. The linearization of the APWs resolves the issue of energy-dependent basis functions, but it comes at the expense of sacrificing the optimal shape of the basis functions within the muffin-tin sphere.

3.3.1 Semi-Core State

In the LAPW technique, there exists a singular linearization energy (denoted as E_1) corresponding to each l quantum number. This situation poses a challenge when dealing with systems that encompass states sharing the same l quantum number, yet possessing distinct n quantum numbers, consequently giving rise to distinctly disparate energies. This issue predominantly arises in systems featuring semi-core states, which reside not within the valence region but also lack the same low-energy status as core states. To address this, the LAPW method introduces localized orbitals to handle semi-core states. These localized orbitals remain uninfluenced by **k** and **G** variables, being exclusive to a single atom and

possessing a specific l characteristic. Referred to as *local* due to their confinement within muffin-tin spheres, they remain non-existent within the interstitial spaces.

$$\varphi^{LO}(r)=\begin{cases}0 & r\in I\\ \sum_{lm}[A_{lm}u_l(r,E_1)+B_{lm}\dot{u}_l(r,E_1)+C_{lm}u_l(r,E_2)]Y_{lm}(r) & r\in S\end{cases} \quad (3.7)$$

Within the confines of the muffin-tin spheres, local orbitals encompass an extra radial function that is assessed at a fresh linearization energy E_2. Two of the coefficients are ascertained based on the stipulation that both the value and the initial derivative of the local orbitals reach zero at the boundary of the sphere. As for the third coefficient, it can be assigned a specific constant value, such as unity. The resultant LAPW+LO basis set proves effective in adequately representing both the valence region and the already well-localized semi-core states.

3.4 APW+lo

An alternative approach for linearizing the APW method is the APW+local orbitals technique [21-23]. In this method, the eigenvalue problem is linearized by selecting a constant linearization energy of E_1. However, the increased flexibility is not achieved by introducing an extra term to the original APW basis functions. Instead, it involves incorporating a supplementary collection of local orbitals.

$$\varphi^{lo_1}(r)=\begin{cases}0 & r\in I\\ \sum_{lm}[A_{lm}u_l(r,E_1)+B_{lm}\dot{u}_l(r,E_1)]Y_{lm}(r) & r\in S\end{cases} \quad (3.8)$$

Each of these local orbitals is designed to have zero value at the boundary of the sphere, without imposing any limitations on the derivatives at the muffin-tin boundaries. Consequently, a surface component for the kinetic energy needs to be considered [4]. The APW+lo complete basis set is made up of two distinct categories of basis functions. Firstly, the APWs (as defined in Eqn. 3.1) characterized by a consistent linearization energy of E_1. Secondly, the lo's (as described in Eqn. 3.8). This defines the basis set configuration.

$$\varphi_i=\begin{cases}\varphi_i^{APW} & i\le N_{APW}\\ \varphi_i^{lo_1} & i\le N_{APW}\end{cases} \quad (3.9)$$

In this context, N_{APW} denotes an integer value dependent on the total size of the basis set and the quantity of included local orbitals. A notable advantage of this alternative linearization, in comparison to the LAPW method, is its ability to maintain the optimal shape of the basis

functions within the muffin-tin. This preservation of shape leads to an improved representation of the eigenstate and subsequently reduces the necessary basis set size to achieve the same level of accuracy.

Similar to the LAPW approach, where there exists a sole linearization energy (denoted as E_1) for each angular momentum quantum number *l*, a challenge arises when attempting to depict semi-core states. However, in the APW+lo method, these semi-core states are managed through an additional collection of localized orbitals.

$$\varphi^{lo_2}(r) = \begin{cases} 0 & r \in I \\ \sum_{lm} [A_{lm} u_l(r, E_1) + C_{lm} u_l(r, E_2)] Y_{lm}(r) & r \in S \end{cases} \qquad (3.10)$$

Once more, the local orbital emerges alongside a secondary linearization energy of E_2. This energy can be intentionally positioned within the semi-core zone, allowing for appropriate treatment of eigenstates that share the same quantum number 'l' but possess varying principal quantum numbers, denoted as *n*. Furthermore, these local orbitals are seamlessly aligned to a zero value at the spherical boundary, and this alignment does not impose any constraints on the initial derivative.

3.5 Mixed Augmentation

Madsen et al. [23] demonstrated that the APW+lo approach generally achieves quicker convergence than the LAPW method. This implies that comparable accuracy in metrics like total energy can be attained using a smaller basis set in the APW+lo method as opposed to the LAPW method. Typically, additional localized orbitals (lo's) are only necessary to extend the expansion up to the physical *l* quantum numbers, encompassing the *l* quantum numbers within the electronic configuration of the relevant element. On the contrary, higher l quantum numbers are adequately addressed by pure APW's. Nevertheless, certain scenarios may demand supplementary lo's for higher quantum numbers in the supplementary basis set, which mitigates the advantage gained in basis set reduction. Conversely, radial functions devoid of significant *l-character* do not notably benefit from the precise shape of the u_l function. Thus, a combined augmentation strategy was proposed [23], in which the crucial I quantum numbers are treated with APW+lo and the higher l quantum numbers are augmented via LAPW. This hybrid approach is referred to as the (L)APW+lo method. All findings presented in this study were acquired using the hybrid (L)APW+lo methodology.

3.6 The full potential (L)APW+lo method

Enhanced precision of the (L)APW+lo approach can be achieved through the utilization of the complete potential (FP). This involves substituting the constant muffin-tin potential with a variable potential in the interstitial region and a non-spherical component within the muffin-tin.

$$V(r) = \begin{cases} \sum_{G} V_G e^{iGr} & r \in I \\ \sum_{lm} Vlm(r) Y_{lm}(\hat{r}) & r \in S \end{cases} \qquad (3.11)$$

These enhancements are also termed non-muffin-tin corrections. The selection of basis functions in the interstitial domain remains unaffected by these corrections. However, the radial functions u, as defined in Eqn. (3.2), cease to be the exact solutions within the muffin-tin sphere. In theory, to accurately evaluate function u_l, the actual crystal potential of the muffin-tin area should be employed. Nevertheless, significant improvements in results are not anticipated, as the non-muffin-tin corrections introduce only minor modifications to the muffin-tin potential. Additionally, the flexibility of basis functions within the linearized APW methods should be sufficient to characterize both the eigenstates influenced by non-muffin-tin corrections and those within the muffin-tin potential.

References

[1] J. C. Slater, "Wave Functions in a Periodic Potential," *Phys. Rev.*, vol. 51, no. 10, pp. 846–851, May 1937, doi: 10.1103/PhysRev.51.846.

[2] S. Blügel and G. Bihlmayer, The Full-Potential Linearized Augmented Plane Wave Method, *Comput. nanosci.: do it yourself*, 2006, vol. 31, pp. 85–129

[3] O. K. Andersen, "Linear methods in band theory," *Phys. Rev. B*, vol. 12, no. 8, pp. 3060–3083, Oct. 1975, doi: 10.1103/Phys. Rev. B.12.3060.

[4] D. J. Singh , L. Nordström, *Planewaves, Pseudopotentials and the LAPW Method*. Springer US, 2006. doi: 10.1007/978-0-387-29684-5.

[5] N. Elyashar and D. D. Koelling, "Effect of non-muffin-tin terms on the electronic structure of transition metals: Niobium," *Phys. Rev. B*, vol. 13, no. 12, pp. 5362–5372, Jun. 1976, doi: 10.1103/PhysRevB.13.5362.

[6] P. D. DeCicco, "Self-Consistent Energy Bands and Cohesive Energy of Potassium Chloride," *Phys. Rev.*, vol. 153, no. 3, pp. 931–938, Jan. 1967, doi: 10.1103/PhysRev.153.931.

[7] H. Bross, G. Bohn, G. Meister, W. Schubö, and H. Stöhr, "New Version of the Modified Augmented-Plane-Wave Method," *Phys. Rev. B*, vol. 2, no. 8, pp. 3098–3103, Oct. 1970, doi: 10.1103/PhysRevB.2.3098.

[8] D. D. Koelling, "Alternative Augmented-Plane-Wave Technique: Theory and Application to Copper," *Phys. Rev. B*, vol. 2, no. 2, pp. 290–298, Jul. 1970, doi: 10.1103/PhysRevB.2.290.

[9] D. D. Koelling and G. O. Arbman, "Use of energy derivative of the radial solution in an augmented plane wave method: application to copper," *J. Phys. F Met. Phys.*, vol. 5, no. 11, p. 2041, Nov. 1975, doi: 10.1088/0305-4608/5/11/016.

[10] O. Jepsen, J. Madsen, and O. K. Andersen, "Band structure of thin films by the linear augmented-plane-wave method," *Phys. Rev. B*, vol. 18, no. 2, pp. 605–615, Jul. 1978, doi: 10.1103/PhysRevB.18.605.

[11] H. Krakauer, M. Posternak, and A. J. Freeman, "Linearized augmented plane-wave method for the electronic band structure of thin films," *Phys. Rev. B*, vol. 19, no. 4, pp. 1706–1719, Feb. 1979, doi: 10.1103/PhysRevB.19.1706.

[12] D. R. Hamann, L. F. Mattheiss, and H. S. Greenside, "Comparative LCAO-LAPW study of C1 chemisorption on the Ag(001) surface," *Phys. Rev. B*, vol. 24, no. 10, pp. 6151–6155, Nov. 1981, doi: 10.1103/PhysRevB.24.6151.

[13] D. R. Hamann, "Semiconductor Charge Densities with Hard-Core and Soft-Core Pseudopotentials," *Phys. Rev. Lett.*, vol. 42, no. 10, pp. 662–665, Mar. 1979, doi: 10.1103/PhysRevLett.42.662.

[14] E. Wimmer, H. Krakauer, M. Weinert, and A. J. Freeman, "Full-potential self-consistent linearized-augmented-plane-wave method for calculating the electronic structure of molecules and surfaces: ${\mathrm{O}}_{2}$ molecule," *Phys. Rev. B*, vol. 24, no. 2, pp. 864–875, Jul. 1981, doi: 10.1103/PhysRevB.24.864.

[15] H. J. F. Jansen and A. J. Freeman, "Total-energy full-potential linearized augmented-plane-wave method for bulk solids: Electronic and structural properties of tungsten," *Phys. Rev. B*, vol. 30, no. 2, pp. 561–569, Jul. 1984, doi: 10.1103/PhysRevB.30.561.

[16] S.-H. Wei and H. Krakauer, "Local-Density-Functional Calculation of the Pressure-Induced Metallization of BaSe and BaTe," *Phys. Rev. Lett.*, vol. 55, no. 11, pp. 1200–1203, Sep. 1985, doi: 10.1103/PhysRevLett.55.1200.

[17] S.-H. Wei, H. Krakauer, and M. Weinert, "Linearized augmented-plane-wave calculation of the electronic structure and total energy of tungsten," *Phys. Rev. B*, vol. 32, no. 12, pp. 7792–7797, Dec. 1985, doi: 10.1103/PhysRevB.32.7792.

[18] L. F. Mattheiss and D. R. Hamann, "Linear augmented-plane-wave calculation of the structural properties of bulk Cr, Mo, and W," *Phys. Rev. B*, vol. 33, no. 2, pp. 823–840, Jan. 1986, doi: 10.1103/PhysRevB.33.823.

[19] P. Blaha, K. Schwarz, P. Sorantin, and S. B. Trickey, "Full-potential, linearized augmented plane wave programs for crystalline systems," *Comput. Phys. Commun.*, vol. 59, no. 2, pp. 399–415, Jun. 1990, doi: 10.1016/0010-4655(90)90187-6.

[20] E. Wimmer, H. Krakauer, and A. J. Freeman, "Theory of Surface Electronic Structure**Parts of this work were supported by the National Science Foundation (DMR

grants no.DMR 81–20550 and DMR 82–16543) and the Office of Naval Research (N00014-81-K-0438).," in *Advances in Electronics and Electron Physics*, P. W. Hawkes, Ed., Academic Press, 1985, pp. 357–434. doi: 10.1016/S0065-2539(08)60881-1.

[21] E. Sjöstedt, "Augmented Planewaves, Developments and Applications to Magnetism," 2002, Accessed: Aug. 22, 2023. [Online]. Available: https://urn.kb.se/resolve?urn=urn:nbn:se:uu:diva-1928

[22] E. Sjöstedt, L. Nordström, and D. J. Singh, "An alternative way of linearizing the augmented plane-wave method," *Solid State Commun.*, vol. 114, no. 1, pp. 15–20, Mar. 2000, doi: 10.1016/S0038-1098(99)00577-3.

[23] G. K. H. Madsen, P. Blaha, K. Schwarz, E. Sjöstedt, and L. Nordström, "Efficient linearization of the augmented plane-wave method," *Phys. Rev. B*, vol. 64, no. 19, p. 195134, Oct. 2001, doi: 10.1103/PhysRevB.64.195134.

PART 2

RESULTS AND DISCUSSION

CHAPTER 1

THE STRUCTURAL, ELECTRONIC, ELASTIC, OPTICAL AND THERMOELECTRIC PROPERTIES OF THE ZINTL-PHASES AE_3GaAs_3 (AE = Sr, Ba)

1.1 Calculation methods and settings

The equilibrium crystalline structure parameters and elastic constants of the considered ternary Zintl phases were determined using the DFT-based pseudopotential plane-wave (PP-PW) method with the GGA-PBEsol functional[1]. This method was implemented in the CASTEP package[2]. Vanderbilt's ultrasoft pseudopotentials [3] were used to describe the interactions between the valence electrons (As: $4s^24p^1$; Ga: $3d^{10}4s^24p^1$; Sr: $4s^23p^2$; Ba: $5s^25p^66s^2$) and the pseudo-ionic cores (nuclei plus frozen core electrons). To ensure accurate total energy convergence, an energy cut-off of 350 eV for the plane-wave basis set and a 5x3x10 special Monkhorst-Pack [4] *k*-points mesh for the Brillouin zone (BZ) sampling were adopted.

To begin this work, the BFGS algorithm (named after Broyden, Fletcher, Goldfarb, and Shannon) [5] was employed to identify the equilibrium structural parameters that correspond to the crystal structure with the lowest energy. The computations were conducted using specific tolerance parameters for achieving convergence:

i. Self-consistent total energy within 5.0×10^{-6} eV/atom.
ii. Maximum force acting on each atom within 0.01eV/Å.
iii. Maximum stress within 0.02GPa
iv. Maximum atomic displacement within 5.0×10^{-4} Å.

To compute the monocrystalline elastic constants (C_{ij}s) of the studied orthorhombic systems, the stress-strain method using the generalized Hooker's law [1] was employed. Three distinct strain tensors are applied to the equilibrium crystal structure to determine the nine independent Cijs required for characterizing the elastic properties; the first strain tensor was with non-zero ε_{11} and ε_{32} components, the second strain tensor was with non-zero ε_{22} and ε_{31} components and the third one was with non-zero ε_{33} and ε_{12} components, The computations are carried out with specific settings, including a total energy convergence of 1.0×10^{-6} eV/atom, a Hellman-Feynman force of 0.002eV/Å, and an ionic displacement of 1.0×10^{-4} Å. Several physical properties that are linked to the C_{ij}s, such as mechanical stability, elastic anisotropy, anisotropic sound wave velocities, and polycrystalline elastic moduli, as well as related properties like bulk modulus, shear modulus, Young's modulus, Poisson's ratio, brittleness/ductility, average sound velocity, and Debye temperature, are determined through established empirical and theoretical relationships [6].

To compute the electronic structure and related properties of the studied materials, the state-of-the-art DFT-based full-potential linearized/augmented plane wave plus local orbitals (FP-L/APW+lo) method was used. The calculations were carried out using both the GGA-PBEsol and [7] Tran-Blaha modified Becke-Johnson (TB-mBJ) potential [8], which was specifically developed to improve the electronic structure of semiconductors and insulators, particularly for better quantitative estimates of their bandgaps. The WIEN2k package [9] was utilized to implement the calculations, with a cut-off parameter of $l_{\max}$=10 for the spherical harmonics basis set and a reciprocal lattice vector cut-off of $K_{\max} = 10 / R_{MT}^{\min}$ for the plane-wave basis set, where $R_{MT}^{\min}$ is the smallest muffin-tin sphere. The radii of the muffin-tin spheres for Sr, Ba, Ga, and As are 2.50 Bohr and 2.34 Bohr, respectively. The self-consistent calculations are considered to have converged when the total energy is stable within 10^{-5} Ry and the force acting on each atom of the system is less than 5×10^{-4} Ry/Bohr.

Linear optical responses of matter to incident electromagnetic radiation are described by the complex dielectric function $\varepsilon(\omega)$; $\varepsilon(\omega) = \varepsilon_1(\omega) + i\varepsilon_2(\omega)$ [10], where the real part ($\varepsilon_1(\omega)$) and the imaginary one ($\varepsilon_2(\omega)$) describe, respectively, the dispersion and the absorption of the electromagnetic radiation by the medium which it crosses. $\varepsilon_2(\omega)$ spectrum is calculated by summing the electric dipole operator matrix elements between the occupied and unoccupied wave functions over the Brillouin zone while respecting the selection rules. $\varepsilon_1(\omega)$ spectrum is calculated from $\varepsilon_2(\omega)$ spectrum using Kramers-Kronig relationship [10]. Spectra of all the other linear optical parameters, including refractive index, extinction coefficient, reflectivity, and absorption coefficient, are deduced from $\varepsilon_1(\omega)$ and $\varepsilon_2(\omega)$ spectra, using the well-known relationships [11]. The transport properties were computed within a dense mesh of 30×30×30 k-points in the BZ using Boltzmann's transport theory with the constant scattering time approximation (CSTA) and the rigid band approximation (RBA) as implemented in the BoltzTraP1 code [12].

1.2 Results and discussion

1.2.1 Structural properties

The compounds Sr_3GaAs_3 and Ba_3GaAs_3, which belong to the ternary Zintl-phase, exhibit an orthorhombic structure characterized by the space group *Pnma* Ba_3GaSb_3-type structure (no. 62), with eight formula units present in a single unit cell [13]. A representation of the Sr3GaAs3 unit cell is depicted in **Fig. 1.1**. The key feature of the AE_3GaAs_3 structure is the formation of $GaAs_4$ tetrahedra by Ga and As atoms (**Fig. 1.1a**). These tetrahedra are connected via two common edges to form isolated $[Ga_2As_6]$ units (**Fig. 1.1b**), which are held together by covalent bonds. The isolation of these polyanions from one another is facilitated by the alkaline-earth AE cations. The $[Ga_2As_6]$ units are oriented along the b-axis and arranged in slabs that are offset by $a/4$. The AE cations serve to separate and balance the charge of the polyanions $[Ga_2As_6]$. Thus, the structure can be understood as valence-precise $[AE^{2+}]_3[Ga^{3+}]\ [As^{3-}]_3$ or, alternatively, as $[AE^{2+}]_6[Ga_2As_6]^{12-}$, i.e., Zintl phases. However, it is essential to note that the Zintl formalism oversimplifies the interactions between cations and anions, and the actual bonding arrangements in these compounds may be considerably more intricate[14].

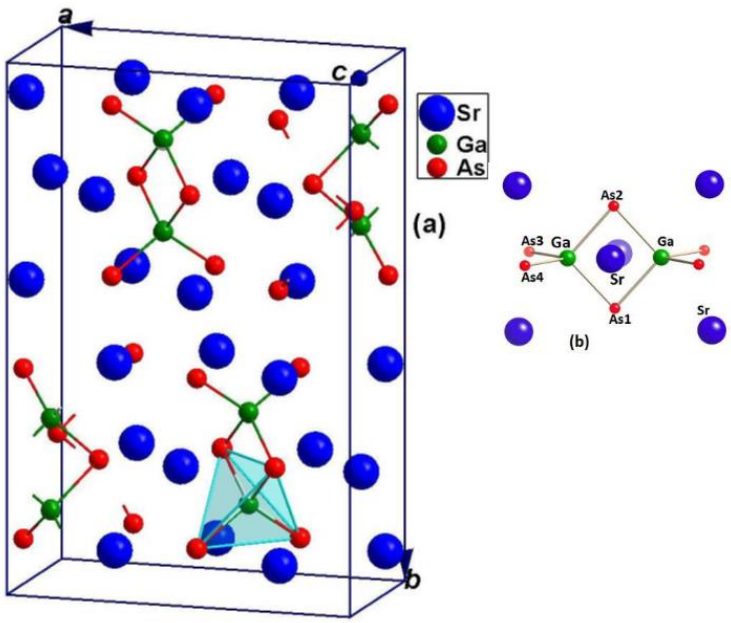

Fig. 1.1: Crystal structure of the Sr_3GaAs_3 unit-cell (a), and the $[Ga_2As_6]$ polyanion (b). Coordination polyhedron around Ga is shown. The purple spheres represent the Sr atoms, the green spheres denote the Ga atoms, and the red ones schematize the arsenic atoms.

The AE_3GaAs_3 compounds (where AE = Sr, Ba) have a unit cell consisting of 56 atoms. Within this unit cell, there exist four non-equivalent positions for AE (AE1, AE2,

AE3, and AE4) and three non-equivalent positions for As (As1, As2, As3, and As4) atoms. The Wyckoff atomic positions for these compounds are as follows: AE1 at 8*d* (x_{AE1}, y_{AE1}, z_{AE1}), AE2 at 8*d* (x_{AE2}, y_{AE2}, z_{AE2}), AE3 at 4c (x_{AE3}, 1/4, z_{AE3}), AE4 at 4c (x_{AE4}, 1/4, z_{AE4}), Ga at 8*d* (x_{Ga}, y_{Ga}, z_{Ga}), As1 at 4*c* (x_{As1}, 1/4, z_{As1}), As2 at 4*c* (x_{As2}, 1/4, z_{As2}), As3 at 8*d* (x_{As3}, y_{As3}, z_{As3}), and As4 at 8*d* (x_{As4}, y_{As4}, z_{As4}). The coordinates x_X, y_X, and z_X refer to the positions internal coordinates of the X atom. Hence, there are a total of 26 free structural parameters, including three lattice parameters (*a*, *b*, and *c*) and 23 internal coordinate parameters, that are not fixed by symmetry. As a result, we need to optimize these parameters by determining their values that correspond to the minimal total energy before exploring other physical properties. To achieve this, we use the experimental crystal structure data [13] as input and determine the equilibrium structural parameters by relaxing the atomic positions and lattice parameters of the unit cell through the minimization of force and stress.

The calculated equilibrium unit-cell and the optimized values of the lattice parameters (a, b and c) and internal atomic coordinates (x, y, z) obtained using the pseudopotential plane-wave (PP-PW) within GGA08 [1]. Where the resulting total energy-volume curve was fitted to the Birch-Murnaghan equation of state [15]. Our results are listed in **Table 1.1** and **1.2** along with the available experimental.

The relative deviation $d(\%) = \left(x_{opt} - x_{exp}\right)100 / x_{exp}$ of the calculated lattice parameters (a, b and c) of Sr_3GaAs_3 (Ba_3GaAs_3) are excellent agreement between the GGA08 optimized lattice parameters values and the corresponding experimental one [13], which are less than -0.4% (-0.3%), -0.5% (-0.4%) and -0.3% (-0.3%) respectively. One can note that the unit-cell parameters a, b and c of A_3GaAs_3 increases when increase of the ionic radii ($R_{Sr} < R_{Ba}$). In addition, relative change of the averaged unit cell deviation (d_r) defined as follows: $d_r = \left(V_{uc}^{(opt)1/3} - V_{uc}^{(\exp)1/3}\right) / V_{uc}^{(\exp)1/3}$ [16], where $V_{uc}^{(opt)}$ and $V_{uc}^{(\exp)}$ are the optimized and experimental unit cell volumes, can be used to give an average measure of the relative deviation of the optimized structure from the experimental counterpart. The very small value of d_r; $d_r = -0.39\%$ for Sr_3GaAs_3 and $d_r = -0.31\%$ for Ba_3GaAs_3, provides a solid proof of the reliability of the theoretical method used for predicting the structural parameters and gives confidence in the reported results on the electronic, optical and elastic properties of the title compounds that will be presented in the following sections. One notes that the unit cell parameters (*a*, *b* and *c*) are related to sizes of the constituent elements. The unit cell volume

(*V*) and lattice parameters (*a*, *b* and *c*) of Ba_3GaAs_3 are larger than those of Sr_3GaAs_3. This is attributed to the fact that the atomic radium of Ba (2.53 Å) is larger than that of Sr (2.19 Å).

Table 1.1: Calculated and experimental equilibrium lattice parameters (*a*, *b* and *c*, in Å) and unit cell volume (*V*, in $Å^3$) for Sr_3GaAs_3 and Ba_3GaAs_3 along with available experimental counterparts [13].

	Sr_3GaAs_3		**Ba_3GaAs_3**	
	Present work [a]	Expt. [b]	Present work [a]	Expt. [b]
a	12.706	12.757	13.3195	13.3589
b	19.175	19.268	19.9121	19.9788
c	6.484	6.503	6.7800	6.8008
V	1579.7	1598.6	1798.2	1815.1

[a] Using PP-PW within GGA08. [b] Ref.[13].

Table 1.2: Calculated equilibrium atomic position fractional coordinates for Sr_3GaAs_3 and Ba_3GaAs_3 along with the available experimental counterparts [13], given in parentheses.

Atom	**x**		**y**		**z**	
	Present work [a]	Exp. [b]	Present work [a]	Exp. [b]	Present work [a]	Exp. [b]
Sr_3GaAs_3						
Sr1	0.01219	0.01274	0.57438	0.57417	0.27619	0.27769
Sr2	0.26371	0.26474	0.07364	0.07335	0.30883	0.30854
Sr3	0.26637	0.26816	1/4	1/4	0.68961	0.68712
Sr4	0.48081	0.48050	1/4	1/4	0.16939	0.16924
Ga	0.12592	0.12642	0.16325	0.16332	0.01492	0.01367
As1	0.23508	0.23468	1/4	1/4	0.21232	0.21000
As2	0.01516	0.01681	1/4	1/4	0.81442	0.81317
As3	0.01010	0.01121	0.08941	0.08982	0.23492	0.23326
As4	0.25832	0.25889	0.58948	0.58990	0.29450	0.29433
Ba_3GaAs_3						
Ba1	0.00992	0.01098	0.57558	0.57530	0.27262	0.27503
Ba2	0.26516	0.26589	0.07493	0.07478	0.31128	0.31222
Ba3	0.26771	0.26836	1/4	1/4	0.68906	0.68616
Ba4	0.48015	0.47937	1/4	1/4	0.16491	0.16338
Ga	0.12770	0.12737	0.16493	0.16495	0.01782	0.01690
As1	0.22964	0.22915	1/4	1/4	0.20966	0.20661
As2	0.02222	0.02242	1/4	1/4	0.82535	0.82548
As3	0.01666	0.01687	0.09081	0.09121	0.22737	0.22609
As4	0.25885	0.26014	0.59197	0.59211	0.30835	0.30814

[a] Using PP-PW within GGA08.
[b] Ref. [13]

Bond lengths provide information about the chemical bond characters. From **Table 1.3**, which lists the bond lengths of some selected bonds, the bond length of the Ga-As bond ranges between 2.4911 and 2.5589 Å, which closely match the sum of the corresponding covalent radii of Ga (1.246 Å) and As (1.210 Å), suggesting that the Ga-As bond is of strong covalent bonding character. The bond length of the Sr-As (Ba-As) bond ranges between 3.1203 and 3.4583 Å (between 3.2682 and 3.5659 Å), which is longer than the sum of the respective covalent radii of Sr (1.85 Å)/Ba (1.96 Å) and As (1.210 Å), suggesting that these bonds are almost ionic in nature. This statement is confirmed by the calculated diagrams of the site projected and *l*-decomposed density of states, which we will discuss later.

Table 1.3: Calculated interatomic distances (in Å) for Sr_3GaAs_3 and Ba_3GaAs_3 compared with the available experimental counterparts [13].

	Sr_3GaAs_3		**Ba_3GaAs_3**			**Sr_3GaAs_3**		**Ba_3GaAs_3**	
	Present	**Exp. [13]**	**Present**	**Exp. [13]**		**Present**	**Exp. [13]**	**Present**	**Exp. [13]**
AE1–As4	3.1428	3.157	3.3405	3.3530	**AE3–As2**	3.2927	3.310	3.3979	3.4195
AE1–As3	3.1521	3.173	3.3285	3.3441	**AE3–As1**	3.4125	3.427	3.5659	3.5780
AE1–As3	3.1957	3.209	3.4219	3.4279	**AE4–As1**	3.1346	3.147	3.3503	3.3556
AE1–As4	3.2708	3.286	3.4045	3.4150	**AE4–As2**	3.1674	3.171	3.3709	3.3740
AE1–As3	3.3387	3.351	3.422	3.4430	**AE4–As3**	3.1632	3.175	3.289	3.2985
AE1–As2	3.436	3.460	3.5619	3.5846	**AE4–As1**	3.3204	3.337	3.4303	3.4519
AE2–As4	3.13	3.148	3.3245	3.3353	**AE4–As2**	3.3754	3.398	3.5012	3.5234
AE2–As3	3.1579	3.172	3.3734	3.3789	**Ga–As4**	2.4914	2.4855	2.5319	2.5281
AE2–As4	3.1761	3.190	3.4022	3.4082	**Ga–As3**	2.4911	2.4911	2.5266	2.5245
AE2–As3	3.2716	3.287	3.3749	3.3937	**Ga–As1**	2.5157	2.515	2.5308	2.5299
AE2–As4	3.3605	3.373	3.4417	3.4631	**Ga–As2**	2.5372	2.538	2.5586	2.5589
AE2–As1	3.4583	3.485	3.5848	3.6071	**AE1–Ga**	3.0897	3.113	3.2254	3.2505
AE3–As1	3.1203	3.132	3.2896	3.3032	**AE2–Ga**	3.1064	3.130	3.2439	3.2715
AE3–As2	3.1612	3.172	3.3914	3.3948	**AE3–Ga**	3.2249	3.251	3.3639	3.3903
AE3–As4	3.1677	3.182	3.2682	3.2839	**AE4–Ga**	3.2181	3.241	3.3704	3.3948

1.2.2 Electronic properties

1.2.2.1 Energy band dispersions

The electronic energy band dispersions, density of states and effective mass are of great importance for technology, electronic band structure is a quite helpful theoretical tool to predict whether a material is conductive, semiconductor or isolator; it transmits, reflects or absorbs the visible spectrum and so on. In other words, according to the band gap type, the band gap character (direct or indirect gap) and dispersion of the electronic states one can for example predict whether a material can be an eventual candidate for thermoelectric applications or optoelectronic applications, including lighting, lasing, optical sensing, displays manufacturing, and sunlight converter and so on. Thus, it is of great importance to study the electronic structure of materials through accurate theoretical methods. The calculated band energy dispersions for our compounds, along the selected high-symmetry points in the first Brillouin zone (red line in **Fig. 1.2**).

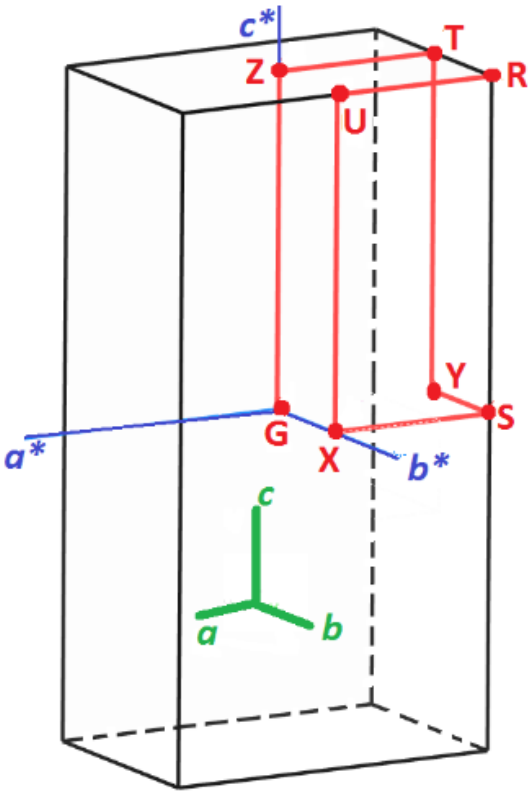

Fig. 1.2: The selected path (red line) in the Brillouin zone for calculating the energy band dispersions for AE_3GaAs_3 (Ae = Sr, Ba). The high-symmetry points have the following coordinates (in units of the reciprocal lattice unit vectors): Γ (0,0,0), Z (0,0,1/2), T (-1/2,0,1/2), Y (-1/2,0,0), S (-1/2,1/2,0), X (0,1/2,0) U (01/2,1/2) and R (-1/2,1/2,1/2).

The calculations carried out for the considered compounds in this work are are investigated with GGA-PBEsol and mBJ functionals within the full potential linearized augmented plane wave (FP-LAPW) method, using mBJ functionals at the optimized structural parameters of both explored systems are depicted in **Fig. 1.3**. As seen in this figure, Sr_3GaAs_3 and Ba_3GaAs_3 are semiconductors, our calculation yielded a direct band gap located at the Γ point. The mBJ (GGA-PBEsol) fundamental bandgap value is equal to 1.271 eV (0.655 eV) for Sr_3GaAs_3 and 1.285 eV (0.572 eV) for Ba_3GaAs_3 between the valence band maximum and the conduction band minimum respectively. There are no experimental values for the gaps of the studied compounds so far up to date to be compared with our findings. Nevertheless, our GGA-PBEsol bandgap for Ba_3GaAs_3 is in acceptable agreement with the unique reported theoretical result; E_g = 0.78 eV, calculated using the tight-binding linear muffin-tin orbital method with the LDA functional (Increasing by 65%). and for mBJ bandgap for Sr_3GaAs_3 there is the unique reported value for this compound; E_g = 1.35 eV, calculated using the pseudopotential projector augmented waves method with the mBJ functional [17].

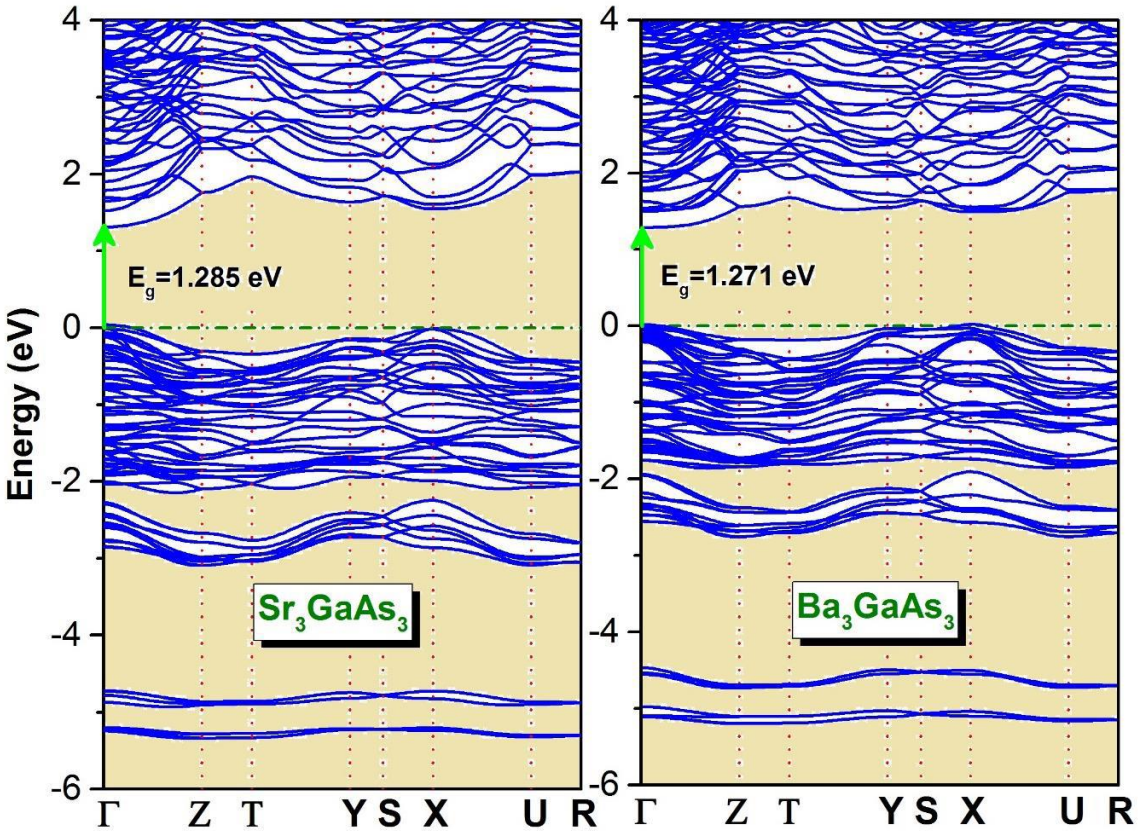

Fig. 1.3: Band structures of AE_3GaAs_3 (*AE* = Sr, Ba) calculated using the TB-mBJ potential. The Fermi level is set to zero.

Our obtained results reveal that:

- The Gallium arsenides of the alkaline metals AE_3GaAs_3 (*AE* = Sr, Ba) compounds have similar electronic structure.
- The valence band maximum (VBM) and the conduction band minimum (CBM) are both located at the Γ point, therefore these compounds are direct band gap (Γ – Γ) semiconductors.
- The energy band gap decreases when moving from Sr_3GaAs_3 to Ba_3GaAs_3, due to the decrease of the ionization potential when moving in the same sequence.
- The TB-mBJ approach improves the band gap values of Sr_3GaAs_3 and Ba_3GaAs_3 by approximately 194% and 225%, respectively, compared to the corresponding GGA08 ones.
- Substituting of Sr by Ba in AE_3GaAs_3 leads to a monotonously narrowing of the mBJ fundamental band gap; it is the reverse case when using the GGA08.

1.2.2.2 Charge-carrier effective mass

Charge-carrier effective masses are very important physical parameters that characterize the electronic energy band dispersions and consequently they link the band structure to the transport parameters, such as charge-carrier mobility and Seebeck coefficient. Thus, it is of great importance to determine the charge-carrier effective masses in solids to have insight into their transport properties. Therefore, it is necessary to estimate the electron and hole effective masses of the studied compounds at the band edge. The hole effective mass m_h^* (electron effective mass m_e^*) was numerically evaluated by fitting the energy band dispersions e (*k*) around the VBM (around the CBM) to parabolas $E(k) = Ak^2$, then the effective masses m^* could be compute using the following expression:

$$\frac{1}{m^*} = \frac{m_0}{\hbar^2}\frac{\partial^2 E(k)}{\partial k^2} \quad (1.1)$$

Table 1.4: Calculated electron and hole effective masses ($m_e^*$and m_h^*, respectively; in unit of electron rest mass) for Sr_3GaAs_3 and Ba_3GaAs_3 compounds at VBM and CBM along the Γ-X , Γ-Y and Γ-Z directions in BZ. correspond to the [010], [100] and [001] crystalline directions, respectively.

	direction	m_e^*	m_h^*
Sr_3GaAs_3	Γ-X	0.45	0.19
	Γ-Y	0.39	1.61
	Γ-Z	2.05	2.24
Ba_3GaAs_3	Γ-X	1.05	0.70
	Γ-Y	0.43	1.73
	Γ-Z	9.98	3.13

The effective mass is m^*, in units of m_0 (m_0 denotes the electron rest mass). The computed effective masses in the Brillouin zone at the Γ point from the band dispersion around the VBM and CBM toward the X, Y and Z directions are listed in **Table 1.4**. According to this table, it shows clearly that the hole effective mass at the valence band maximum is heavier than that of the electron at the conduction band minimum and the hole effective mass along z-axis larger than the corresponding ones along x- and y-axes. So, the calculated band effective masses show a noticeable anisotropy of electronic properties. These results predict the hole mobility should be less than the electron one in the considered compounds, and our calculations show that charge-carrier effective masses of Sr_3GaAs_3 are smaller than that of Ba_3GaAs_3; this expects that the mobility of charge-carriers in Sr_3GaAs_3 is larger than in Ba_3GaAs_3. Hereby, the charge-carrier masses were inversely (directly) proportional with the electrical conductivity (the Seebeck coefficient) respectively. Consequently, the *n*-type Sr_3GaAs_3 and Ba_3GaAs_3 compounds would have the largest electrical conductivity, while the *p*-type Sr_3GaAs_3 and Ba_3GaAs_3 compounds would have the highest the Seebeck coefficient.

The hole and electron effective masses in an arbitrary direction infinitesimally close to the Γ-point for an orthorhombic system can be obtained through the following relationship [18]:

$$m^* = \frac{1}{\cos^2(\alpha)/m^*_{[100]} + \cos^2(\beta)/m^*_{[010]} + \cos^2(\gamma)/m^*_{[001]}} \quad (1.2)$$

where α, β, and γ are the angles between that specific direction and the [100], [010] and [001] crystalline directions, respectively. **Fig. 1.4** and **1.5** illustrate 3D-representations of the crystalline direction dependence of holes and electrons effective masses at Γ-point and their cross-sections (2D-representations) in the (100), (010) and (001) crystalline planes. From these figures, it is obvious that the charge carrier effective masses in the title compounds are strongly anisotropic. Thus, transport parameters, such as mobility and Seebeck coefficient, are expected to be strongly anisotropic too. One notes that the effective mass of electrons in Ba_3GaAs_3 shows the strongest anisotropy due to its unusual heavy holes mass in the [001] crystalline direction.

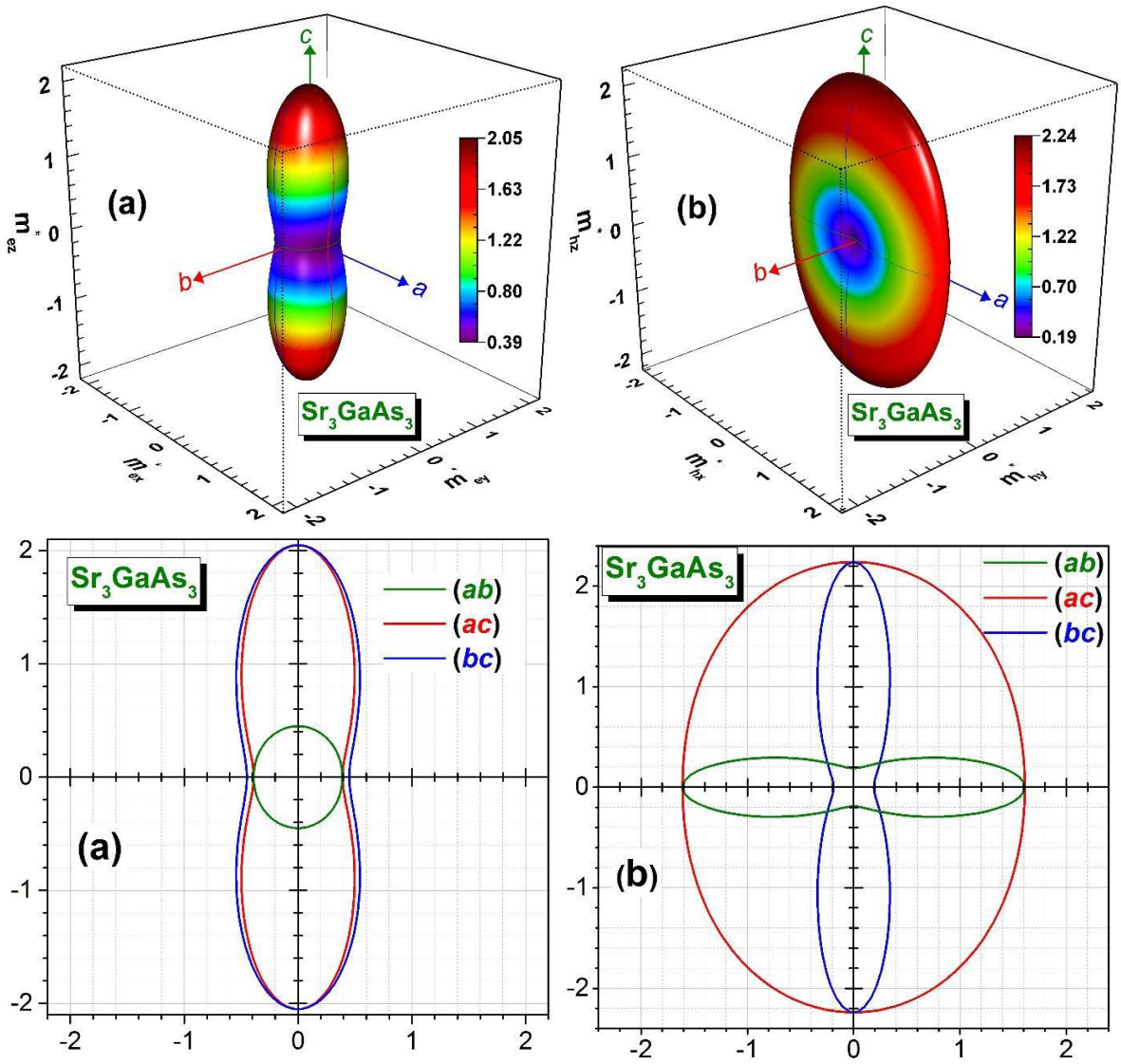

Fig. 1.4: 3D-representations of the crystal direction dependent effective masses of electrons **(a)** and holes **(b)** at Γ-point and their cross-sections in the (001); (*ab*), (010); (*ac*) and (100); (*bc*) crystalline planes for Sr_3GaAs_3.

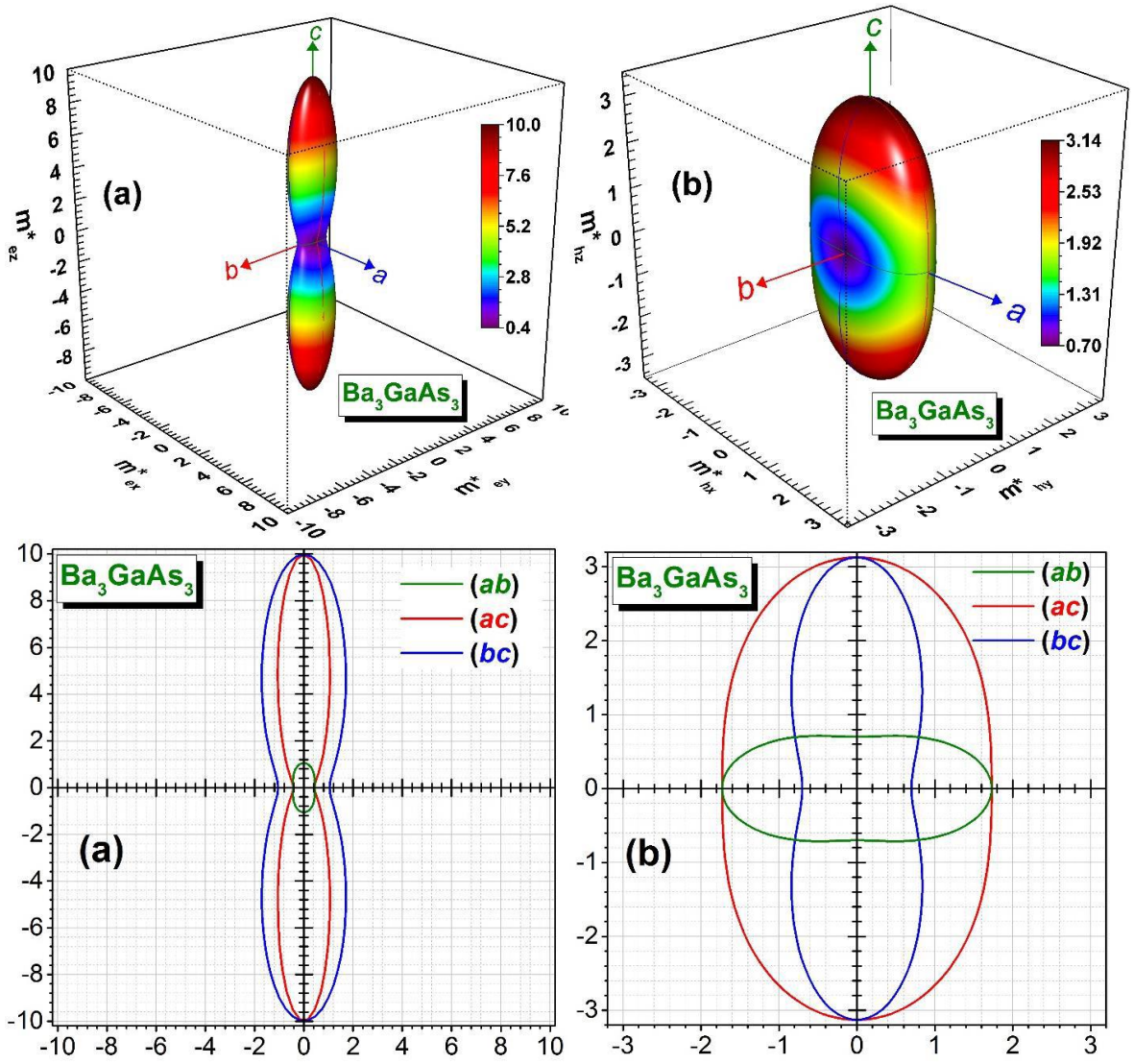

Fig. 1.5: 3D-representations of the crystal direction dependent effective masses of electrons **(a)** and holes **(b)** at Γ-point and their cross-sections in the (001); (*ab*), (010); (*ac*) and (100); (*bc*) crystalline planes for Ba_3GaAs_3.

1.2.2.3 Density of states

The computed total density of states (TDOS) and the atomic-resolved *l*-projected density of states (PDOS) diagrams guide us to closely investigate the electronic structure and gain insight into the nature of chemical bonds between constituents of the studied compounds employing the mBJ potential. **Fig. 1.6** illustrates both curves (i.e., TDOS and PDOS) for the title compounds (Sr_3GaAs_3 and Ba_3GaAs_3) between -12 eV and 5 eV for our compounds Sr_3GaAs_3 (Ba_3GaAs_3). The valence band of Sr_3GaAs_3 consists of six sub-bands labeled V1, V2, V3, V4, V5 and V6, (the valence band of Ba_3GaAs_3 is subdivided into seven sub-bands labelled V1, V2, V3, V4, V5, V6 and V7; the V7 sub-band is not shown for clarity of the figure).

Firstly, V1 in energy range between from -2.2 eV (-2.0 eV) to 0 eV, mainly consists of the As-4*p* states with a noticeable contribution from the Ga-4*p* states and a small contribution from the *AE*-n*d* (n = 3 for Sr and n = 4 for Ba) states. One notes the presence of a weak mixing between the As-4*p* and *AE*-n*d* states and between the Ga-4*p* and *AE*-n*d* states, which is an indicative of the presence of a weak degree of covalency in the As–*AE* and Ga–*AE* bonds. For V2 valence band group, there is an overlapping between two mainly orbitals, the As-4*p* and Ga-4*p* states, suggesting that the As-Ga chemical bond is the covalent nature. The sub-bands V3 and V4 energy range are start from ~-5.57 eV (~-5.40 eV) to -4.59 eV (~-4.35 eV), consist of the hybridized Ga-4*s* and As-4*p* orbitals. The sub-band V5, ranging between ~-9.92 eV and ~-880 eV (~-9.49 eV and ~-8.37 eV), is composed mainly of the hybridizing between the As-4*s* states and the Ga-4*sp* states. The V6 valence band, forming a narrow peak centered at -10.68 eV (~-10.13 eV), consists of the hybridized As-4*s* and Ga-4*s* states. The valence subband V7; not shown in **Fig. 1.6**, located between ~-13.48 eV and ~-12.51 eV, which appears only in Ba_3GaAs_3 is originated from the Ba-5*p* states.

The main feature in **Fig. 1.6** is the strong hybridization (overlapping) between the As and Ga states in all the valence band region, indicating the high covalency of the As-Ga chemical bond. This conclusion is consistent with that deduced from the As-Ga bond length discussed in the structural properties section. On the other hand, apart the weak overlapping in the V1, the PDOS distribution of the *AE* (Sr/Ba) atom is energetically separated from those of the Ga and As atoms, indicating that the chemical bonding between *AE* and Ga/As is predominantly of ionic character. The conduction sub-band C1, ranging from the CBM up to 8 eV, consists mainly of the *AE*-n*d* (Sr/Ba) states. Hence, the Sr/Ba-n*d* electrons would play

an important role in the electrical conductivity for the title compounds. It is worth noting that despite the fact that the As/*AE* atoms have four inequivalent crystallographic positions, the general profiles of their respective PDOS are very similar to each other but with somewhat different amplitudes as shown in **Fig. 1. 6**, suggesting that they would have the same bonding character with neigh boring atoms.

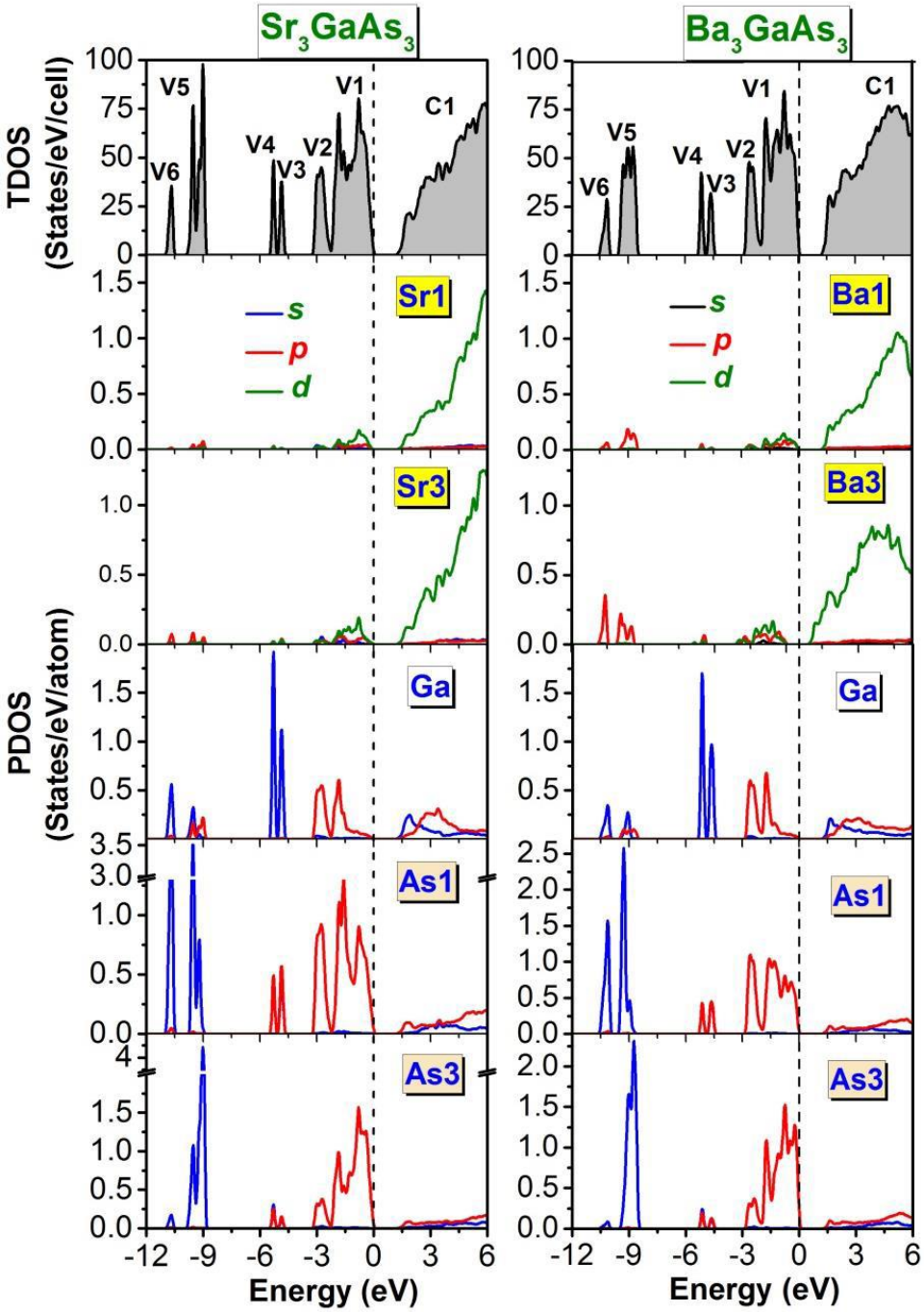

Fig. 1.6: The calculated TDOS, its projections on orbitals and PDOS for Sr_3GaAs_3 (left panel) and Ba_3GaAs_3 (right panel) using the mBJ potential. The Fermi level is at zero.

1.2.3 Elastic properties

The elastic moduli of solids, both monocrystalline and polycrystalline, serve to measure how these materials react to external deformations within the elastic range. Consequently, these moduli are intricately connected to a multitude of fundamental characteristics of solids, the mechanical properties, structural stability, sound velocity, bonding forces between neighbouring atoms, nature and strength of chemical bond, machinability, anisotropy and lattice dynamics, ... Hence, the assessment of solid materials' elastic moduli is of profound significance from both foundational and practical standpoints.

1.2.3.1 Monocrystalline elastic constants

The calculated elastic constant in single-crystal at orthorhombic phase were described by twenty-one independent elastic constants C_{ij}s (and their elastic compliances S_{ij}s), with considerable values of nine independent elastic constants, labeled C_{11}, C_{12}, C_{13}, C_{22}, C_{23}, C_{33}, C_{44}, C_{55} and C_{66}. Our calculated elastic constants C_{ij} of considered compounds are presented in **Table 1.5**. Show both theme's values. Until now no experimental or theoretical data interest to study the elastic constants of the title compounds. According to **Table 1.5**. One can make the following conclusions:

i. The C_{11}, C_{22} and C_{33} elastic constants illustrate the stiffness stress lengthways the crystallographic a, b and c axes, respectively. For both studied compounds, the $C_{11} > C_{22} > C_{33}$. Sr_3GaAs_3 and Ba_3GaAs_3 compounds appear large resistant to versus the external stress along the [100] crystallographic direction comparing that along the other directions ([010] and [001]). This indicates that values of the C_{ij}s do not change significantly with the radius of the alkali-earth atom in the title compounds.

ii. As can be again attributed to the more robust bonds that along the crystallographic a-axis. the shear modulus of the (100), (010) and (001) planes represented by the C_{44}, C_{55} and C_{66} elastic constants, respectively. Also, suggest that the linear compressibility (β) along the [100] direction is smaller than that along the [010] direction which in turn is a little smaller than that along the [001] direction; $\beta^{[100]} < \beta^{[010]} < \beta^{[001]}$.

Table 1.5: Calculated elastic constant C_{ij} (in GPa) for the orthorhombic Zintl phase Sr_3GaAs_3 and Ba_3GaAs_3 compounds.

	C_{11}	C_{12}	C_{13}	C_{22}	C_{23}	C_{33}	C_{44}	C_{55}	C_{66}
Sr_3GaAs_3	93.3	22.1	27.2	82.8	26.9	81.5	28.8	28.4	26.5
Ba_3GaAs_3	84.4	16.8	22.4	79.7	22.9	76.4	20.5	23.4	20.6

The letters are comparatively little than the C_{11}, C_{22} and C_{33}, demonstrating that these compounds are less resistance to shear deformation than compression. On the other hand, C_{44}, C_{55} and C_{66} values are almost equal, so one can draw a conclusion that the shear modulus of the title compounds is almost isotropic.

iii. The computed elastic constants of the studied compounds satisfy the conditions of Born and Huang mechanical stability criteria [19,20]:

$C_{11}>0$, $C_{22}>0$, $C_{33}>0$, $C_{44}>0$, $C_{55}>0$, $C_{66}>0$, $C_{11}+C_{22}-2C_{12}>0$, $C_{11}+C_{33}-2C_{13}>0$, $C_{22}+C_{33}-2C_{23}>0$, $C_{11}+C_{22}+C_{33}+2(C_{12}+C_{13}+C_{23}+)>0$

This suggests the mechanical stability of Sr_3GaAs_3 and Ba_3GaAs_3 compounds.

iv. There are some important physical properties of the material (such as thermal conductivity) related sound velocity in a crystal. For given the single-crystal elastic wave velocities in different directions ([100], [001] and [110]) can be use Christoffel equation [21] and procedure of Brugger [22] in an orthorhombic system, the pure longitudinal (L) and transverse (T) wave velocities propagating are given by the following expressions [23]:

$$\begin{aligned} v_L^{[100]} &= \sqrt{C_{11}/\rho}, v_{T_1}^{[100]} = \sqrt{C_{66}/\rho}, v_{T_2}^{[100]} = \sqrt{C_{55}/\rho} \\ v_L^{[010]} &= \sqrt{C_{22}/\rho}, v_{T_1}^{[010]} = \sqrt{C_{66}/\rho}, v_{T_2}^{[010]} = \sqrt{C_{44}/\rho} \\ v_L^{[001]} &= \sqrt{C_{33}/\rho}, v_{T_1}^{[001]} = \sqrt{C_{55}/\rho}, v_{T_2}^{[001]} = \sqrt{C_{44}/\rho} \end{aligned} \qquad (1.3)$$

Where ρ : is the mass density of the propagating medium. The calculated elastic wave velocities along [100], [001] and [110] directions are listed in **Table 1.6**. From this latter, one can see that the transverse wave velocities are less than the longitudinal ones, where its values less than *4500 m/s*, and both the longitudinal and transverse waves increase when substitution *Ba* by *Sr* atoms.

Table 1.6: Longitudinal and transverse acoustic wave velocities (v_L and v_T, in *m/s*) in different crystallography directions for considered compounds.

	$v_L^{[100]}$	$v_L^{[010]}$	$v_L^{[001]}$	$v_{T_1}^{[100]}$	$v_{T_1}^{[010]}$	$v_{T_1}^{[001]}$	$v_{T_2}^{[100]}$	$v_{T_2}^{[010]}$	$v_{T_2}^{[001]}$
Sr_3GaAs_3	4461.6	4203.1	4170.0	2377.8	2377.8	2461.6	2461.6	2478.8	2478.8
Ba_3GaAs_3	4021.3	3907.7	3826.0	1986.7	1986.7	2117.4	2117.4	1981.9	1981.9

1.2.3.2 Elastic anisotropy

The extent of elastic anisotropy is widely recognized for its significant role in materials, engineering, and physical crystallography. It influences material stability, dislocations, and reveals diverse bonding characteristics in various crystallographic directions. Understanding elastic anisotropy is crucial for insights into microcracks in solids [24] and its effect at the nanoscale precursor textures in alloys [25]. So, there are several criterion to investigate the elastic anisotropy for example: universal index[26], shear anisotropic factors [27], the percentage anisotropy in compressibility and shear [28], The scalar log-Euclidean anisotropy index [29] and 3D representation of elastic moduli. In this presentation, we introduce two distinct approaches for evaluating elastic anisotropy.

First, universal index A^U has been proposed by Ranganathan and Ostoja-Starzewski [26], which is defined as follows:

$$A^U = 5\frac{G_V}{G_R} + \frac{B_V}{B_R} - 6 \qquad (1.4)$$

where B and G represent the bulk and shear modulus and the subscripts V and R denote Voigt and Reuss approximations, respectively. The isotropic crystals are characterized by universal index equal to zero (A^U= 0), so, any deviation from this value means that the extent of anisotropy crystals and can be measuring its degree. Calculated value of A^U for Sr_3GaAs_3 and Ba_3GaAs_3 compounds is equal to 0.037 and 0.158 respectively, denoting that Sr_3GaAs_3 is characterized by a feeble elastic anisotropy, whereas Ba_3GaAs_3 is characterized by a noticeable elastic anisotropy, so its degree increases when substitution *Strontium* by *Barium* atoms in AE_3GaAs_3 system.

Second, the evaluation of the elastic anisotropy in a material is by representation 3D of the crystallographic directions dependence of its elastic moduli (Young's modulus and bulk's modulus), In a 3D plotting, the exhibition a spherical shape means an isotropic system, and the aberration from a spherical shape denotes the degree of anisotropy. Representation of the 3D-closed surface for the crystallographic direction dependence of the Young's modulus E and compressibility β of an orthorhombic crystal are expressed by the following well-known relations [30]

$$\frac{1}{E} = l_1^4 S_{11} + 2l_1^2 l_2^2 S_{12} + 2l_1^2 l_3^2 S_{13} + l_2^4 S_{22} + 2l_2^2 l_3^2 S_{23} + l_3^4 S_{33} + l_2^2 l_3^2 S_{44} + l_1^2 l_3^2 S_{55} + l_1^2 l_2^2 S_{66} \qquad (1.5)$$

$$\beta = \frac{1}{B} = \left(S_{11} + S_{12} + S_{13}\right) l_1^2 + \left(S_{12} + S_{22} + S_{23}\right) l_2^2 + \left(S_{33} + S_{23} + S_{13}\right) l_3^2 \qquad (1.6)$$

Where, l_1, l_2 and l_3 are the direction cosines coordinates with respect to X, Y and Z axes respectively, which show the angles between these axes, and S_{ij}s are the elastic compliances constants. Computed 3D-closed surface and their central cross sections in the YZ, XZ and XY planes of the Young's modulus and bulk's modulus for both considered compounds are shown in **Fig. 1.7** and **Fig. 1.8**. From these illustration 3D and its central cross sections for the two considered compounds of young's modulus E, one can see that deviate largely from the spherical shape and circular form respectively, demonstrating a noticeable directional dependence, while from bulk's modulus, evidencing that these compounds are characterized by a feeble elastic anisotropy and we show that the values of young's modulus and bulk's modulus along the X, Y and Z axes for Ba_3GaAs_3 are less than Sr_3GaAs_3 values.

Fig. 1.7 shows that the 3D-representations (2D-representations) of the Young's modulus deviate considerably from the spherical shape (circular form), suggesting that this property is noticeably anisotropic. The minimum value of *E* is equal to 67 (54) GPa along the [100] direction and the maximum value is equal to 82 (77) GPa along the [001] direction in Sr_3GaAs_3 (Ba_3GaAs_3)

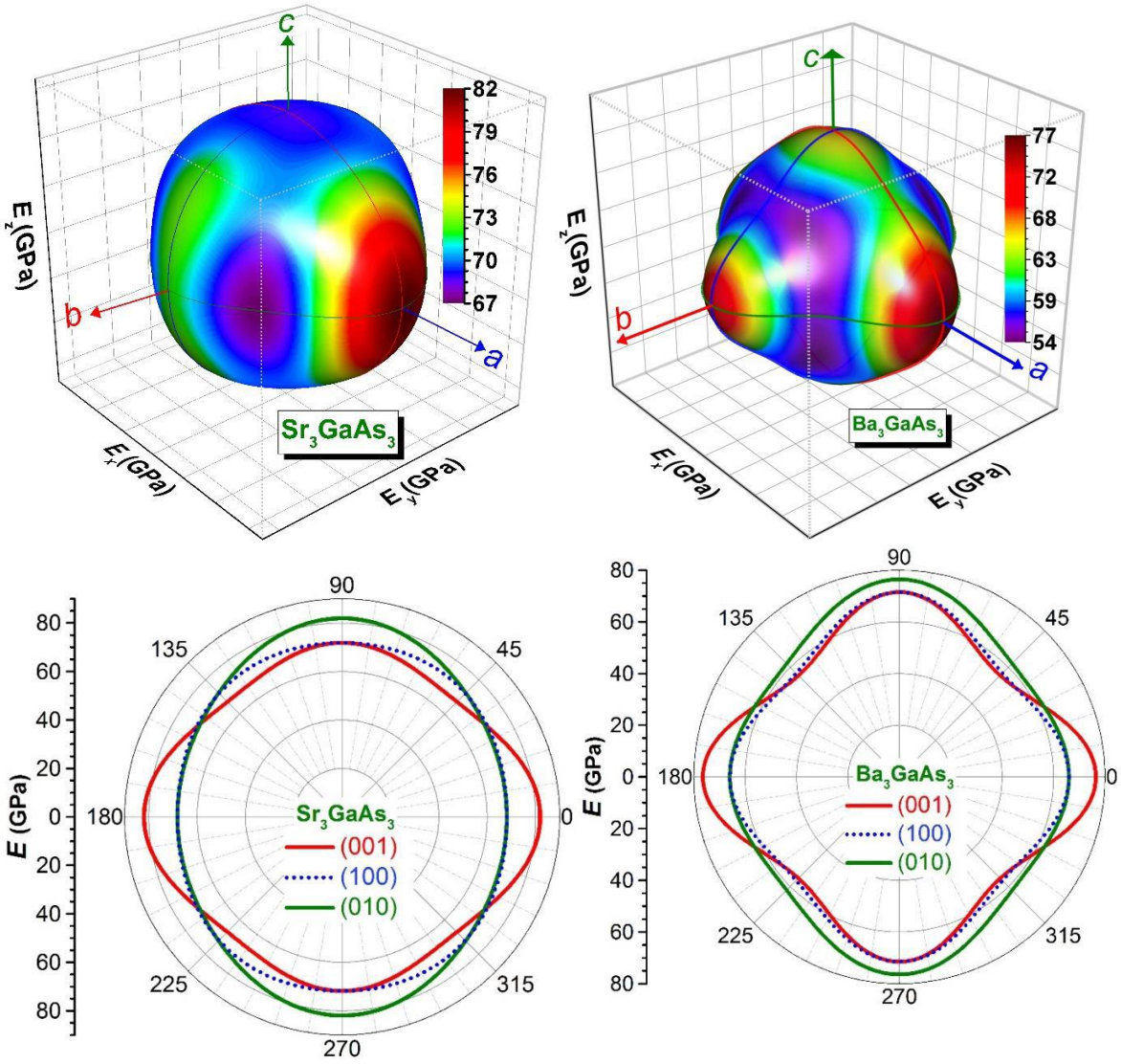

Fig. 1.7: 3D-representations of crystal direction dependence of the Young's modulus and their cross-sections in the (001), (010) and 001) crystalline planes for Sr_3GaAs_3 and Ba_3GaAs_3

Fig. 1.8 shows that the deviation degree of the 3D-representations (2Drepresenations) of compressibility from the spherical shape (circle form) is less than that of the Young's modulus, suggesting that this property is less anisotropic than the Young's modulus. The minimum value of β is equal to 0.0067 (0.008) GPa^{-1} along the [100] direction and the maximum value is equal to 0.0079 (0.0085) GPa^{-1} along the [001] in Sr_3GaAs_3 (Ba_3GaAs_3). This is consistent with the statement that has been already drawn from the elastic constants C_{11}, C_{22} and C_{33}; β exhibits a relatively weak anisotropy. Note that Ba_3GaAs_3 is somewhat

more elastically anisotropic than Sr_3GaAs_3, which is consistent with the statement that has been deduced from the universal anisotropy index A^U, vide supra.

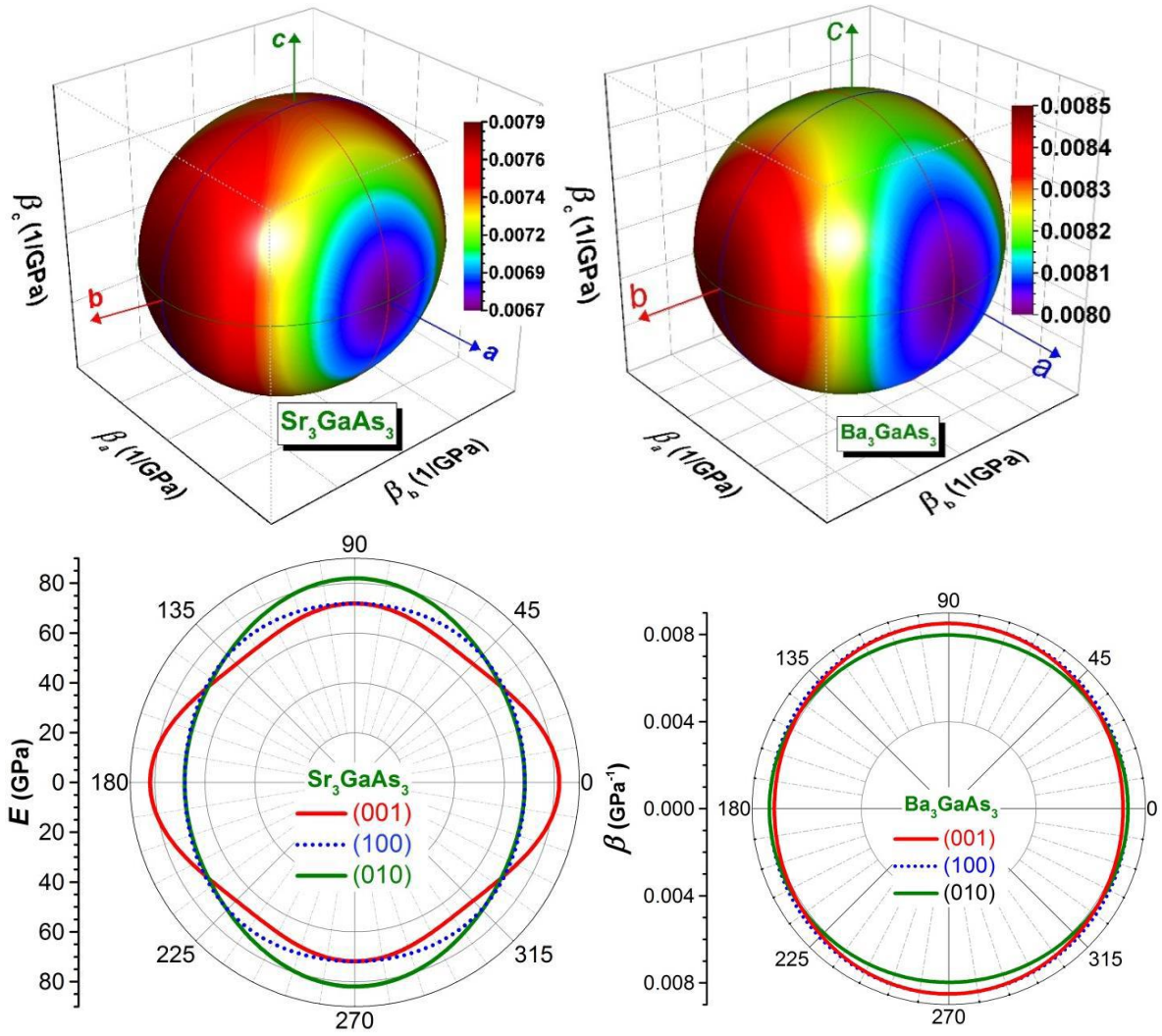

Fig. 1.8: 3D-representations of the crystal direction dependence of the linear compressibility and their cross-sections in the (001), (010) and 001) crystalline planes for Sr_3GaAs_3 and Ba_3GaAs_3.

1.2.3.3 Polycrystalline elastic moduli

In a polycrystalline system, numerous grains possess distinct structures that can influence the relative elastic properties. Consequently, we must consider hypotheses such as the isostress of Voigt [31], isostrain Reuss [32] and Hill approximations [33], which bulk 's modulus B and shear's modulus G in recent approximations defined by following express:

$$\frac{1}{B_R} = \left(S_{11} + S_{22} + S_{33}\right) + 2\left(S_{12} + S_{13} + S_{23}\right) \qquad (1.7)$$

$$\frac{1}{G_R} = \frac{4\left(S_{11}+S_{22}+S_{33}\right)-4\left(S_{12}+S_{13}+S_{23}\right)+3\left(S_{44}+S_{55}+S_{66}\right)}{15} \quad (1.8)$$

$$B_V = \frac{1}{9}\left(C_{11}+C_{22}+C_{33}+2\left[C_{12}+C_{13}+C_{23}\right]\right) \quad (1.9)$$

$$G_V = \frac{1}{15}\left(C_{11}+C_{22}+C_{33}+3\left[C_{44}+C_{55}+C_{66}\right]-\left[C_{12}+C_{13}+C_{23}\right]\right) \quad (1.10)$$

Here: S_{ij} (C_{ij}) is the elastic compliances (stiffness) constants, where $S_{ij} = 1/C_{ij}$

Hill proved that the effective values is equal to the arithmetic mean between bulk and shear moduli:

$$B_H = \frac{B_R + B_V}{2} \quad (1.11) \quad \text{and} \quad G_H = \frac{G_R + G_V}{2} \quad (1.12)$$

Young's modulus (E), Poisson ratio's σ [34], average longitudinal v_l, transverse v_T elastic wave velocities, the average wave velocity v_m [35] and Debye temperature T_D [36] in polycrystalline structure can be computed from the following expressions:

$$E = \frac{9BG}{3B+G} \quad (1.13) \quad \text{and} \quad \sigma = \frac{3B-2G}{2\left(3B+G\right)} \quad (1.14)$$

$$v_l = \left[\frac{3B_H + 4G_H}{3\rho}\right]^{1/2} \quad (1.15) \quad \text{and} \quad v_T = \left[\frac{G_H}{\rho}\right]^{1/2} \quad (1.16)$$

$$v_m = \left[\frac{1}{3}\left(\frac{1}{v_l^3}+\frac{2}{v_T^3}\right)\right]^{-1/3} \quad (1.17) \quad \text{and} \quad T_D = \frac{h}{K_B}\left[\frac{3n}{4\pi}\frac{N_A\rho}{M}\right]^{1/3} v_m \quad (1.18)$$

Where: ρ is the mass density, n is the number of atoms in the molecule, N_A is Avogadro number, M is the molecular weight, h and K_B are Planck and Boltzmann constants respectively. Employing the aforementioned relations, the obtained results are listed in **Table 1.7**, which let us to make some conclusions:

a) There is well-known relationship between the elastic moduli (bulk and shear) and the elastic properties of polycrystalline pure metals, Pugh's ratio empirical criterion [37], which provide information concerning the brittle-ductile nature of a material, if B/G >1.75 denotes the ductile nature of the material; otherwise, it is brittle. The computed B/G ratio values registered in **Table 1.6**, these results indicating the brittle nature of the considered compounds. Brittle materials are fragile to thermal shocks [38].

Table 1.7: Calculated Reuss, Voigt and Hill bulk (B, in GPa), shear's modulus (G, in GPa), Young's modulus (E, in GPa) and Poisson's ratio (σ, dimensionless), Pugh ratio B_H/G_H, average sound velocities (v_m, in m/s), Debye temperature (T_D, in K) and density (ρ) for polycrystalline Sr_3GaAs_3 and Ba_3GaAs_3 compounds. The subscript V, R and H stand to the Voigt, Reuss and Hill.

	Theory	**B**	**G**	**E**	**σ**	**B/G**	v_m	ρ	**T_D**
	V	45.55	28.84	71.45	0.239				
Sr_3GaAs_3	***R***	45.45	28.65	71.02	0.240				
	H	45.50	28.75	71.24	0.239	1.58	2747	4.687	268.4
	V	40.53	24.78	61.75	0.246				
Ba_3GaAs_3	***R***	40.51	24.02	60.17	0.252				
	H	40.52	24.40	60.96	0.249	1.66	2395	5.219	224.2

b) Values of *B*, *G* and *E* of Sr_3GaAs_3 are somewhat greater than those of Ba_3GaAs_3.This is expected as the unit-cell volume of Ba_3GaAs_3 is somewhat greater than that of Sr_3GaAs_3; the bulk modulus value is inversely proportional to the unit-cell volume, and the C_{ij} values of Ba_3GaAs_3 are somewhat smaller than those of Sr_3GaAs_3.

c) Debye temperature T_D is correlated with several important physical properties of solids, such as heat capacity value, thermal expansion, melting temperature, so on. As a rule, when T_D increase, thermal conductivity and melting temperature increase [38], as well as, it can be used to separate between high- and low-temperature regions for a solid. Debye temperature T_D was calculated by relationship mentioned above [36]. The values of T_D dependences Sr_3GaAs_3 and Ba_3GaAs_3 are listed in **Table 1.6**. On the hand, T_D and V_m of Sr_3GaAs_3 are somewhat larger than those of Ba_3GaAs_3, which is expect as the elastic moduli of the former are somewhat larger than those of the later.

d) The determination of chemical bonding nature can be by the use of Poisson's ratio σ and comparison between shear G and bulk B moduli, in order for chemical bonding to be covalent, G must be small comparing, A typical value of σ for covalent bonding is less than 0.2; for ionic bonding σ is typically 0.3-0.4; finally for pure-ionic limit bonding σ is 0.5 and G is zero [39]. One shows that the values of the studied compounds are equal almost 0.25. So, we suggest that the chemical bonding in Sr_3GaAs_3 and Ba_3GaAs_3 compounds has a dominant covalent character.

1.2.4 Optical properties

The Sr_3GaAs_3 and Ba_3GaAs_3 compounds have an orthorhombic structure. Thus, the consequent dielectric functions are $\varepsilon^{xx}(\omega)$, $\varepsilon^{yy}(\omega)$ and $\varepsilon^{zz}(\omega)$. These latter correspond to incident radiation in an electrical field polarized parallel along three axes dependents (x, y and z) respectively. The optical properties may be concluded from the imaginary part $\varepsilon_2(\omega)$ and the real part $\varepsilon_1(\omega)$ of the complex dielectric function $\varepsilon(\omega) = \varepsilon_1(\omega) + i\,\varepsilon_2(\omega)$. The linear optical response of the medium is characterized by the dielectric function $\varepsilon(\omega)$. The intraband and interband transitions are contributions to $\varepsilon(\omega)$, but the first is important for metals, where $\varepsilon_2(\omega)$ explains the absorbed energy, and it is computed from the matrix elements dependent valence band and the conduction band using well-known relationship[40,41], while the real part $\varepsilon_1(\omega)$ describe the incident radiation, it can be calculated from $\varepsilon_2(\omega)$ within the Kramers–Kronig transformation [42].

The computed components of the imaginary and real parts of the dielectric tensor for the studied compounds are display in **Fig. 1.9** in a wide range of energy, 0-14 eV. We see the spectra of components (ε^{xx}, ε^{yy} and ε^{zz}) of the imaginary and real parts exhibit main peaks with almost the same position for title compounds and it appear a considerable anisotropy. There are four main peaks in imaginary part of incident radiation along three crystallography directions for Sr_3GaAs_3 and Ba_3GaAs_3 compounds listed in **Table 1.8**. One can conclude that the fundamental originated of the peaks E_1, E_2, E_3 and E_4 of the Sr_3GaAs_3 (Ba_3GaAs_3) $\varepsilon_2(\omega)$ spectrum due based on the PDOS diagrams given in **Fig. 1.6**, one can assign the observed structure in $\varepsilon_2(\omega)$ spectrum to electronic transitions from the V_1, V_2, V_3 and V_4 valence sub-bands to the C_1 conduction sub-band, i.e., transitions from the filled As-4*p* and Ga-4*p* states to the empty Sr/Ba-n*d* states (n = 3 for Sr and n = 4 for Ba). From **Fig. 1.9**, one observes that the energy locations and magnitudes of the major peaks in the $\varepsilon_2(\omega)$ spectra are clearly different in the energy range from 1.5 eV to 7.5 eV. In other words, $\varepsilon_2(\omega)$ curves are distinct from each other in the energy range 1.5-7.5 eV and are almost superposed in the rest of the considered energy range. The magnitude of the structure corresponding to ***E*||*b*** is somewhat larger than those corresponding to ***E*||*a*** and ***E*||*c*.** These features indicate that the imaginary part of the dielectric function; $\varepsilon_2(\omega)$, exhibits a well pronounced anisotropy in the energy range ~1.5 to ~7.5 eV and it is almost isotropic in the rest of the considered energy range for both studied compounds.

Table 1.8: Determined the main peak positions of the dependent components (ε^{xx}, ε^{yy} and ε^{zz}) of the imaginary part for Sr_3GaAs_3 and Ba_3GaAs_3 compounds.

Directions	**xx**				**yy**				**zz**			
Peak positions	**E_1**	**E_2**	**E_3**	**E_4**	**E_1**	**E_2**	**E_3**	**E_4**	**E_1**	**E_2**	**E_3**	**E_4**
Sr_3GaAs_3	3.33	3.99	4.34	4.88	3.42	3.96	4.29	5.67	3.58	4.23	4.48	5.16
Ba_3GaAs_3	2.82	3.88	4.15	4.72	2.73	3.45	3.96	4.29	2.90	3.58	4.15	4.75

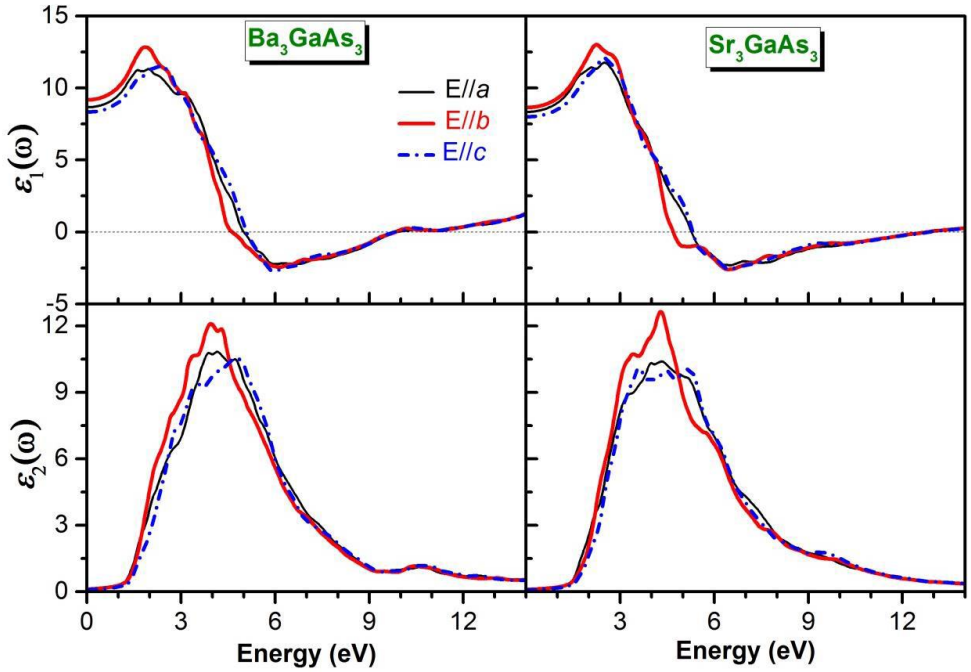

Fig. 1.9: Real (upper panel) and imaginary (lower panel) parts of the dielectric function for Sr_3GaAs_3 and Ba_3GaAs_3 compounds of the incident radiations polarized along x-, y- and z-axes directions, using the TB-mBJ potential.

The real part of dielectric function is considered importance parameter, because there are many features of materials science dependence by the static dielectric constant $\varepsilon_1(0)$, this latter is the real parts at low energy limit. According to Penn model[43]:

$$\varepsilon_1(0) = 1 + \left(\hbar\omega_p / E_g\right)^2 \left[1 - \left(E_g / 4E_F\right) + \left(E_g / 4E_F\right)^2 / 3\right] \quad (1.19)$$

Where $\hbar\omega_p$ is the plasma energy and neglecting the small quantity E_g / E_F, the values of static dielectric constants for Ba_3GaAs_3 along the three directions (x-, y- and z-axes) are

represented in **Table 1.8**. We note that the values of static dielectric constants for Ba_3GaAs_3 are greater than that of Sr_3GaAs_3 and there is inversely proportional relationship between the band gap *Eg* and $\varepsilon_1(0)$. Also, one observes that $\varepsilon_2(\omega)$ exhibits obvious anisotropy in the energy window from 0 eV to ~7.5 eV for both studied compounds. Each $\varepsilon_1(\omega)$ (x, y and z) curve increase with the increasing photon energy from its static value to reach a maximum then starts to decrease. Magnitude of $\varepsilon_1(\omega)$ (x, y and z) curve, corresponding to the ***E*||*b*** polarization, is somewhat greater than those of $\varepsilon_1(\omega)_{xx}$ and $\varepsilon_1(\omega)_{zz}$. The maximum magnitude of $\varepsilon_1(\omega)$ corresponding to ***E*||*b*** polarization is ~12.83 at ~1.84 eV for Sr_3GaAs_3 and ~13.00 at ~2.22 eV for Ba_3GaAs_3. $_1\varepsilon(\omega)$ has negative values in the energy range from ~4.62 eV to ~9.81 eV for Sr_3GaAs_3 and from ~4.68 eV to ~12.84 eV for Ba_3GaAs_3, which correspond to metallic behavior. The calculated values of the electronic static dielectric constant for the three polarizations; $\varepsilon_1(0)_{xx}$, $\varepsilon_1(0)_{yy}$ and $\varepsilon_1(0)_{zz}$ for the studied compounds are summarized in **Table 1.9**. The $\delta\varepsilon$, given by following relation [16], [44]: $\delta\varepsilon = (\varepsilon^{zz}(0) - \varepsilon^{xx}(0)) / \varepsilon^{tot}(0)$, can be used as a measure of optical anisotropy. The calculated $\delta\varepsilon$ is equal to 0.042 for Sr_3GaAs_3 and 0.013 for Ba_3GaAs_3, implying a relatively low anisotropy degree.

Table 1.9: Calculated static anisotropy A_{OPT} based on the static refractive index $n(0)$ and the static dielectric constants $\varepsilon_1(0)$ for Sr_3GaAs_3 and Ba_3GaAs_3 compounds along x-, y-, z-axes.

	Direction	$n(0)$	$\varepsilon_1(0)$	A_{OPT}
Sr_3GaAs_3	**xx**	2.89	8.330	1.00
	yy	2.94	8.636	1.06
	zz	2.83	7.983	0.94
Ba_3GaAs_3	**xx**	2.94	8.655	0.99
	yy	3.03	9.168	1.08
	zz	2.88	8.320	0.93

Using $\varepsilon_1(\omega)$ and $\varepsilon_2(\omega)$ well-known relationships could be calculate the absorption coefficient $\alpha(\omega)$, electron energy-loss function $L(\omega)$, reflectivity $R(\omega)$, refraction index $n(\omega)$ and extinction coefficient $k(\omega)$, these parameters are display in **Fig. 1.10**. We can conclude the following:

a) The absorption spectrum is extends horizontally forward starting from 1.3 eV up to 30 eV, this is start corresponding to the energy direct gap at Γ point. In the semiconductors, typically when the photon energy is increases the absorption coefficient α(ω) rises rapidly as is the case with our system. These compounds have a band gap about 1.3 eV may absorb the infrared rays of the invisible field and there is the strong absorption of the electromagnetic wave occurs in the Near-UV region. The high absorptivity of the electromagnetic wave in the visible spectrum and Near-UV region, suggests that these compounds are possible candidates for optoelectronic applications based on absorption of electromagnetic radiation in the aforementioned energy ranges. We can see that Sr_3GaAs_3 (Ba_3GaAs_3) is characterized by a high optical absorption ($>10^6$ cm^{-1}) in two wide optical structures centered almost at 9 eV (8 eV) and 23 eV (18 eV) respectively.

b) The reflectivity coefficient R (ω) of title materials is characterized by an averages value where these are reaches approximately 45% for a photon energy equal to ~6.5 eV. Whereas the static reflectivity coefficient R (0) has a value for a maximum of 0.26. The magnitude of $R(\omega)$ is higher than 23.5 (24.5) in an energy range 0–12.6 eV (0–9.6 eV) for Sr_3GaAs_3 (Ba_3GaAs_3), and $R(\omega)$ curve exhibits some maxima and humps in the aforementioned energy range. For photon energy higher than 12.5 (9.6 eV) for Sr_3GaAs_3 (Ba_3GaAs_3).

c) To describe the energy loss of a fast electron traversing in a material, the spectrum of the electron energy loss function L(w) is depicted in **Fig. 1.10.** Where the primary peak location is usually associated with the plasma frequency [38]. One can see that the L (w) peak is at edges in the reflection spectrum, it is at approximately 12.9 eV for Sr_3GaAs_3, as we note two peaks almost at 9.8 eV and 11.5 eV for Ba_3GaAs_3.

d) The refractive index is interesting parameter in optoelectronic devices. **Fig. 1.10** represents the refractive index n(ω) for three different orientations in an extensive spectral region reaches to 30 eV. We note at the lower energy limit that n(0) (the static refractive index) value for Sr_3GaAs_3 (Ba_3GaAs_3) is listed in **Table 1.8**. As we see the refractive index increases in about the 0 - 2.5 eV energy range, after that it decreases, where the n(ω) maximum value of Sr_3GaAs_3 (Ba_3GaAs_3) exceed 3.36 (3.62) at photon energy of approximately to 2.54 eV (1.97eV) for the ***E*||*b***, then it decreases rapidly to a minimum value of ~0.44 at ~11.93 eV for Sr_3GaAs_3 and ~0.5 at ~9.10 eV for Ba_3GaAs_3.

e) The extinction coefficient k(ω) reaches its maximum (around 2.5) almost at 4.5 eV for both studied compounds for ***E*||*b*** polarization. From **Fig. 1.10**, the optical properties of the title compounds exhibit a noticeable anisotropy.

f) As con be determined an important parameter, static anisotropy, reflecting the photonic response through the material crystallographic orientations. The static anisotropy expressed as follows [44]:

$$A_{OPT} = \left[\frac{n(0)^{[dir]}}{n(0)^{[poly]}}, \frac{\varepsilon_1(0)^{[dir]}}{\varepsilon_1(0)^{[poly]}} \right] \quad (1.20)$$

Here, $n(0)^{[dir]}$ $\varepsilon_1(0)^{[dir]}$ are the value of along x-, y- and z-axes, $n(0)^{[poly]}$ $\varepsilon_1(0)^{[poly]}$ are its values in polycrystalline. A material is optically isotropic if $A_{OPT} = 1$, otherwise, it is optically anisotropic. The degree of deviation of A_{OPT} from unity reveals the extent of the optical anisotropy. The values of A_{OPT} are listed in **Table 1.8**. According to this table, the studied compounds exhibit a sure optical anisotropy, particularly with regard to y- and z-axes.

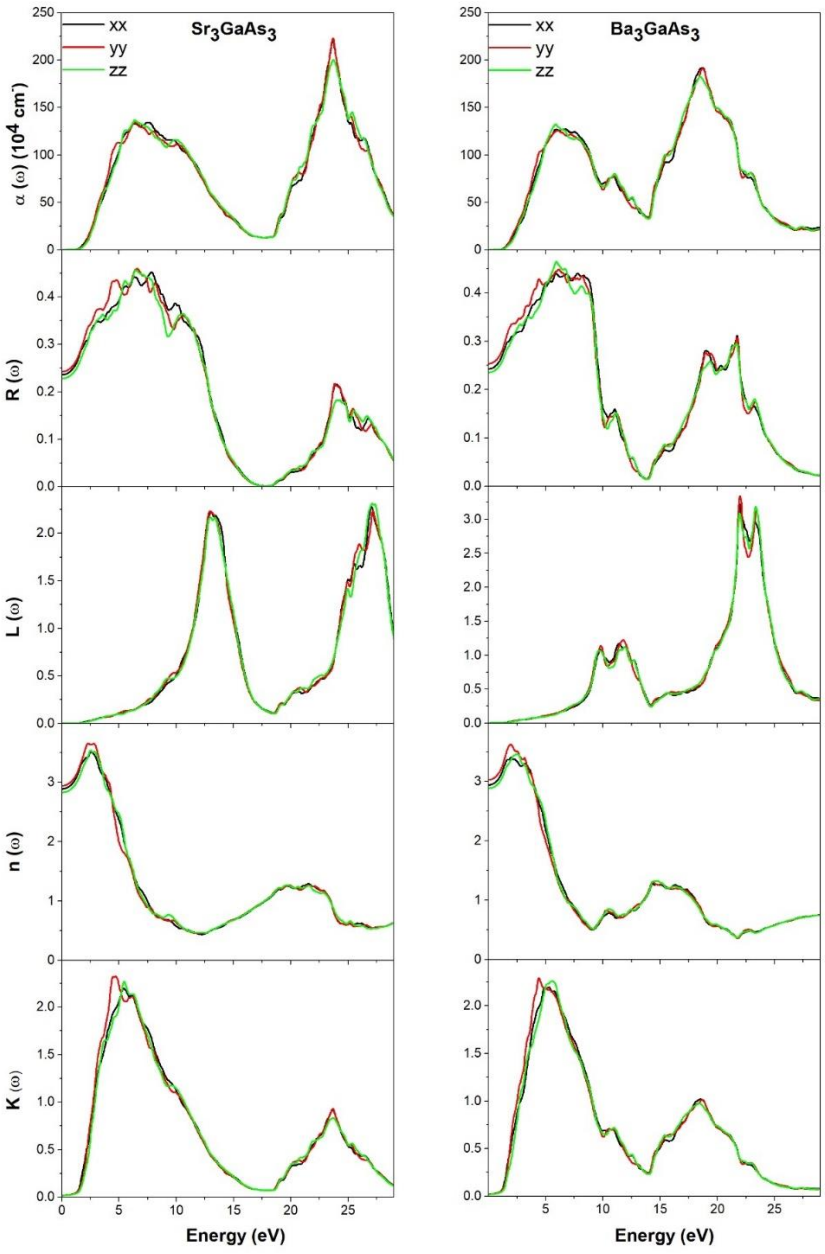

Fig. 1.10: Calculated absorption coefficient α(ω), electron energy-loss function L(ω), reflectivity R(ω), refraction index n(ω) and extinction coefficient k(ω) for Sr_3GaAs_3 and Ba_3GaAs_3.

1.2.5 Thermoelectric properties

Seebeck's effect [45] and peltier's effect [46] phenomena are caused by the conversion between heat and electricity such as in generator and cooling (refrigerator) applications, resepectively. For thermoelectric materials with highly efficient, figure of merit ZT (dimensionless parameter) has large valeus and have no limit to it value [47]. Figure of merit defined as: $ZT = S^2\sigma T / k$, where S is Seebeck coefficient or thermopower, σ is the electrical conductivity ($PF = S^2\sigma / \tau$ is called power factor), τ is the relaxation time, T is the absolute temperature, $k = k_e + k_l$ thermal conductivity, k_e is the electronic thermal conductivity and k_l is the lattice thermal conductivity, k_l is frequently calculated as the difference between k and k_e from Wiedemann–Franz equation: $k_e = L\sigma T$, where L is the Lorenz factor, 2.4×10^{-8} $J^2K^{-2}C^{-2}$ for free electrons[48].

So, the field of thermoelectric materials is needing research focused on minimizing the thermal conductivity and large power factor. The transport properties of Sr_3GaAs_3 and Ba_3GaAs_3 compounds were calculated based on the calculated mBJ-GGA electronic structure using the Boltzmann theory[49] as executed in the BoltzTraP code[12]. The calculated of the electrical conductivity scaled by relaxation time (σ / τ), electronic thermal conductivity scaled by relaxation time (k_e / τ), power factor ($PF = S^2\sigma / \tau$), Seebeck coefficient (*S*), the thermoelectric figure of merit (*ZT*) as a function of charge-carrier concentration between 10^{18} cm^{-3} and 10^{21} cm^{-3} aimed to get better thermoelectric performance [38], [48] for both the *n*-type and *p*-type doped studied compounds at 300, 600 and 900 K, Seebeck coefficient along the X, Y and Z axes (*S*) and the thermoelectric figure of merit (*ZT*) along the X, Y and Z axes as a same function at 600K are shown in **Fig. 1.11** and **Fig. 1.12**, respectively. The Seebeck coefficient (*S*) of holes and electrons in a non-degenerate semiconductor with parabolic bands are [50-51]:

$$S_h = \frac{k_0}{e}\left[\ln\left(\frac{N_V}{p}\right) + 2.5 - r\right] \quad \text{and} \quad S_e = -\frac{k_0}{e}\left[\ln\left(\frac{N_C}{n}\right) + 2.5 - r\right]$$

Where r, S_h, S_e, N_V, N_C, n and p are the scattering mechanism parameter, the Seebeck coefficients of hole, the Seebeck coefficients of electron, the effective density of states in valence band, the effective density of states in conduction band, the number of electron carriers, and the number of hole carriers, respectively.

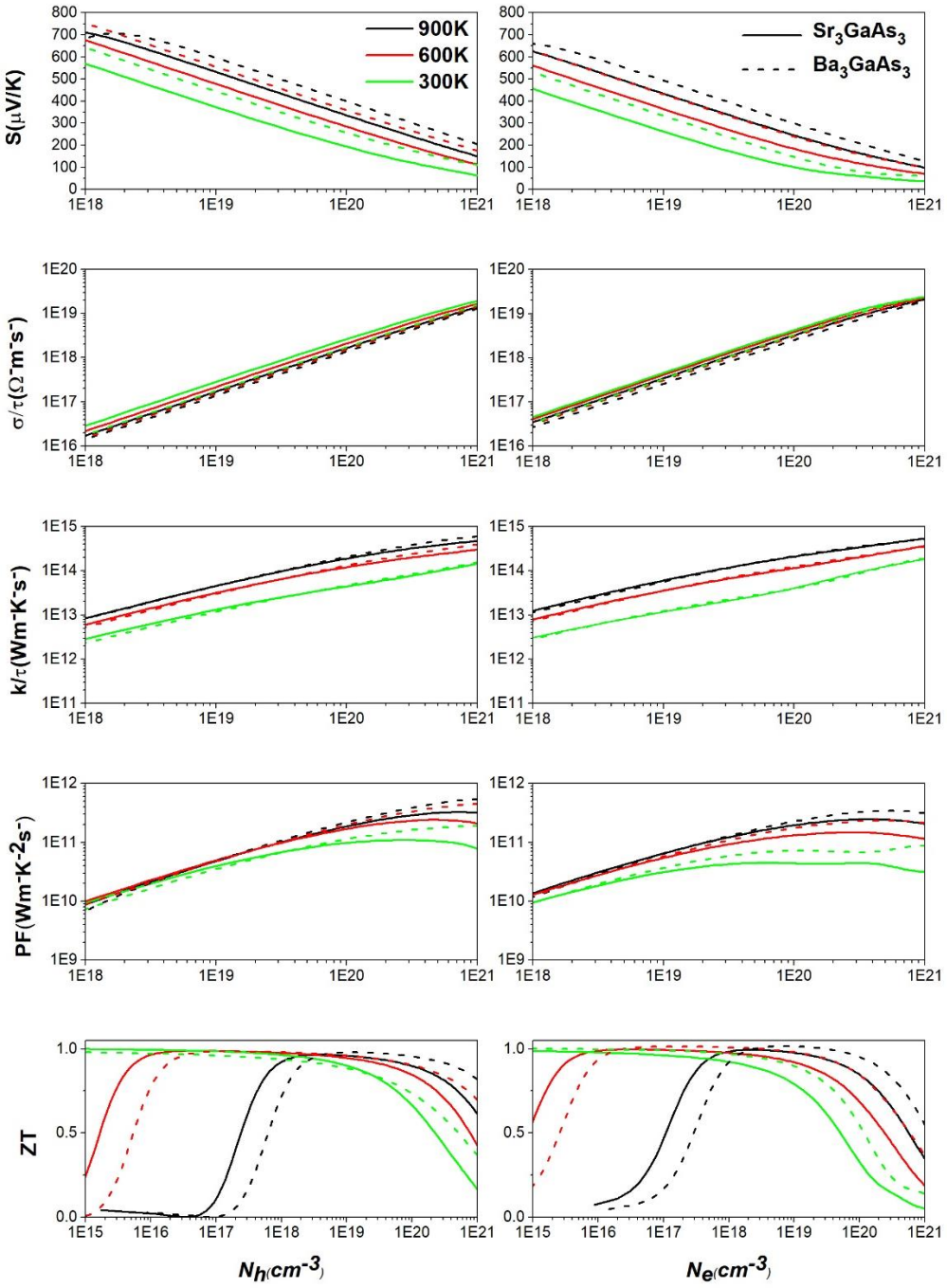

Fig. 1.11: Transport coefficients of the Seebeck coefficient (S), electrical conductivity over relaxation time (σ / τ), electronic thermal conductivity over relaxation time (k_e / τ), power factor ($PF = S^2\sigma / \tau$) and figure of merit (ZT) as a function of carrier concentration 10^{18} cm^{-3} and 10^{21} cm^{-3} for the *n*-type and *p*-type doped Sr_3GaAs_3 and Ba_3GaAs_3 compounds at 300, 600 and 900 K.

For mixed and degenerate semiconductors, the combined Seebeck coefficient is given by[51-52]:

$$S = \frac{S_e\sigma_e + S_h\sigma_h}{\sigma_e + \sigma_h} \quad (1.21) \qquad \text{and} \qquad S = m^*_{DOS} T \frac{8}{3e}\left(\frac{\pi k_B}{h}\right)^2 \left(\frac{\pi}{3n}\right)^{2/3} \quad (1.22)$$

Where k_B is the Boltzmann constant, T is the temperature, n is the carrier concentration and m^*_{DOS} is the density of states effective mass, it is given by:

$$m^*_{DOS} = \left(m^*_{xx} m^*_{yy} m^*_{zz}\right)^{1/3} N_V^{2/3} \quad (1.23)$$

Where m^*_{xx}, m^*_{yy} and m^*_{zz} are the band effective mass components along $\Gamma - X$, $\Gamma - Y$ and $\Gamma - Z$, respectively and N_V is the band degeneracy.

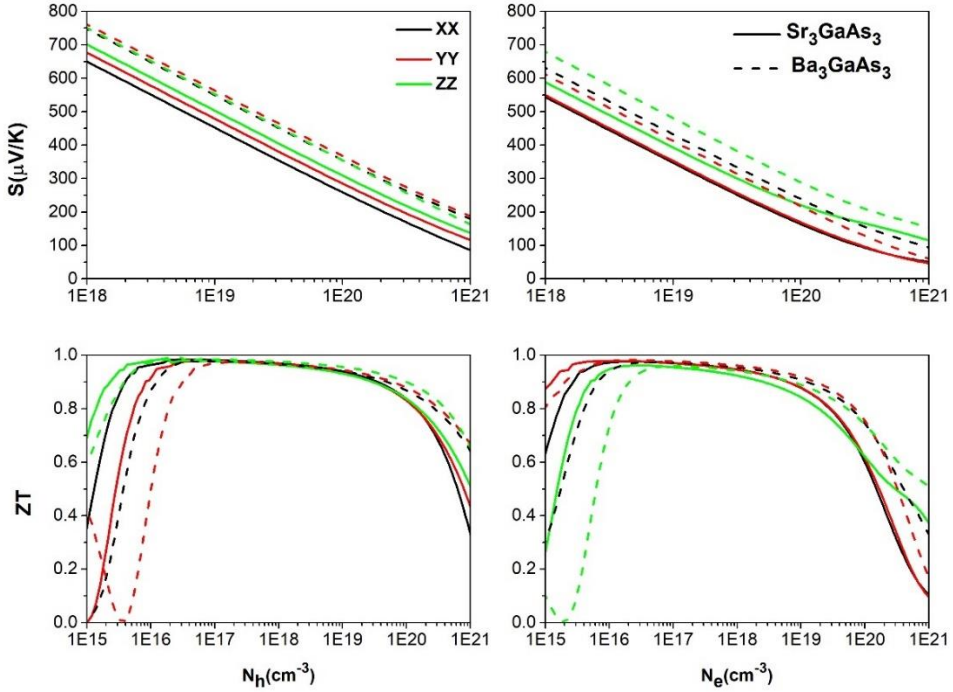

Fig. 1.12: Representation of Seebeck coefficient (*S*) (figure of merit (*ZT*) along the X, Y and Z axes) as a function of carrier concentration 10^{18} (10^{15}) cm^{-3} and 10^{21} cm^{-3} for the *n*-type and *p*-type doped Sr_3GaAs_3 and Ba_3GaAs_3 compounds at 600 K.

According to **Fig. 1.11** and **Fig. 1.12**, we can conclude the following:

a) Effect of charges carrier concentration and temperature

The extent of Seebeck coefficient is inversely proportional with the charges carrier concentration for both studied compounds *n*-type and *p*-type doping, while the electrical conductivity, the thermal conductivity and the power factor have been directly proportional at the same temperature. There is a fairly inverse relationship between electrical conductivity and temperature, i.e., that Sr_3GaAs_3 and Ba_3GaAs_3 become has behavior of the conductor at high temperature, because the electrical conductivity at the semiconductors is directly related to the temperature. The Seebeck coefficient, the power factor and the thermal conductivity have a directly proportional to the temperature at the same carrier concentration. This is a common trend in the thermoelectric materials.

b) Effect of substitution Alkaline earth (Sr, Ba) atoms and doping type

For the Seebeck coefficient efficiency, the effect of *p*-type doping at Sr_3GaAs_3 and Ba_3GaAs_3 compounds is slightly larger than *n*-type, because of the hole effective mass is heavier than the electron effective mass (as shown in **Table 1.4**), for the carrier concentration equal $10^{18}cm^{-3}$, Seebeck coefficient of *p*-type Sr_3GaAs_3 (Ba_3GaAs_3) equal to 560 μV/K (650 μV/K) at 300K. Meanwhile, Seebeck coefficient of *n*-type title compounds equal to 450 μV/K (540 μV/K) corresponding to same conditions. The efficient of *p*-type and *n*-type doped Ba_3GaAs_3 is more considerable than Sr_3GaAs_3 one. Thus, one can suggest that Ba_3GaAs_3 with a greater interest and Sr_3GaAs_3 with *p*-type doping are more appropriate for thermoelectric performance than the *n*-type ones. The *p*-type and *n*-type doped Sr_3GaAs_3 is large electrical conductivity than Ba_3GaAs_3 ones. We note that electrical conductivity of the *n*-type doped studied compounds are large than *p*-type ones, these results are expected, because the hole effective mass is heavier than the electron effective mass.

c) Figure of merit (ZT)

From **Fig. 1.11**, one can observe the variation of ZT as function of carrier concentration, where the figure of merit reaches its maximum at deference carrier concentration of both the *n*-type and *p*-type doped investigated compounds for 300, 600 and 900 K. **Table 1.10**, conclude the maximum of figure of merit at the same temperature and charge-carrier concentration, the maximum of ZT for the *p*-type doped studied compounds are

slightly less than that of the *n*-type doped ones and the *p*-type and *n*-type doped Ba_3GaAs_3 is often large than Sr_3GaAs_3 one. The figure of merit ZT reaches a maximum of 1.02 for an electron concentration of 7×10^{18} cm^{-3} of Ba_3GaAs_3 compound at 900k.

Table 1.10: Maximum values of figure of merit, at differences temperature and charge-carrier concentration for the *p*-type and *n*-type doped Sr_3GaAs_3 and Ba_3GaAs_3 compounds.

	Sr_3GaAs_3						**Ba_3GaAs_3**					
	Hole			**Electron**			**Hole**			**Electron**		
T(k)	900	600	300	900	600	300	900	600	300	900	600	300
ZT	0.96	0.99	1	0.99	1	0.99	0.98	0.98	0.99	1.02	1.01	1
cc (cm^{-3})	4.10^{18}	5.10^{16}	2.10^{13}	2.10^{18}	3.10^{16}	1.10^{13}	1.10^{19}	2.10^{17}	2.10^{13}	7.10^{18}	1.10^{17}	1.10^{13}

d) Thermoelectric anisotropy

According **Fig. 1.12**, Seebeck coefficient of the *p*-type and *n*-type compounds along the z-axis are larger than the corresponding ones along x- and y-axes, due to of the directly proportional between the charge-carrier masses and Seebeck coefficient. So, Seebeck coefficient of Sr_3GaAs_3 and Ba_3GaAs_3 are anisotropic.

e) Quality of the Sr_3GaAs_3 and Ba_3GaAs_3 in thermoelectric field

The TE quality of compounds regarded as important factors to estimate Seebeck coefficient and figure of merit (ZT), we compared Sr_3GaAs_3 and Ba_3GaAs_3 Zintl phase one to some in A_3TrPn_3 system discovered. Where A is Ca, Sr and Ba atoms from Alkaline earth, Tr is Al, Ga and In atoms, Pn is p, As and Sb atoms, for example Ca_3AlSb_3, Sr_3AlSb_3 [52], Sr_3AlAs_3 and Ba_3AlAs_3 [53].

Table 1.11: Values of Seebeck coefficient at 300K and charge-carrier concentration of 4×10^{18} cm^{-3} for some compounds in system A_3TrPn_3 Zintl phase.

	[52]Ca_3AlSb_3		**[52]Sr_3AlSb_3**		**[53]Sr_3AlAs_3**		**[53]Ba_3AlAs_3**		**Sr_3GaAs_3**		**Ba_3GaAs_3**	
Doping type	***n***	***p***	***n***	***p***	***n***	***p***	***n***	***p***	***n***	***p***	***n***	***p***
S (μV/K)	380	430	480	500	327	442	404	472	331	454	408	514

From this table, we can note the following:

- Generally, Seebeck coefficient of studied compounds (Sr_3GaAs_3 and Ba_3GaAs_3) has the largest values
- In the A_3TrPn_3 system, when the atoms are larger, the Seebeck coefficient increases. So, we think the big values of Seebeck coefficient will be at Ba_3InAs_3 and Ba_3GaSb_3 (found stable compounds) for A_3TrPn_3 system.
- Under the same conditions, the values of Seebeck coefficient for A_3TrPn_3 system are greater than their values at a traditional thermoelectric Bi_2Te_3 material (313 μV/K for the *p*-type and 196 μV/K for the *n*-type [54]).

So, one can propose that the Zintl phase Sr_3GaAs_3 and Ba_3GaAs_3 as probable candidates for thermoelectric applications if one can further reduce their thermal conductivities by alloying, nano-structuring, superlattice growth or other techniques[38]. As can be enhanced these results through doping with Zn^{2+} on the Ga^{3+} site under $(Sr\text{-}Ba)_3Ga_{1-x}Zn_xAs_3$ (x= 0.0 to 0.1) for *p*-type[55].

References

[1] J. P. Perdew *et al.*, "Restoring the Density-Gradient Expansion for Exchange in Solids and Surfaces," *Phys. Rev. Lett.*, vol. 100, no. 13, p. 136406, Apr. 2008, doi: 10.1103/PhysRevLett.100.136406.

[2] S. J. Clark *et al.*, "First principles methods using CASTEP," *Z. Für Krist. - Cryst. Mater.*, vol. 220, no. 5–6, pp. 567–570, May 2005, doi: 10.1524/zkri.220.5.567.65075.

[3] D. Vanderbilt, "Soft self-consistent pseudopotentials in a generalized eigenvalue formalism," *Phys. Rev. B*, vol. 41, no. 11, pp. 7892–7895, Apr. 1990, doi: 10.1103/PhysRevB.41.7892.

[4] H. J. Monkhorst and J. D. Pack, "Special points for Brillouin-zone integrations," *Phys. Rev. B*, vol. 13, no. 12, pp. 5188–5192, Jun. 1976, doi: 10.1103/PhysRevB.13.5188.

[5] T. H. Fischer and J. Almlof, "General methods for geometry and wave function optimization," *J. Phys. Chem.*, vol. 96, no. 24, pp. 9768–9774, Nov. 1992, doi: 10.1021/j100203a036.

[6] A. Bedjaoui *et al.*, "Structural, elastic, electronic and optical properties of the novel quaternary diamond-like semiconductors Cu_2MgSiS_4 and Cu_2MgGeS_4," *Solid State Sci.*, vol. 70, pp. 21–35, Aug. 2017, doi: 10.1016/j.solidstatesciences.2017.06.007.

[7] F. Tran and P. Blaha, "Accurate Band Gaps of Semiconductors and Insulators with a Semilocal Exchange-Correlation Potential," *Phys. Rev. Lett.*, vol. 102, no. 22, p. 226401, Jun. 2009, doi: 10.1103/PhysRevLett.102.226401.

[8] D. Koller, F. Tran, and P. Blaha, "Merits and limits of the modified Becke-Johnson exchange potential," *Phys. Rev. B*, vol. 83, no. 19, p. 195134, May 2011, doi: 10.1103/PhysRevB.83.195134.

[9] P. Blaha, K. Schwarz, F. Tran, R. Laskowski, G. K. H. Madsen, and L. D. Marks, "WIEN2k: An APW+lo program for calculating the properties of solids," *J. Chem. Phys.*, vol. 152, no. 7, p. 074101, Feb. 2020, doi: 10.1063/1.5143061.

[10] C. Ambrosch-Draxl and J. O. Sofo, "Linear optical properties of solids within the full-potential linearized augmented planewave method," *Comput. Phys. Commun.*, vol. 175, no. 1, pp. 1–14, Jul. 2006, doi: 10.1016/j.cpc.2006.03.005.

[11] S. Z. Karazhanov, P. Ravindran, A. Kjekshus, H. Fjellvag, and B. G. Svensson, "Electronic structure and optical properties of ZnX (X=O, S, Se, Te)," *Phys. Rev. B*, vol. 75, no. 15, p. 155104, Apr. 2007, doi: 10.1103/PhysRevB.75.155104.

[12] G. K. H. Madsen and D. J. Singh, "BoltzTraP. A code for calculating band-structure dependent quantities," *Comput. Phys. Commun.*, vol. 175, no. 1, pp. 67–71, Jul. 2006, doi: 10.1016/j.cpc.2006.03.007.

[13] S. S. Stoyko, L. H. Voss, H. He, and S. Bobev, "Synthesis, Crystal and Electronic Structures of the Pnictides AE_3TrPn_3 (AE = Sr, Ba; Tr = Al, Ga; Pn = P, As)," *Crystals*, vol. 5, no. 4, Art. no. 4, Dec. 2015, doi: 10.3390/cryst5040433.

[14] G. Yang, G. Zhang, C. Wang, and Y. Wang, "The unusual chemical bonding and thermoelectric properties of a new type Zintl phase compounds $Ba_3Al_2As_4$," *Solid State Commun.*, vol. 237–238, pp. 28–33, Jul. 2016, doi: 10.1016/j.ssc.2016.03.018.

[15] P. Pichanusakorn and P. Bandaru, "Nanostructured thermoelectrics," *Mater. Sci. Eng. R Rep.*, vol. 67, no. 2–4, pp. 19–63, Jan. 2010, doi: 10.1016/j.mser.2009.10.001.

[16] M. Ya. Rudysh *et al.*, "First-principles analysis of physical properties anisotropy for the Ag2SiS3 chalcogenide semiconductor," *J. Alloys Compd.*, vol. 826, p. 154232, Jun. 2020, doi: 10.1016/j.jallcom.2020.154232.

[17] V. Weippert, A. Haffner, A. Stamatopoulos, and D. Johrendt, "Supertetrahedral Layers Based on GaAs or InAs," *J. Am. Chem. Soc.*, vol. 141, no. 28, pp. 11245–11252, Jul. 2019, doi: 10.1021/jacs.9b04712.

[18] J. Feng and B. Xiao, "Crystal Structures, Optical Properties, and Effective Mass Tensors of $CH_3NH_3PbX_3$ (X = I and Br) Phases Predicted from HSE06," *J. Phys. Chem. Lett.*, vol. 5, no. 7, pp. 1278–1282, Apr. 2014, doi: 10.1021/jz500480m.

[19] M. Born and K. Huang, *Dynamical Theory of Crystal Lattices*. in Oxford Classic Texts in the Physical Sciences. Oxford, New York: Oxford University Press, 1998.

[20] F. Mouhat and F.-X. Coudert, "Necessary and sufficient elastic stability conditions in various crystal systems," *Phys. Rev. B*, vol. 90, no. 22, p. 224104, Dec. 2014, doi: 10.1103/PhysRevB.90.224104.

[21] B. B. Karki, L. Stixrude, S. J. Clark, M. C. Warren, G. J. Ackland, and J. Crain, "Structure and elasticity of MgO at high pressure," *Am. Mineral.*, vol. 82, no. 1–2, pp. 51–60, 1997.

[22] W. Y. Ching, S. Aryal, P. Rulis, and W. Schnick, "Electronic structure and physical properties of the spinel-type phase of BeP_2N_4 from all-electron density functional calculations," *Phys. Rev. B*, vol. 83, no. 15, p. 155109, Apr. 2011, doi: 10.1103/PhysRevB.83.155109.

[23] A. Bedjaoui, A. Bouhemadou, and S. Bin-Omran, "Structural, elastic and thermodynamic properties of tetragonal and orthorhombic polymorphs of Sr_2GeN_2: an ab initio investigation," *High Press. Res.*, vol. 36, no. 2, pp. 198–219, Apr. 2016, doi: 10.1080/08957959.2016.1167202.

[24] P. Ravindran, L. Fast, P. A. Korzhavyi, B. Johansson, J. Wills, and O. Eriksson, "Density functional theory for calculation of elastic properties of orthorhombic crystals: Application to TiSi2," *J. Appl. Phys.*, vol. 84, no. 9, pp. 4891–4904, Nov. 1998, doi: 10.1063/1.368733.

[25] P. Lloveras, T. Castán, M. Porta, A. Planes, and A. Saxena, "Influence of Elastic Anisotropy on Structural Nanoscale Textures," *Phys. Rev. Lett.*, vol. 100, no. 16, p. 165707, Apr. 2008, doi: 10.1103/PhysRevLett.100.165707.

[26] S. I. Ranganathan and M. Ostoja-Starzewski, "Universal Elastic Anisotropy Index," *Phys. Rev. Lett.*, vol. 101, no. 5, p. 055504, Aug. 2008, doi: 10.1103/PhysRevLett.101.055504.

[27] P. Mao, B. Yu, Z. Liu, F. Wang, and Y. Ju, "First-principles investigation on mechanical, electronic, and thermodynamic properties of Mg_2Sr under high pressure," *J. Appl. Phys.*, vol. 117, no. 11, p. 115903, Mar. 2015, doi: 10.1063/1.4915339.

[28] D. H. Chung and W. R. Buessem, "The Elastic Anisotropy of Crystals," *J. Appl. Phys.*, vol. 38, no. 5, pp. 2010–2012, Jun. 2004, doi: 10.1063/1.1709819.

[29] C. M. Kube, "Elastic anisotropy of crystals," *AIP Adv.*, vol. 6, no. 9, p. 095209, Sep. 2016, doi: 10.1063/1.4962996.

[30] J. F. Nye, *Physical Properties of Crystals: Their Representation by Tensors and Matrices*. Oxford, New York: Oxford University Press, 1985.

[31] H. Amamou, B. Ferhat, and A. Bois, "Calculation of the Voigt Function in the Region of Very Small Values of the Parameter; Where the Calculation Is Notoriously Difficult," *Am. J. Anal. Chem.*, vol. 04, no. 12, pp. 725–731, 2013, doi: 10.4236/ajac.2013.412087.

[32] G. Kipkemei Chirchir, W. Mueni Mulwa, and B. Ibrahim Adetunji, "Structural, Electronic and Mechanical Properties of Re Doped $FeMnP_{0.67}A_{0.33}$ (A=Ga and Ge): A DFT Study," *Int. J. Phys.*, vol. 10, no. 1, pp. 70–78, Feb. 2022, doi: 10.12691/ijp-10-1-6.

[33] R. Hill, "The Elastic Behaviour of a Crystalline Aggregate," *Proc. Phys. Soc. Sect. A*, vol. 65, no. 5, p. 349, May 1952, doi: 10.1088/0370-1298/65/5/307.

[34] O. Boudrifa, A. Bouhemadou, Ş. Uğur, R. Khenata, S. Bin-Omran, and Y. Al-Douri, "Structural, electronic, optical and elastic properties of the complex K_2PtC_{l6}-structure hydrides $ARuH_6$ (A = Mg, Ca, Sr and Ba): first-principles study," *Philos. Mag.*, vol. 96, no. 22, pp. 2328–2361, Aug. 2016, doi: 10.1080/14786435.2016.1198874.

[35] E. Schreiber, O. L. Anderson, N. Soga, and J. F. Bell, "Elastic Constants and Their Measurement," *J. Appl. Mech.*, vol. 42, no. 3, pp. 747–748, Sep. 1975, doi: 10.1115/1.3423687.

[36] O. L. Anderson, "A simplified method for calculating the debye temperature from elastic constants," *J. Phys. Chem. Solids*, vol. 24, no. 7, pp. 909–917, Jul. 1963, doi: 10.1016/0022-3697(63)90067-2.

[37] S. F. Pugh, "XC2. Relations between the elastic moduli and the plastic properties of polycrystalline pure metals," *Lond. Edinb. Dublin Philos. Mag. J. Sci.*, vol. 45, no. 367, pp. 823–843, Aug. 1954, doi: 10.1080/14786440808520496.

[38] A. Bouhemadou *et al.*, "Electronic, optical, elastic, thermoelectric and thermodynamic properties of the spinel oxides $ZnRh_2O_4$ and $CdRh_2O_4$," *J. Alloys Compd.*, vol. 774, pp. 299–314, Feb. 2019, doi: 10.1016/j.jallcom.2018.09.338.

[39] W. Y. Ching, S. Aryal, P. Rulis, and W. Schnick, "Electronic structure and physical properties of the spinel-type phase of BeP_2N_4 from all-electron density functional calculations," *Phys. Rev. B*, vol. 83, no. 15, p. 155109, Apr. 2011, doi: 10.1103/PhysRevB.83.155109.

[40] V. Natarajan *et al.*, "Crystal Growth, Thermal, Mechanical and Optical Properties of a New Organic Nonlinear Optical Material: Ethyl P-Dimethylamino Benzoate (EDMAB),"

J. Miner. Mater. Charact. Eng., vol. 10, no. 01, pp. 1–11, 2011, doi: 10.4236/jmmce.2011.101001.

[41] M. Fox, *Optical Properties of Solids*, Second Edition, Second Edition. in Oxford Master Series in Physics. Oxford, New York: Oxford University Press, 2010.

[42] M. Alouani and J. M. Wills, "Calculated optical properties of Si, Ge, and GaAs under hydrostatic pressure," *Phys. Rev. B*, vol. 54, no. 4, pp. 2480–2490, Jul. 1996, doi: 10.1103/PhysRevB.54.2480.

[43] D. R. Penn, "Wave-Number-Dependent Dielectric Function of Semiconductors," *Phys. Rev.*, vol. 128, no. 5, pp. 2093–2097, Dec. 1962, doi: 10.1103/PhysRev.128.2093.

[44] D. Cherrad *et al.*, "Ultra soft pseudo potential investigation of fundamental physical properties of $CaXO_3$ (X=Sn and Hf) distorted perovskites: A reference study to the perfect perovskites," *Phys. B Condens. Matter*, vol. 429, pp. 95–105, Nov. 2013, doi: 10.1016/j.physb.2013.08.002.

[45] T. J. Seebeck, "Magnetic polarization of metals and minerals," *Abh. Dtsch. Akad. Wiss.*, vol. 265, 1823.

[46] J. C. Peltier, "Nouvelle experieces sur la caloricite des courans electrique," *Ann Chim*, vol. 371, 1834.

[47] M. K. Yadav and B. Sanyal, "First principles study of thermoelectric properties of Li-based half-Heusler alloys," *J. Alloys Compd.*, vol. C, no. 622, pp. 388–393, 2015, doi: 10.1016/j.jallcom.2014.10.025.

[48] G. J. Snyder and E. S. Toberer, "Complex thermoelectric materials," *Nat. Mater.*, vol. 7, no. 2, pp. 105–114, Feb. 2008, doi: 10.1038/nmat2090.

[49] J.R. Chelikowsky and S.G. Louie. Quantum Theory of Real Materials. Kluwer Press, Amsterdam, 1996.

[50] Y. L. Yan, Y. X. Wang, and G. B. Zhang, "Electronic structure and thermoelectric performance of Zintl compound $Ca_5Ga_2As_6$," *J. Mater. Chem.*, vol. 22, no. 38, pp. 20284–20290, Sep. 2012, doi: 10.1039/C2JM32945J.

[51] M. C. Chen, "A quick thermoelectric technique for typing HgCdTe at liquid nitrogen temperature," *J. Appl. Phys.*, vol. 71, no. 7, pp. 3636–3638, Apr. 1992, doi: 10.1063/1.350926.

[52] Q. Shi, Z. Feng, Y. Yan, and Y. X. Wang, "Electronic structure and thermoelectric properties of Zintl compounds A_3AlSb_3 (A = Ca and Sr): first-principles study," *RSC Adv.*, vol. 5, no. 80, pp. 65133–65138, Jul. 2015, doi: 10.1039/C5RA09804A.

[53] A. Benahmed *et al.*, "Structural, elastic, electronic, optical and thermoelectric properties of the Zintl-phase Ae_3AlAs_3 (Ae = Sr, Ba)," *Philos. Mag.*, vol. 98, no. 13, pp. 1217–1240, May 2018, doi: 10.1080/14786435.2018.1425013.

[54] S. K. Mishra, S. Satpathy, and O. Jepsen, "Electronic structure and thermoelectric properties of bismuth telluride and bismuth selenide," *J. Phys. Condens. Matter*, vol. 9, pp. 461–470, Jan. 1997, doi: 10.1088/0953-8984/9/2/014.

[55] A. Zevalkink, W. G. Zeier, G. Pomrehn, E. Schechtel, W. Tremel, and G. J. Snyder, "Thermoelectric properties of Sr_3GaSb_3 – a chain-forming Zintl compound," *Energy Environ. Sci.*, vol. 5, no. 10, pp. 9121–9128, Sep. 2012, doi: 10.1039/C2EE22378C.

CHAPTER 2

THE STRUCTURAL, ELECTRONIC, ELASTIC, OPTICAL AND THERMOELECTRIC PROPERTIES OF THE ZINTL-PHASE Ba_2ZnP_2

2.1 Calculation methods and settings

First-principles study basis on the density functional theory (DFT) calculations are performed by two methods, the pseudopotential plane-wave (PP-PW) method with the GGA-PBEsol [1] functional for describe the exchange-correlation to the accuracy of the results, as implemented in the CASTEP package [2] and the full-potential linearized/augmented plane wave plus orbitales (FP-L/APW + lo) with both the GGA-PBEsol and Tran-Blaha modified Becke-Johnson (TB-mBJ) potential [3,4], which almost yields band gaps close to experimental values, as implanted in the WIEN2k code [5].

The first method is used to calculate the full optimized geometric and elastic constants, where the interaction between the valence electrons (Ba: $5s^2\ 5p^6\ 6s^2$, Zn: $3d^{10}\ 4s^2$ and P: $3s^2\ 3p^3$) and the ion core are described by the Vanderbilt ultrasoft pseudopotentials [6] (nuclei plus frozen core electrons) with the energy cut-off of 400 eV for the plane-wave and a 6×7×6 [7] k-points in Brillouin zone (BZ). For determining the minimum energy crystal structure and calculating the nine independent C_{ij}s, we used the Broyden-Fletcher-Goldfarb-Shannon algorithm (BFGS) [8] and Stress-strain method depended by Hooker's law [1] through the following settings: Total energy convergence, maximum force acting on each atom, Maximum stress and ionic displacement within 5.0×10^{-6} eV/atom, 0.01 eV/Å, 0.02 GPa and 5.0×10^{-4} Å, respectively. Where C_{ijkl} is the elastic constants tensor which is a 6×6 matrix. Using Voigt notations, the Hooke's law for an orthorhombic system is written:

$$\begin{pmatrix}\sigma_1\\ \sigma_2\\ \sigma_3\\ \sigma_4\\ \sigma_5\\ \sigma_6\end{pmatrix}=\begin{bmatrix}C_{11} & C_{12} & C_{13} & 0 & 0 & 0\\ C_{12} & C_{22} & C_{23} & 0 & 0 & 0\\ C_{13} & C_{23} & C_{33} & 0 & 0 & 0\\ 0 & 0 & 0 & C_{11} & 0 & 0\\ 0 & 0 & 0 & 0 & C_{11} & 0\\ 0 & 0 & 0 & 0 & 0 & C_{11}\end{bmatrix}\begin{pmatrix}\varepsilon_1\\ \varepsilon_2\\ \varepsilon_3\\ \varepsilon_4\\ \varepsilon_5\\ \varepsilon_6\end{pmatrix} \quad (2.1)$$

The second method is exploited for computing the properties depended of the electronic structure, when the cut-off parameter $R_{MT}K_{max}$= 9 for the spherical of the plane-wave, where R_{MT} is the smallest muffin-tin sphere radius, and the muffin-tin sphere radii of Ba, Zn and P are: 2.50, 2.50 and 2.04 Bohr, with the convergent of the total energy is stable in range 10^{-5} Ry and less than 5×10^{-4} Ry/Bohr for the force acting on each atom, are selected to the accurate calculation. As for the optical properties dependent of incident electromagnetic radiation are described by the real part ($\varepsilon_1(\omega)$) and the imaginary one ($\varepsilon_2(\omega)$), where $\varepsilon(\omega)$=

$\varepsilon_1(\omega)$ + $i\varepsilon_2(\omega)$ [9]. Theoretically, the $\varepsilon_2(\omega)$ spectrum is calculated by summing all the allowed electronic transitions from the filled valence states to the empty conduction states via the following relationship:

$$\varepsilon_2^{ij}(\omega) = \frac{Ve^2}{2\pi\hbar m_0^2\omega^2}\sum_{n,n'}\int d^3k \langle kn|\, p_i\,|kn'\rangle \times \langle kn|\, p_j\,|kn'\rangle\, f_{kn}\left(1-f_{kn'}\right)\delta\left(E_{kn'}-E_{kn}-\hbar\omega\right) \quad (2.2)$$

Here $|kn\rangle$, which is obtained from the resolution of the Kohn-Sham equations, is the wave function of the electronic state ($\vec{k}, n$) in an energy band of index *n* with a wave vector *k* and the corresponding energy is E_{kn}, P_i (i = *x*, *y*, *z*) is the momentum operator, f_{kn} is the Fermi distribution corresponding to the energy level E_{kn} and $\delta\left(E_{kn'}-E_{kn}-\hbar\omega\right)$ is the Dirac function. $\varepsilon_1(\omega)$ is deduced from $\varepsilon_2(\omega)$ using the Kramers-Kronig (KK) transformation as follows [9]:

$$\varepsilon_1^{ij}(\omega) = 1+\frac{2}{\pi}\int_0^{\infty}\frac{\varepsilon_2^{ij}(\omega')\omega' d\omega'}{\omega'^2-\omega^2} \quad (2.3)$$

For the other linear optical parameters, are inferred from $\varepsilon_1(\omega)$ and $\varepsilon_2(\omega)$ spectra, using the well-known relationships [10]. The transport properties were computed within a dense mesh of 30×30×30 k-points in the BZ. Using Boltzmann's transport theory with the constant scattering time approximation (CSTA) and the rigid band approximation (RBA) as implemented in the BoltzTraP1 code [11]. For some thermodynamic properties (such as Grüneisen parameter), we use the quasi-harmonic model, as applied in the Gibbs1 package [12]

2.2 Results and discussion

2.2.1 Structural properties

The ternary Zintl-phase dibarium zinc diphosphide compound Ba_2ZnP_2 has an orthorhombic structure, space group *Ibma* (no. 72) with two formula units in one-unit [13] **Fig. 2.1** displays (Using the 3D visualization program for structural models, VESTA) the primitive cell of Ba_2ZnP_2 contains 10 atoms (Z = 2) and there are seven free structural parameters that are not fixed by the space group symmetry, viz., *a*, *b*, *c*, x_{Ba}, y_{Ba}, x_P and y_P. In the unit cell of Ba_2ZnP_2, the three constituent elements are located in the following Wyckoff sites: Ba: 8*j* (x_{Ba}, y_{Ba}, 0); Zn: 4*b* (0 0 0); P: 8*j* (x_P, y_P, 0). According to this figure, one can note the prominent structural feature in the Ba_2ZnP_2 structure is that the Zn and P atoms form ZnP_2 tetrahedra. Also, the arrangement of P atoms products distorted octahedral-like around each

Ba atom in the structure to be at the center. The equilibrium unit-cell, the optimized values of the lattice parameters (a, b and c) and the internal atomic coordinates (x, y, z) are obtained using the pseudopotential plane-wave (PP-PW) within GGA08 (GGA-PBEsol) [1]. Where the resulting total energy volume curve was fitted to the Birch-Murnaghan equation of state [14].

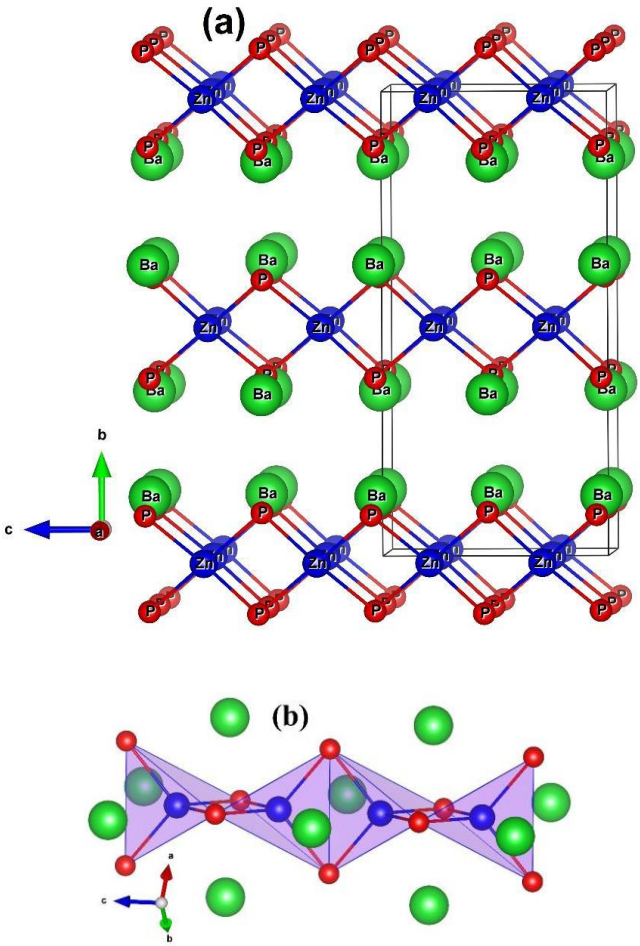

Fig. 2.1: (a) Ball-and-stick view of the Ba_2ZnP_2 structure, projected down the *a*-axis. The representation emphasizes the isolated [ZnP_4] polyanionic chains, "solvated" by the cations Ba. The orthorhombic conventional cell is outlined. (b) A close-up view of a segment of the [ZnP_4] chains, depicting the edge-shared ZnP_4 tetrahedra.

Our results are listed in **Table 2.1** and **2.2** with the available experimental. The relative deviation $d\ (\%) = (X_{opt}-X_{exp})\times 100/X_{exp}$ of the calculated lattice parameters (a, b and c) of Ba_2ZnP_2, where X_{opt} and X_{exp} are the optimized and experimental unit cell parameters, are excellent agreement between the GGA08 optimized lattice parameters values and the corresponding experimental one, which are less than -0.94%, -0.47% and -0.79%, respectively. Furthermore, the relative deviation of the averaged unit cell (d_r) defined as

follows: $d_r = (V_{uc}^{(opt)1/3} - V_{uc}^{(\exp)1/3}) / V_{uc}^{(\exp)1/3}$ [15], where $V_{uc}^{(opt)}$ and $V_{uc}^{(\exp)}$ are the optimized unit cell volume and the experimental counterpart, respectively, is usually used to quantify the average relative deviation of an optimized structure from the experimental counterpart. The calculated unit cell volume is equal to 553.1 $Å^3$ and the measured one is equal to 565.4 $Å^3$, and thus $d_r = -0.7\%$.

Table 2.1: Atomic position coordinates for the Ba_2ZnP_2 compound, compared with the available experimental.

	x		**y**		**z**	
	Present work[a]	Exp[b]	Present work[a]	Exp[b]	Present work[a]	Exp[b]
Ba_2ZnP_2						
Ba	0.19345	0.19118	0.36040	0.35970	0	0
Zn	0	0	0	0	0.25	0.25
P	0.19876	0.20008	0.10606	0.10649	0	0

[a] Using PP-PW within GGA08.

[b] Ref. [13]

The chemical bond nature can be determined from bond lengths, **Table 2.3** lists of various selected bonds, the bond length of the Zn-P is 2.488 Å, suggesting that the Zn-P bond is of strong covalent bonding character because the sum of the corresponding covalent radii of Zn (1.323 Å) and P (1.080 Å) is closely match. About of the Ba-P bond, it ranges between 3.278 and 3.412 Å, suggesting that these bonds are almost ionic nature because of the large sum of the respective covalent radii of Ba (1.323 Å) and P (1.080 Å), we will discuss this extensively later.

Table 2.2: Optimized and experimental lattice parameters of Ba_2ZnP_2.

	Ba_2ZnP_2	
	Present work[a]	Exp[b]
a (Å)	6.6926	6.756
b (Å)	13.0467	13.108
c (Å)	6.3346	6.385
V ($Å^3$)	553.1	565.4

[a] Using PP-PW within GGA08.

[b] Ref. [13].

Table 2.3: Determined interatomic distances (in Å) for Ba_2ZnP_2.

	Present work[a]	**Exp[b]**		**Present work[a]**	**Exp[b]**
Ba-Ba1	4.091	4.107	**Ba-P**	3.319	3.320
Ba-Ba2	4.416	4.370	**Ba-P3**	3.278	3.306
Ba-Ba3	4.348	4.370	**Ba-P8**	3.285	3.317
Ba-Ba4	4.091	4.107	**Ba-P2**	3.278	3.306
Ba-Zn3	3.168	3.207	**Zn-P**	2.488	2.515
Ba-Zn5	3.168	3.207	**Zn-P1**	2.488	2.515
Ba-P6	3.340	3.347	**Zn-P9**	2.488	2.515
Ba-P7	3.412	3.466	**Zn-P10**	2.488	2.515

[a] Using PP-PW within GGA08.

[b] Ref. [13].

2.2.2 Electronic properties

2.2.2.1 Band structure

Electronic band structure is a quite helpful theoretical tool to predict whether a material is conductive, semiconductor or isolator; it transmits, reflects or absorbs the visible spectrum and so on. In other words, from the band gap value, the band gap character (direct or indirect gap) and dispersion of the electronic states, one can for example predict whether a material can be an eventual candidate for thermoelectric applications or optoelectronic applications, including lighting, lasing, optical sensing, displays manufacturing, and sunlight converter and so on. Thus, it is of great importance to study the electronic structure of materials through accurate theoretical methods. The band energy dispersions for Ba_2ZnP_2 compound is calculated along the selected high-symmetry points optimized path in the Brillouin zone, red line in **Fig. 2.2**, $\Gamma \rightarrow T \rightarrow W \rightarrow R \rightarrow S \rightarrow \Gamma \rightarrow X \rightarrow T$, where T (1/2, -1/2, 0), W (3/4, -1/4, -1/4), R (1/2 0, 0), Γ (0, 0, 0), X (1/2 -1/2, 1/2). This investigation by using TB-mBJ and PBEsol within the full potential linearized/augmented plane wave plus orbitales (FP-L/APW +lo) method. As seen in **Fig. 2.3**, Ba_2ZnP_2 is semiconductor, our calculation yielded an indirect band gap located between T at VBM and X at CBM points of 1.24 and 0.57 eV for TB-mBJ and PBEsol, respectively. There are no experimental values for the band gap of the studied compound, except the calculation of *A. Balvanz, et al* [13] using the light binding linear muffin-tin orbital (TB-LMTO-ASA) with local density approximation (LDA) of 0.6

eV, and other study dependent of Yb_2CdSb_2 structure type (SG. *Cmc2₁* No. 36) of *A. Balvanz, et al* [16] using GGA-PBE with Projector Augmented Wave method under VASP code, where it was characterized by the direct band gap equal to 0.15 eV. Third, as is visible from **Fig. 2.3**, the energy band around the CBM at the X-point is much more dispersive and isotropic than that around the VBM at the T-point. In particular, the topmost valence band in the T–Γ direction is almost flat. This evidences that the hole effective mass at the VBM will be heavier and more anisotropic than the electron effective mass at the CBM. The nearly flat bands around the VBM along the high symmetry T–Γ line indicates that the hole effective mass will be much heavier along this direction. Dispersion of the energy band around the VBM demonstrates that the hole effective mass and related properties are strongly anisotropic.

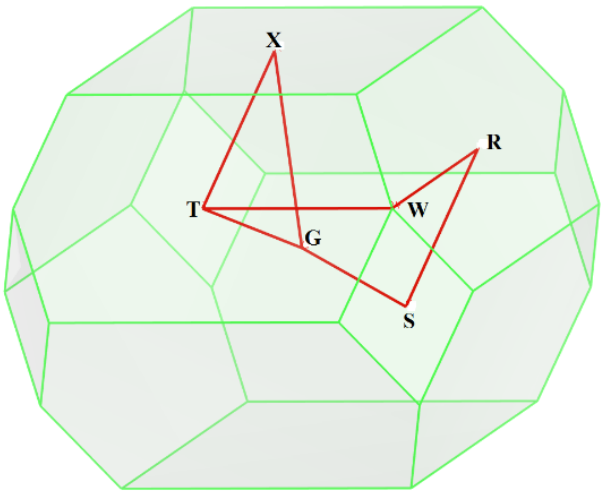

Fig. 2.2: Calculated band structure diagrams for Ba_2ZnP_2 along the selected path (red lines) in the first Brillouin zone (the green lines).

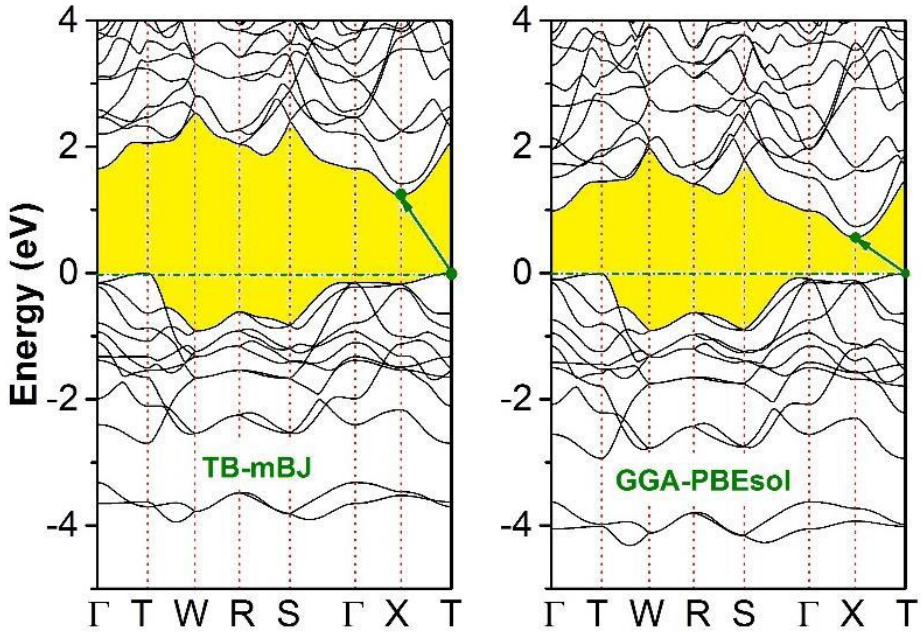

Fig. 2.3: Band structure for Ba_2ZnP_2 using the TB-mBJ and PBEsol. The Fermi level is set to zero.

2.2.2.2 Charge-carrier effective mass

The evaluated effective mass is of great importance in determining the transport properties and their related phenomena (Seebeck coefficient and electrical conductivity…etc) of materials. Therefore, it becomes needed to estimate the electron and hole effective masses of the studied compound at the band edge. The hole effective mass m_h^* (electron effective mass m_e^*) was numerically evaluated by fitting the energy band dispersions e (k) around the VBM (around the CBM) to parabolas e (k) = Ak^2, then the effective masses m^* could be compute using the following expression: $\frac{1}{m^*} = \frac{m_0}{\hbar^2}\frac{\partial^2 E(k)}{\partial k^2}$ (2.4)

The effective mass is m^*, in units of m_0 (m_0 denotes the electron rest mass). The computed effective masses in the Brillouin zone at some high symmetry points from the band dispersion around the VBM and CBM toward the considered directions are listed in **Table 2.4**. According to this table, it shows clearly that the hole effective mass at the valence band maximum is heavier than that of the electron at the conduction band minimum, this result is due to the fact that the bottommost of the conduction band is more dispersive than the topmost of the valence band, the hole effective mass along T-Γ direction is very larger than the corresponding ones along T-W and T-X directions. These results predict the hole mobility

should be lighter than the electron one in the considered compound. Hereby, the charge-carrier masses were inversely (directly) proportional with the electrical conductivity (Seebeck coefficient). Consequently, the *n*-type Ba_2ZnP_2 compound would have the largest electrical conductivity, while the *p*-type Ba_2ZnP_2 compound would have the highest Seebeck coefficient. it is obvious from **Table 2.4** that the electron effective mass is almost isotropic, while the hole effective mass is strongly anisotropic, which can be traced back to the flatter band around the VBM along the high symmetry T-Γ direction than along the T-W and T-X directions.

Table 2.4: Calculated electron and hole effective masses ($m_e^*$and m_h^*, respectively; in unit of electron rest mass) for Ba_2ZnP_2 compound at VBM and CBM within TB-mBJ along some directions in BZ.

	direction	m_e^*	**direction**	m_h^*
Ba_2ZnP_2	X-T	0.81	T-Γ	10.6
	X-Γ	0.81	T-W	0.18
			T-X	4.26

2.2.2.3 Density of states

The calculated total density of states TDOS (states/eV/unit-cell) and atomic-resolved *l*-projected density of states PDOS (states/eV/atom) diagrams conduct us toward a close examination of the electronic structure. Both curves (i.e., TDOS and PDOS) of title compound using TB-mBJ are described in **Fig. 2.4**. From these diagrams, one observes that the electronic states composing the valence bands of the Ba_2ZnP_2 compound mainly come from the Zn and P atoms, while the states of the conduction band bottom are dominantly formed from the Ba atom. These diagrams appear clearly that the TDOS part valance bands between -10 eV and the Fermi level for Ba_2ZnP_2 compound. One can divide the formed range into six main pseudo regions where the subbands V5 and V6, located in the lowest energy region far from the Fermi level, not shown in **Fig. 2.3** for clarity of the figure, are originated from core electrons.

Firstly, V_1, Beneath Fermi level, there is a structure start from -2.9 eV with barycentre is of -2.44 eV, it contains two main parts formed by a hybridization between P-3p, Zn-4p3d and Ba-5p4d orbitals with great contribution from the two latter states. One notes that the Zn-

4p is hybridized with the P-3p, indicating a covalent character of the Zn-P bond. The very weak presence of the valence two Ba-6s electrons evidences that the Ba atom has donated almost these two valence Ba-6s electrons to the [ZnP_4] anion, indicating an ionic bonding between the Ba cation and the [ZnP_4] anion. Contribution of the Ba-5p4d states in the V1 subband and their hybridization with the P-3p, indicating the presence of a contribution of covalent nature in the bonding between the Ba cation and the [ZnP_4] anion. This behavior of the Ba cation seems to violate the Zintl concept which supposes that Ba is only an electron donor. One can conclude that the bonding between the Ba and the anion [ZnP_2] is dominantly of ionic character with weak contribution of covalent nature due to the hybridization between the Ba-5p4d and the P-3p states. Secondly V_2, is ranged from-4.0 to -3.2 eV, this is mainly arisen by contribution of Zn-4s state and P-3p state with great influence, so presence of the covalent bond between Zn and P atoms. Thirdly V_3, we can see one big peak in range -7.2 to -6.4 eV as a result of Zn-3d. Fourthly, V_4 confined between -9.8 and -8.6 eV, this energy range was attributed to the contribution of 3s state of P atom and a small contribution from the 3d-Zn states with small contributions from the Ba-5p and Zn-4p4s states. The conduction bands, ranging from the CBM up, consists mainly of the Ba-4d states. Hence, the 4d-Ba electrons would play an important role in the electrical conductivity for the Ba_2ZnP_2 compound. According to **Fig. 2.4**, one can note the main feature, it is the strong hybridization between the Zn and P states in mostly valence bands, signifying the high covalency of the Zn-P chemical bond as mentioned above in the structural properties section. On the other hand, apart the weak overlapping in the V_1, the PDOS of the Ba atom is energetically separated from those of the Zn and P atoms, signifying that the chemical bonding between Ba and Zn/P is mostly of ionic character.

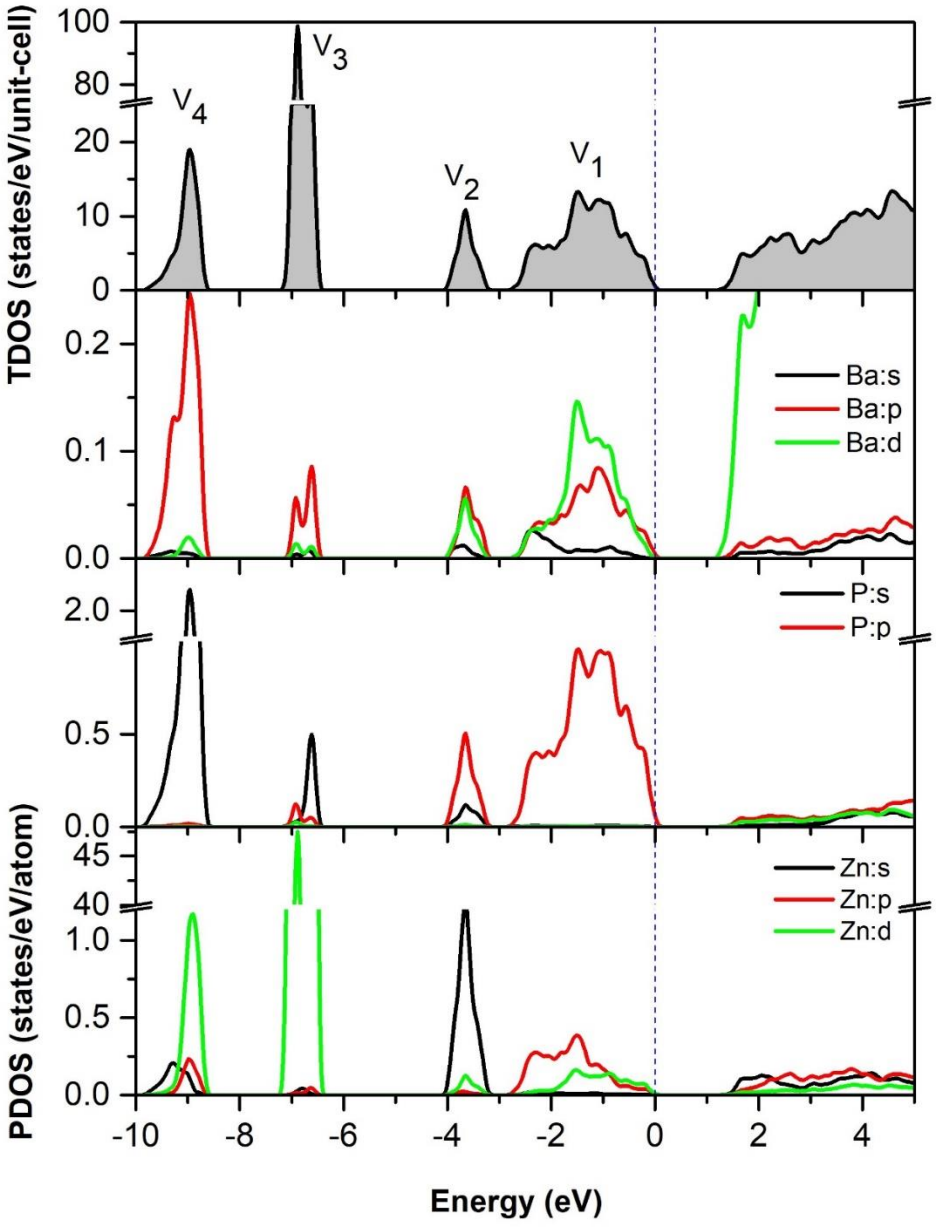

Fig. 2.4: The calculated TDOS and PDOS for Ba_2ZnP_2. The Fermi level is at zero.

The Zn-P interaction must be considered as an intermediate mixed interaction with a polar-covalent character as it can be seen in **Fig. 2.5**.

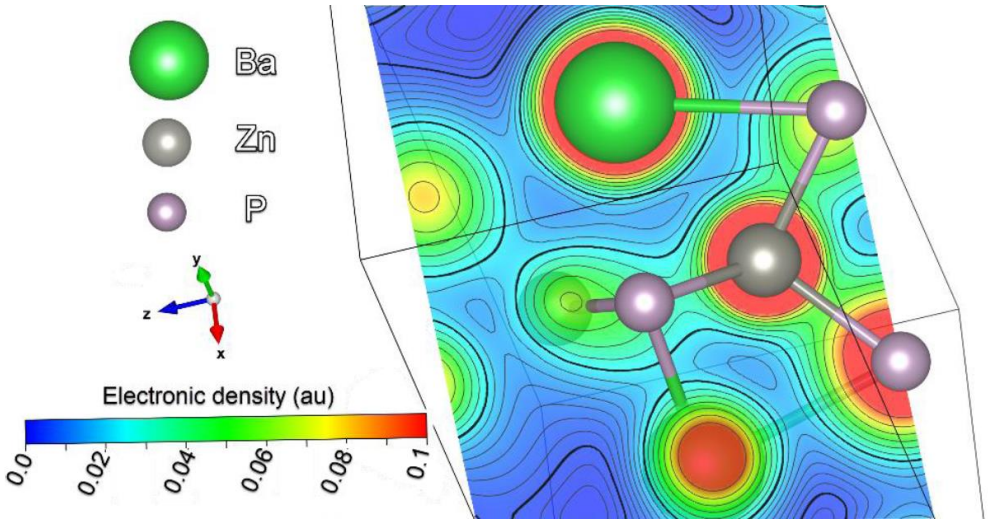

Fig. 2.5: Contours map of the electronic density showing the partially covalent character of the Zn-P bond and the dominantly ionic nature of the Ba-P bond, using the QTAIM as implemented in the CRITIC2 software.

2.2.3 Elastic properties

2.2.3.1 Monocrystalline elastic constants C_{ij}s

Monocrystalline and polycrystalline elastic moduli of solids quantify their responses to applied external deformations within the elastic limit. Therefore, elastic moduli are closely related to a number of fundamental physical properties of solids, such as mechanical properties, structural stability, sound velocity, bonding forces between neighboring atoms, nature and strength of chemical bond, machinability, anisotropy, lattice dynamics, thermoelectricity and thermodynamic properties. Thus, determination of the elastic moduli of solids is of great importance from basic and applied perspectives. The calculated elastic constant in single-crystal at orthorhombic phase were described by twenty-one independent elastic constants C_{ij}s (and their elastic compliances S_{ij}s), with considerable values of nine independent elastic constants, labeled C_{11}, C_{12}, C_{13}, C_{22}, C_{23}, C_{33}, C_{44}, C_{55} and C_{66}. Our calculated elastic constants C_{ij} of Ba_2ZnP_2 are presented in **Table 2.5**. Until now no experimental or theoretical data interest to study the elastic constants of the title compound. According to **Table 2.5**. we can make the following conclusions:

a) The C_{11}, C_{22} and C_{33} elastic constants illustrate the stiffness stress lengthways the crystallographic a, b and c axes, respectively. For the studied compound, the $C_{33} \approx C_{22} > C_{11}$.

The Ba_2ZnP_2 compound appeared large resistant to versus the external stress along the [001] and [010] crystallographic direction comparing that along the other directions [100]. As can be again attributed to the more robust bonds that along the crystallographic z-axis. The shear modulus of the (100), (010) and (001) planes represented by the C_{44}, C_{55} and C_{66} elastic constants, respectively. The latter are comparatively little than the C_{11}, C_{22} and C_{33}, demonstrating that this compound is less resistance to shear deformation than compression. This evidences that the linear compressibility (β) will be almost isotropic.

b) The computed elastic constants of the studied compounds satisfy the conditions of Born and Huang mechanical stability criteria [17,18]:
$C_{11}>0$, $C_{22}>0$, $C_{33}>0$, $C_{44}>0$, $C_{55}>0$, $C_{66}>0$, $C_{11}+C_{22}-2C_{12}>0$, $C_{11}+C_{33}-2C_{13}>0$, $C_{22}+C_{33}-2C_{23}>0$, $C_{11}+C_{22}+C_{33}+2(C_{12}+C_{13}+C_{23})>0$. This suggests the mechanical stability of title compound.

Table 2.5: Calculated elastic constant C_{ij} (in GPa) for the orthorhombic Zintl phase Ba_2ZnP_2 compound.

	C_{11}	C_{12}	C_{13}	C_{22}	C_{23}	C_{33}	C_{44}	C_{55}	C_{66}
Ba_2ZnP_2	83.9	27.7	26.9	93.6	18.1	93.8	17.4	25.7	22.1

2.2.3.2 Elastic wave velocities

There are some important physical properties of the material (such as thermal conductivity) closely related with the sound velocity in a crystal. The single-crystal elastic wave velocities in different directions ([100], [010] and [001]) can be estimate using Christoffel equation [19] and procedure of Brugger [20] in an orthorhombic system, the pure longitudinal (L) and transverse (T) wave velocities propagating are given by the following expressions [21]:

$$\begin{aligned} &v_L^{[100]} = (C_{11}/\rho)^{1/2}, v_{T_1}^{[100]} = (C_{66}/\rho)^{1/2}, v_{T_2}^{[100]} = (C_{55}/\rho)^{1/2} \\ &v_L^{[010]} = (C_{22}/\rho)^{1/2}, v_{T_1}^{[010]} = (C_{66}/\rho)^{1/2}, v_{T_2}^{[010]} = (C_{44}/\rho)^{1/2} \\ &v_L^{[001]} = (C_{33}/\rho)^{1/2}, v_{T_1}^{[001]} = (C_{55}/\rho)^{1/2}, v_{T_2}^{[001]} = (C_{44}/\rho)^{1/2} \end{aligned} \quad (2.5)$$

In this context, ρ is the mass density of the propagating medium. The calculated elastic wave velocities along [100], [001] and [110] directions are listed in **Table 2.6**. From this latter, one

can see that the transverse wave velocities are less than the longitudinal ones, where its values less than 4500 m/s. This can be explained by the fact that the measuring of C_{44}, C_{55} and C_{66}, are smaller than those measuring of C_{11}, C_{22} and C_{33}. Also, the table illustrates also that the sound velocities are anisotropic.

Table 2.6: Longitudinal and transverse acoustic wave velocities (v_L and v_T, in *m/s*) in different crystallography directions for considered compound within their density ρ= 4.83.

	$v_L^{[100]}$	$v_L^{[010]}$	$v_L^{[001]}$	$v_{T_1}^{[100]}$	$v_{T_1}^{[010]}$	$v_{T_1}^{[001]}$	$v_{T_2}^{[100]}$	$v_{T_2}^{[010]}$	$v_{T_2}^{[001]}$
Ba_2ZnP_2	4167.8	4402.1	4046.8	2139.1	2139.1	2306.7	2306.7	1898.0	1898.0

2.2.3.3 Elastic anisotropy

It is well-known that the elastic anisotropy extent of a great important in materials and engineering sciences as well as physical crystallography point of view, also it affects the stability, dislocations of materials and the elastic anisotropy reflects different bonding natures in different crystallographic directions. Evaluation of the elastic anisotropy is necessary to understand the microcracks in solids [22] and its effect at the nanoscale precursor textures in alloys [23]. So, there are several criterium to investigate the elastic anisotropy for example: universal index [24], shear anisotropic factors [25], the percentage anisotropy in compressibility and shear [26], The scalar log-Euclidean anisotropy index [27] and 3D representation of elastic moduli. We present two different approaches ways to evaluate the elastic anisotropic read:

First, universal index A^U has been proposed by Ranganathan and Ostoja-Starzewski [24], which is defined as follows:

$$A^U = 5\frac{G_V}{G_R} + \frac{B_V}{B_R} - 6 \quad (2.6)$$

where *B* and *G* represent the bulk and the shear modulus, the subscripts V and R denote Voigt and Reuss approximations, respectively. The isotropic crystals are characterized by universal index equal to zero (A^U= 0), so, any deviation from this value means that the extent of anisotropy crystals, can be measuring its degree. Calculated value of A^U for Ba_2ZnP_2 is equal to 0.35, denoting that is Ba_2ZnP_2 characterized by a noticeable elastic anisotropy.

Second, evaluation the elastic anisotropy in a material is by representation 3D of the crystallographic directions dependence of its elastic moduli (Young's modulus and bulk's modulus), In a 3D plotting, the exhibition a spherical shape means an isotropic system, and the aberration from a spherical shape denotes the degree of anisotropy. Representation of the 3D-closed surface for the crystallographic direction dependence of the young's modulus E and compressibility β of an orthorhombic crystal are expressed by the following well-known relations [28]:

$$1/E = l_1^4 S_{11} + 2l_1^2 l_2^2 S_{12} + 2l_1^2 l_3^2 S_{13} + l_2^4 S_{22} + 2l_2^2 l_3^2 S_{23} + l_3^4 S_{33} + l_2^2 l_3^2 S_{44} + l_1^2 l_3^2 S_{55} + l_1^2 l_2^2 S_{66} \quad (2.7)$$

$$\beta = 1/B = (S_{11} + S_{12} + S_{13})l_1^2 + (S_{12} + S_{22} + S_{23})l_2^2 + (S_{33} + S_{23} + S_{13})l_3^2 \quad (2.8)$$

Where, l_1, l_2 and l_3 are the direction cosines coordinates with respect to X, Y and Z axes respectively, which show the angles between these axes, and S_{ij} are the elastic compliances constants.

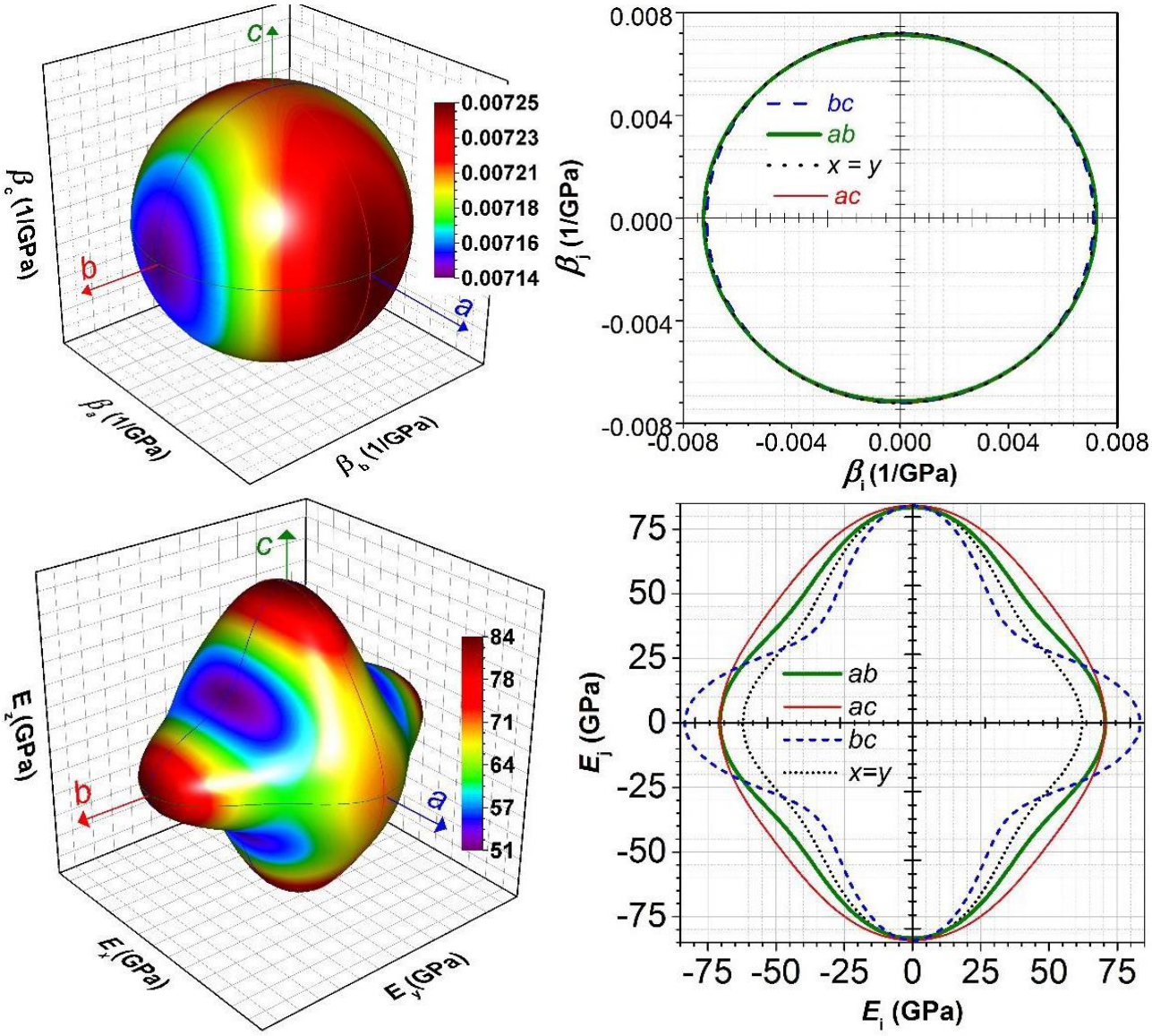

Fig. 2.6: 3D-representations of the crystal direction dependence of the Young's modulus (*E*, in GPa) and linear compressibility (*β*, in GPa^{-1}) and their cross-sections in the (*xy; ab*), (*xz; ac*), (*yz; bc*) and (*x = y*) planes for Ba_2ZnP_2.

Computed 3D-closed surface and their central cross sections in the YZ, XZ and XY planes of the Young's modulus and bulk's modulus for Ba_2ZnP_2 are shown in **Fig. 2.6**. From these illustration 3D and its central cross sections for the considered compound of young's modulus E, one can see that deviate largely from the spherical shape and circular form, respectively, demonstrating a noticeable directional dependence, while from bulk's modulus, evidencing that this compound is characterized by a feeble elastic anisotropy. The minimum value of *E* is equal to 51 GPa along the [011] direction and the maximum value is equal to 84 GPa along the [001] direction. Thus, the relative difference between the E_{max} and E_{min} is approximately equal 52% of the isotropic value of *E* (~64.5 GPa). The minimum value of *β* is

equal to 7.13×10^{-3} GPa^{-1} along the [100] direction and the maximum value is equal to 7.25×10^{-3} GPa^{-1} along the [010].

2.2.3.4 Polycrystalline aggregate elastic moduli

In polycrystalline system, there are the several grains has some structure, but could affect relative elastic properties, therefore we have to resort to hypotheses such isostress of Voigt [29], isostrain Reuss[30] and Hill approximations [31], which bulk 's modulus B and shear's modulus G in recent approximations defined by following express:

$$1/B_R = (S_{11}+S_{22}+S_{33}) + 2(S_{12}+S_{13}+S_{23}) \quad (2.9)$$

$$1/G_R = [4(S_{11}+S_{22}+S_{33}) - 4(S_{12}+S_{13}+S_{23}) + 3(S_{44}+S_{55}+S_{66})]/15 \quad (2.10)$$

$$B_V = (C_{11}+C_{22}+C_{33}+2[C_{12}+C_{13}+C_{23}])/9 \quad (2.11)$$

$$G_V = (C_{11}+C_{22}+C_{33}+3[C_{44}+C_{55}+C_{66}]-[C_{12}+C_{13}+C_{23}])/15 \quad (2.12)$$

Here*: S_{ij} (C_{ij})* is the elastic compliances (stiffness) constants, where $S_{ij} = 1/C_{ij}$.

Hill proved that the effective values is equal to the arithmetic mean between bulk and shear moduli:

$$B_H = (B_R + B_V)/2 \quad (2.13) \quad \text{and} \quad G_H = (G_R + G_V)/2 \quad (2.14)$$

Young's modulus (E), Poisson ratio's σ [32], average longitudinal v_l, transverse v_T elastic wave velocities, the average wave velocity v_m [33] and Debye temperature T_D [34] in polycrystalline structure can be computed from the following expressions:

$$E = 9BG/(3B+G) \quad (2.15) \quad \text{and} \quad \sigma = (3B-2G)/(6B+2G) \quad (2.16)$$

$$v_l = [(3B_H + 4G_H)/(3\rho)]^{1/2} \quad (2.17) \quad \text{and} \quad v_T = [G_H/\rho]^{1/2} \quad (2.18)$$

$$v_m = [(1/v_l^3 + 2/v_T^3)/3]^{-1/3} \quad (2.19) \quad \text{and} \quad T_D = (h/K_B)[3nN_A\rho/(4\pi M)]^{1/3} v_m \quad (2.20)$$

Where: ρ is the mass density, n is the number of atoms in the molecule, N_A is Avogadro number, M is the molecular weight, h and K_B are Planck and Boltzmann constants, respectively. Employing the aforementioned relations, the obtained results are listed in **Table 2.7**, which let us to make some conclusions:

a) There is well-known relationship between the elastic moduli (bulk and shear) and the elastic properties of polycrystalline pure metals, Pugh's ratio empirical criterion [35], which provide information concerning the brittle-ductile nature of a material, if B/G >1.75 denotes the ductile nature of the material; otherwise, it is brittle. The computed B/G ratio values registered in **Table 2.7**, this result indicating the ductile nature of the considered compound. Brittle materials are fragile to thermal shocks [36].

b) Debye temperature T_D is correlated with several important physical properties of solids, such as heat capacity value, thermal expansion, melting temperature, so on. As a rule, when T_D increase, thermal conductivity and melting temperature increase [36], as well as, it can be used to separate between high- and low-temperature regions for a solid. Debye temperature T_D was calculated by relationship mentioned above [34]. The value of T_D dependence Ba_2ZnP_2 is listed in **Table 2.7**.

c) The determined of chemical bonding nature can be by the use of Poisson's ratio σ and comparison between shear G and bulk B moduli, in order for chemical bonding to be covalent, G must be small comparing, A typical value of σ for covalent bonding is 0.1 and G/B= 24/22; for ionic bonding σ is typically 0.25 and G/B= 6/10; finally, for metallic bonding σ is 0.33 and G/B= 3/8; in the extreme case where σ is 0.5 and G is zero [20]. One shows that the values of the σ is equal almost 0.27. So, we suggest that the chemical bonding in Ba_2ZnP_2 has a dominant ionic character.

d) The predicted values for the *B, G* and *E* moduli are moderate, evidencing the moderate resistance of Ba_2ZnP_2 against averaged volume change, shearing deformation and unidirectional compression/attraction.

e) The *B* value is almost double that of *G*, indicating that Ba_2ZnP_2 is more resistant to change in volume than to change in shape and therefore *G* is the decisive modulus of elasticity affecting the mechanical stability of Ba_2ZnP_2.

Table 2.7: Calculated Reuss, Voigt and Hill bulk (B, in GPa), shear's modulus (G, in GPa), Young's modulus (E, in GPa) and Poisson's ratio (σ, dimensionless), Pugh ratio B_H/G_H, average sound velocities (v_m, in m/s) and Debye temperature (T_D, in K) for polycrystalline Ba_2ZnP_2 compound. The subscript V, R and H stand to the Voigt, Reuss and Hill.

	Theory	**B**	**G**	**E**	**σ**	**B/G**	v_m	**T_D**
Ba_2ZnP_2	***V***	46.31	26.27	66.28	0.26	1.82	2542	250.0
	R	46.31	24.58	62.67	0.27			
	H	46.31	25.43	64.48	0.27			

2.2.4 Optical properties

The Ba_2ZnP_2 compound has an orthorhombic symmetry. Thus, the consequent dielectric functions are $\varepsilon^{xx}(\omega)$, $\varepsilon^{yy}(\omega)$ and $\varepsilon^{zz}(\omega)$. These latter correspond to incident radiation in an electrical field polarized parallel along three axes dependents (x, y and z), respectively. The optical properties may be concluded from the imaginary part $\varepsilon_2(\omega)$ and the real part $\varepsilon_1(\omega)$ of the complex dielectric function $\varepsilon(\omega) = \varepsilon_1(\omega) + i\,\varepsilon_2(\omega)$. The linear optical response of the medium is characterized by the dielectric function $\varepsilon(\omega)$. The intraband and interband transitions are contributions to $\varepsilon(\omega)$, but the first is important for metals, where $\varepsilon_2(\omega)$ explains the absorbed energy, and it is computed from the matrix elements dependent valence band and the conduction band use well-known relationship [37,38], while the real part $\varepsilon_1(\omega)$ describes the incident radiation, it can be calculated from $\varepsilon_2(\omega)$ within the Kramers–Kronig transformation [39]. According the PDOS diagrams depicted in **Fig. 2.4**, one can assign the observed structure in $\varepsilon_2(\omega)$ spectrum to electronic transitions from the V_1, V_2, V_3 and V_4 valence bands to the CBM band, i.e., transitions from the occupied P-3p and Zn-4s states to the unfilled Ba-5d states. The computed components of the imaginary and real parts of the dielectric tensor for the studied compound are display in **Fig. 2.7** in a wide range of energy, 0-30 eV. We see the spectra of components (ε^{xx}, ε^{yy} and ε^{zz}) of the imaginary and real parts exhibit main peaks with almost the same position for title compound and it appear a considerable anisotropy. There are two main peaks in imaginary part of incident radiation ranging 0-15 eV along three crystallography directions for Ba_2ZnP_2 compound listed in **Table 2.8**. The magnitude of the structure corresponding to ε^{zz} is slightly larger than those corresponding to ε^{xx} and ε^{yy}. It exhibits a well distinct anisotropy in the energy range 0-20 eV and it is nearly isotropic in the rest energy range for considered compound.

Table 2.8: Determined the main peak positions dependent components (ε^{xx}, ε^{yy} and ε^{zz}) of the imaginary part for Ba_2ZnP_2 compound.

Direction	**xx**		**yy**		**zz**	
Peak positions	**E_1**	**E_2**	**E_1**	**E_2**	**E_1**	**E_2**
Ba_2ZnP_2	4.5	10.9	4.6	11.0	4.1	11.3

The real part of dielectric function is considered importance parameter, from **Fig. 2.7** shown an obvious anisotropy, especially along z-axis and the magnitude of ε^{zz} curve equal to 11.8 at 2.1 eV, and it is somewhat greater than those of ε^{xx} and ε^{yy}, it can also be note $\varepsilon_1(\omega)$

to reach a maximum at ~2.1 eV then starts to decrease, where the real part of dielectric function has negative values ranging ~5 eV to ~10 eV and ~18 eV to ~22 eV, which correspond to metallic behavior. There are many features of materials science dependence of the static dielectric constant $\varepsilon_1(0)$ such as measuring of optical anisotropy, this latter is the real parts at low energy limit. According Penn model [40]:

$$\varepsilon_1(0) = 1 + (\hbar\omega_p / E_g)^2[1 - (E_g / 4E_F) + (E_g / 4E_F)^2 / 3] \quad (2.21)$$

Where $\hbar\omega_p$ is the plasma energy, within neglecting the small quantity E_g / E_F, the values of static dielectric constants for Ba_2ZnP_2 along three direction crystallography (x-, y- and z-axes) are represented in **Table 2.9**. We note the inversely proportional relationship between the band gap Eg and $\varepsilon_1(0)$. Using $\varepsilon_1(\omega)$ and $\varepsilon_2(\omega)$ well-known relationships could be calculate the absorption coefficient $\alpha(\omega)$, optical conductivity $\Sigma(\omega)$, electron energy-loss function $L(\omega)$, reflectivity $R(\omega)$, refraction index $n(\omega)$ and extinction coefficient $k(\omega)$, these parameters are display in **Fig. 2.7**.

Table 2.9: Calculated static anisotropy A_{OPT} based on the static refractive index $n(0)$ and the static dielectric constants $\varepsilon_1(0)$ for Ba_2ZnP_2 compound along x-, y-, z-axes.

	Direction	$n(0)$	$R(0)(\%)$	Δn	$\varepsilon_1(0)$	A_{OPT}
Ba_2ZnP_2	**xx**	2.79	22.3	-0.17	7.78	0.93
	yy	2.81	22.6	0.19	7.90	0.95
	zz	2.98	24.7	-0.02	8.86	1.13

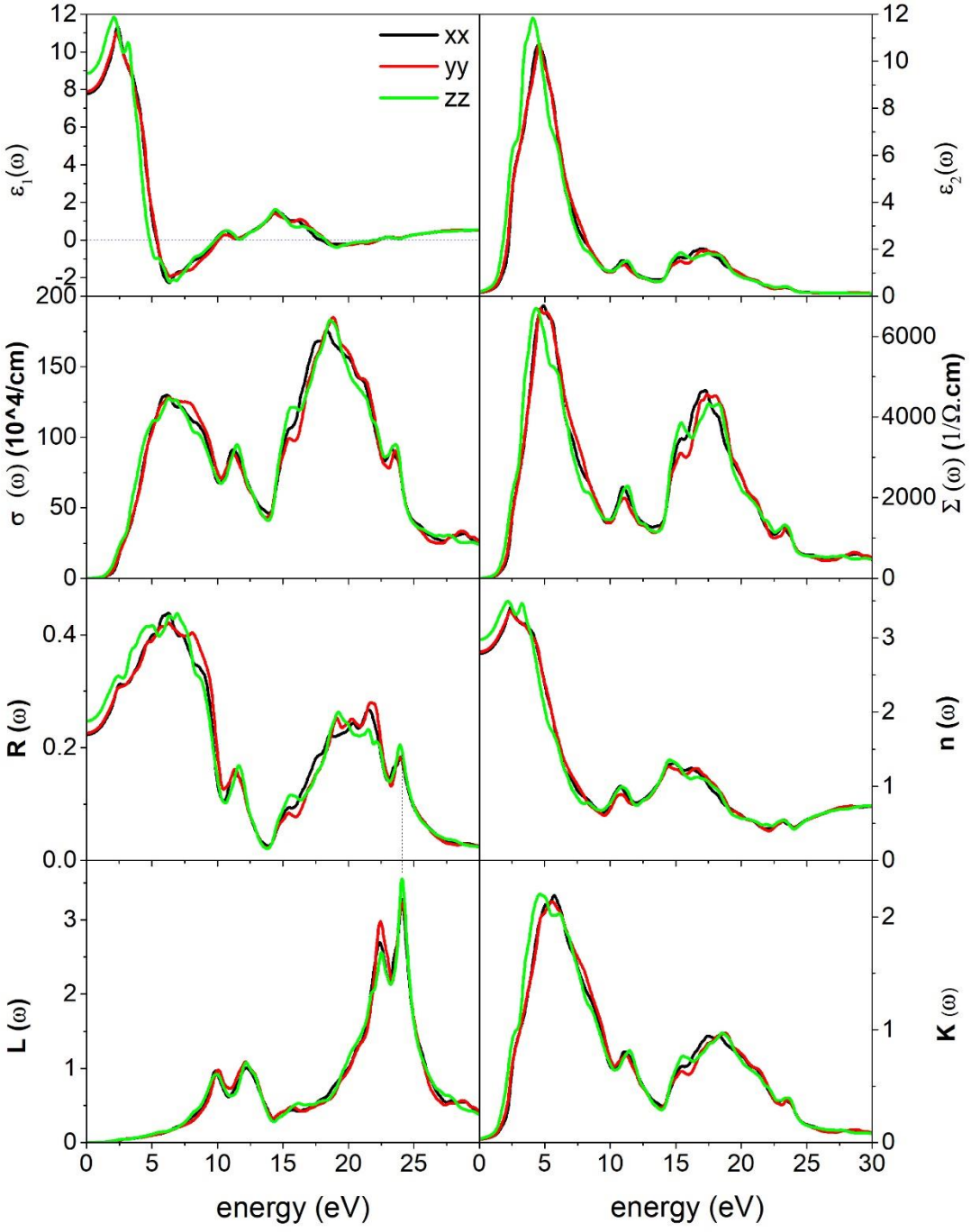

Fig. 2.7: Real and imaginary parts, absorption coefficient α(ω), optical conductivity Σ (ω) electron energy-loss function L(ω), reflectivity R(ω), refraction index n(ω) and extinction coefficient k(ω) of the dielectric function for Ba_2ZnP_2 compound of incident radiations polarized along x-, y- and z-axes directions.

We can conclude the following:

a) The absorption spectrum is extends horizontally forward starting from 1.3 eV up to 30 eV, this start corresponding to the energy indirect gap. In the semiconductors, typically, when the photon energy is increases the absorption coefficient α(ω) rises rapidly as is the case with our system. the Ba_2ZnP_2 compound has a band gap about 1.24 eV may absorb the infrared rays of the invisible field, we can see that the considered compound is characterized by a high optical absorption ($>10^6$ cm^{-1}) in two wide optical structures lying in the energy range ~5 to ~9 eV with threshold exceeding 125×10^4 cm^{-1} and ~16 to ~22 eV with threshold exceeding 180×10^4 cm^{-1}. Also, the absorption coefficient is very close to the optimum band gap for the solar cell absorbers (1.4 eV), and the title compound have a high absorptivity with direct proportion of the electromagnetic wave in the visible spectrum (1.6 to 3.1 eV) and Near-UV region (3.1 to 6.0 eV), suggests that this compound is possible candidates for optoelectronic applications in the aforementioned energy ranges.

b) The reflectivity coefficient R (ω) of Ba_2ZnP_2 is plotted in **Fig. 2.7**. which is characterized by an average its values, where it reaches approximately ~ 44% for a photon energy equal to ~6.9 eV. Whereas the static reflectivity coefficient R (0) has a value for a maximum of 25% along [001] direction. The magnitude of $R(\omega)$ along [001] is higher than [100] and [010] directions, viz. it exhibits obvious anisotropy.

c) For describing of the energy loss of a fast electron traversing in a material, the spectrum of the electron energy loss function L(w) is depicted in **Fig. 2.7**. Where the primary peak location is usually associated with the plasma frequency [36]. One can see that the L(w) peaks is at edges in the reflection spectrum centered at 9.97, 12.17, 22.44 and 24.06 eV correspond to the abrupt decreases of the reflection spectrum.

d) The refractive index is interesting parameter in optoelectronic devices. **Fig. 2.7** represents the refractive index n(ω) for three different orientations in an extensive spectral region reaches to 30 eV. We note at the lower energy limit that n(0) (the static refractive index) value for Ba_2ZnP_2 is listed in **Table 2.9**. As we see the refractive index increases in about the 0 to ~ 2.5 eV energy range, after that it decreases, where the n(ω) maximum value of title compound exceeds 3.49 at photon energy of approximately to 2.2 eV along [001] direction, While the extinction coefficient k(ω) reaches its maximum (around 2.2) almost at 4.6 eV for studied compound. From **Fig. 2.7**, the title compound and their optical properties exhibit a noticeable

anisotropy. As can be determined an important parameter, static anisotropy, reflecting the photonic response through the material crystallographic orientations. The static anisotropy expressed as follows [41]:

$$A_{OPT} = \left[\frac{n(0)^{[dir]}}{n(0)^{[poly]}}, \frac{\varepsilon_1(0)^{[dir]}}{\varepsilon_1(0)^{[poly]}} \right] \quad (2.22)$$

Here, $n(0)^{[dir]}$ $\varepsilon_1(0)^{[dir]}$ are the value of along x-, y- and z-axes, $n(0)^{[poly]}$ $\varepsilon_1(0)^{[poly]}$ are its values in polycrystalline. A material is optically isotropic if $A_{OPT}= 1$, otherwise, it is optically anisotropic. The degree of deviation of A_{OPT} from unity reveal the extent of the optical anisotropy. The values of A_{OPT} are listed in **Table 2.9**. Also, this table contains the calculated values of the birefringence at zero frequency for the Ba_2ZnP_2 along [100], [010] and [001] directions by well-known relationships [42], where the birefringence along one axis equal to the difference between the static refractive index of the other axes within respecting of positive direction of the axes. According this table, the studied compound exhibits a sure optical anisotropy, particularly with regard to z-axis.

2.2.5 Thermoelectric properties

2.2.5.1 Relaxation time and lattice thermal conductivity

Seebeck's effect [43] and Peltier's effect [44] phenomena are caused by convert between heat and electricity such as generator and cooling (refrigerator) applications, respectively. For thermoelectric materials with highly efficient, figure of merit *ZT* (dimensionless parameter) has large values and has no limit to it value [45]. Figure of merit defined as:

$$ZT = S^2 \sigma T / k \quad (2.23)$$

Where *S* is Seebeck coefficient or thermopower, σ is the electrical conductivity ($PF= S^2\sigma$ is called power factor), *T* is the absolute temperature, $k=k_e+k_l$ thermal conductivity, k_e is the electronic thermal conductivity and k_l is the lattice thermal conductivity, as k_l is frequently calculated experimentally as the difference between *k* and k_e from Wiedemann–Franz equation: $k_e=L\sigma T$, where *L* is the Lorenz factor: 2.4×10^{-8} $J^2.K^{-2}.C^{-2}$ for free electrons [46]. The anisotropic charge-carrier relaxation time τ is one of the main physical parameters that

control the transport properties of solid materials, determination of relaxation time based on Bardeen and Shockley's deformation potential (DP) theory [47]:

$$\tau_i = 2(2\pi)^{1/2} C_i \hbar^4 / (3(m_i^* K_B T)^{3/2} E_i^2) \quad (2.24)$$

Where: C_i, $\hbar$, m_i*, K_B, T and Ei are the elastic constant, reduced Planck's constant, the charge-carrier effective mass, Boltzmann's constant, absolute temperature and the 3D deformation potential constant $(Ei = (e_{CBM`VBM`} - e_{core}) / (\Delta i / i_0))$, respectively.

where Δi is a slight deformation of lattice parameter i in a direction, i_0 is the equilibrium value of i, and $e_{CBM`VBM`} - e_{core}$ is the energy change of the CBM (VBM) for electrons (holes). Energy of the deep core state is assumed to be insensitive to the slight lattice deformations and thus it is considered as the reference energy. A series of lattice constants (0.96i_0, 0.98 i_0, i_0, 1.02 i_0 and 1.04 i_0) were considered to calculate the DPs along the *a*, *b* and *c* directions. The average relaxation time (τ_m) is defined as $\tau_m = (\tau_a + \tau_b + \tau_c) / 3$. The variation of τ_m as function of temperature is depicted in **Fig. 2.9**. It is obvious from **Fig. 2.9** that the relaxation time decreases with increasing temperature.

Also, using Slack's relationship [48], can be estimating the lattice thermal conductivity of the title compound in this regime discussed and at temperatures not too far removed from the Debye temperature of the solid, we considered it for our purposes as approximate expressions for the thermal conductivity:

$$K_l = BMV^{1/3} T_D^{\ 3} / (n^{2/3} \gamma^2 T) \quad (2.25)$$

Where: M, V, n, T, γ and T_D are the average atomic mass, the volume per atom (in m^3 unit), the number of atoms in the primitive unit cell, the absolute temperature, the dimensionless acoustic Grüneisen parameter (calculated from thermodynamic properties) and the acoustic Debye temperature. For the lattice thermal conductivity, $B = 2.43 \times 10^4 (1 - 0.514/\gamma + 0.228/\gamma^2)$ (in W/m.K unit).

For the minimum lattice thermal conductivity, $k_{l.min}$ can be calculated by Cahill's model [49]:

$$K_{l.\min} = \tfrac{1}{2} (\pi/6)^{1/3} K_B V^{-2/3} (2v_T + v_L) \quad (2.26)$$

Where: K_B, V, v_T and v_L are Boltzmann's constant, the volume per atom (in m^3 unit), shear and longitudinal sound velocities. The graphs which explain temperature dependence of the average relaxation times, the lattice thermal conductivity and its minimal value are plotted in **Fig. 2.9**. So, the field of thermoelectric materials is needing research focused on minimizing the thermal conductivity and large power factor. The transport properties of Ba_2ZnP_2 compound were estimated based on the calculated mBJ-GGA electronic structure using the Boltzmann theory [50] as executed in the BoltzTraP code [11]. The Seebeck coefficient (S) of holes and electrons in a non-degenerate semiconductor with parabolic bands are [51,52]:

$$S_h = \frac{k_0}{e}\left[\ln\left(\frac{N_V}{p}\right) + 2.5 - r\right] \quad (2.27) \qquad \text{and} \qquad S_e = -\frac{k_0}{e}\left[\ln\left(\frac{N_C}{n}\right) + 2.5 - r\right] \quad (2.28)$$

Where: r, S_h, S_e, N_V, N, c, n and P are the scattering mechanism parameter, the valence band, the effective density of states in conduction band, the number of electron carriers, and the number of hole carriers, respectively.

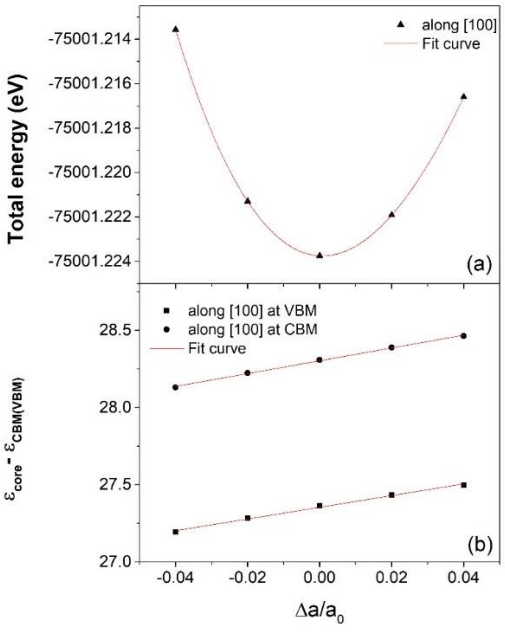

Fig. 2.8: (a) Total primitive cell energy versus lattice dilation strain $\Delta a/a_0$ and (b) band energy of VBM (CBM) with respect to core level (ε_{core}) versus lattice dilation strain $\Delta a/a_0$. The red lines are the fitting curves.

For mixed and degenerate semiconductors, the combined Seebeck coefficient is given by [52,53]:

$$S = \frac{S_e\sigma_e + S_h\sigma_h}{\sigma_e + \sigma_h} \quad (2.29) \qquad \text{and} \qquad S = m^*_{DOS} T \frac{8}{3e}\left(\frac{\pi k_B}{h}\right)^2 \left(\frac{\pi}{3n}\right)^{2/3} \quad (2.30)$$

Where: K_B is the Boltzmann constant, T is the temperature, n is the carrier concentration and m^*_{DOS} is the density of states effective mass, it is given by:

$$m^*_{DOS} = (m^*_{xx} m^*_{yy} m^*_{zz})^{1/3} N_V^{2/3} \quad (2.31)$$

Where: m^*_{xx}, m^*_{yy} and m^*_{zz} are the band effective mass components along Γ-X, Γ-Y and Γ-Z, respectively, and N_V is the band degeneracy.

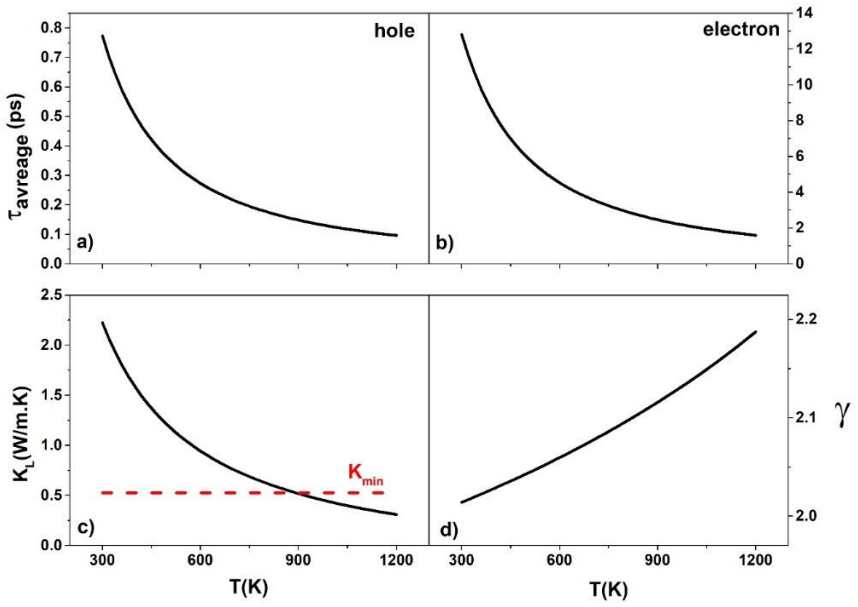

Fig. 2.9: The calculated average relaxation times τ_h, τ_e and Grüneisen parameter γ, the lattice thermal conductivity K_l versus temperature. The red solid line notes the minimal lattice thermal conductivity K_{min}.

The calculated the electrical conductivity (σ), thermal conductivity (κ), power factor ($PF=S^2\sigma$), Seebeck coefficient (S), the thermoelectric figure of merit (ZT) as a function of charge-carrier concentration between 10^{18} cm^{-3} and 10^{21} cm^{-3} aimed at better thermoelectric performance [36], [46] for both the *n*-type and *p*-type doped studied compound at 300, 600, 900 and 1200 K are shown in **Fig. 2.10**.

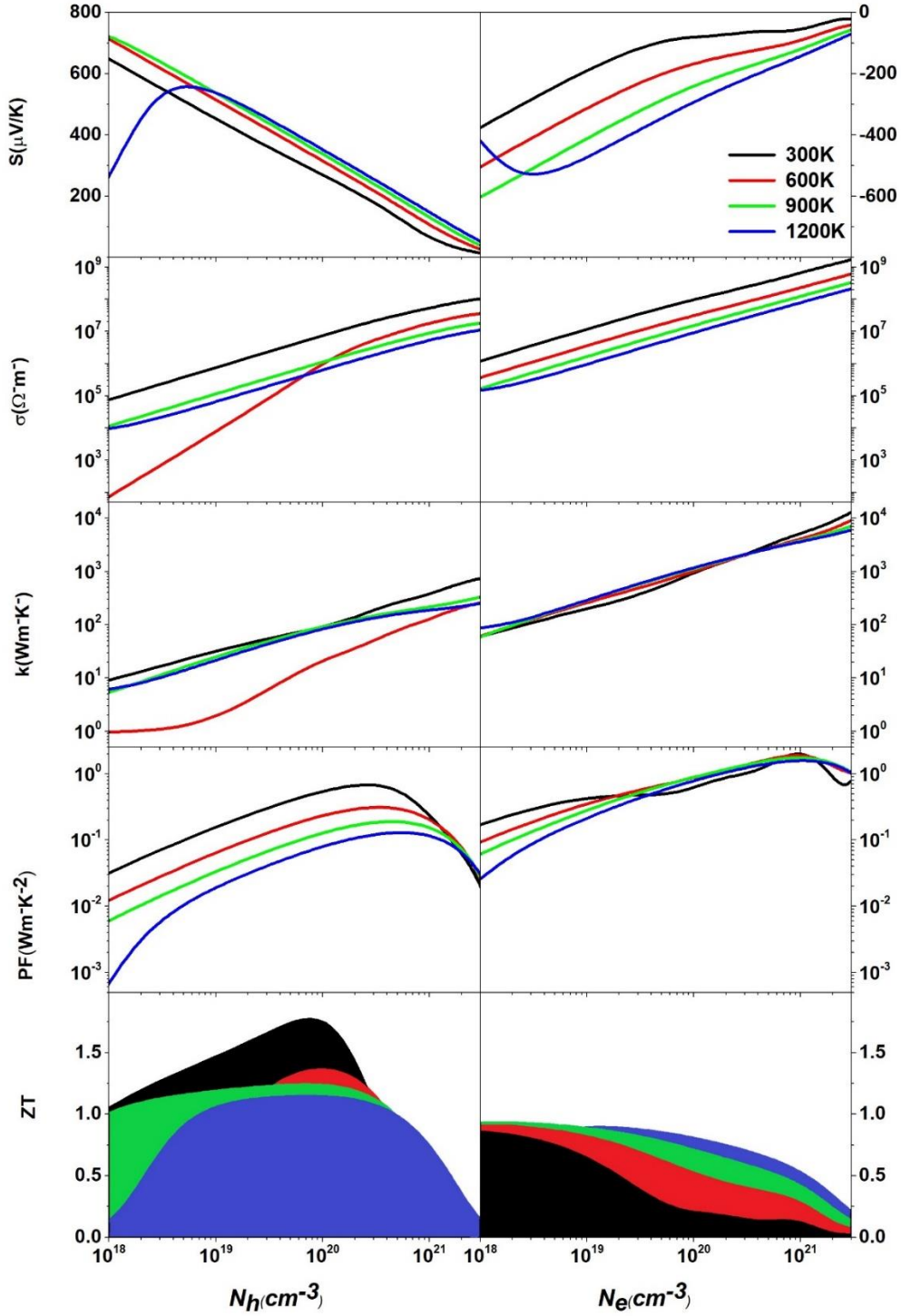

Fig. 2.10: Transport coefficients of the Seebeck coefficient (S), electrical conductivity (σ), thermal conductivity (K), power factor (PF=$S^2\sigma$) and figure of merit (ZT) as a function of carrier concentration 10^{18} cm^{-3} and 10^{21} cm^{-3} for the *n*-type and *p*-type doped Ba_2ZnP_2 compound at 300, 600, 900 and 1200 K.

According to **Fig. 8-10**, we can conclude the following:

a) When the temperature increase, the relaxation time and the lattice thermal conductivity decrease, because of the increasing of the thermal speed of the electrons and the vibration amplitude of atoms around their mean positions. Where the calculated $k_{l,min}$ for Ba_2ZnP_2 is equal to 0.53 W/m.K, which indicates that Ba_2ZnP_2 might be a good thermoelectric material. the presence of heavy atoms and the complexity of the crystal structure (co-existence of ionic and covalent bonds) are the cause of the low value of the lattice thermal [49], [51]. Also, the lattice thermal conductivity within Slack's relationship become smaller than $\kappa_{l,min}$ of Cahill's model afterward ~900K.

b) The extent of Seebeck coefficient is inversely proportional with the carrier concentration for Ba_2ZnP_2 compound *n*-type and *p*-type doping, while the electrical conductivity, the thermal conductivity and the power factor have been directly proportional at the same temperature. There is inverse relationship fairly between electrical conductivity and temperature, i.e., that Ba_2ZnP_2 become has behavior of the conductor at high temperature, because the electrical conductivity at the semiconductors is directly related to the temperature. Seebeck coefficient, the power factor and the thermal conductivity have a directly proportional to the temperature at the same carrier concentration. This is a common trend in the thermoelectric materials.

c) For the Seebeck coefficient efficiency, the effect of *p*-type doping at Ba_2ZnP_2 compound is slightly larger than *n*-type, because the hole effective mass is heavier than the electron effective mass (as shown in **Table 2.4**), for the carrier concentration equal to $10^{18}cm^{-3}$, Seebeck coefficient of *p*-type title compound equal to 720 μV/K at 900K. Meanwhile, Seebeck coefficient of *n*-type studied compound equal to 603 μV/K corresponding to same conditions. We note that electrical conductivity of the *n*-type doped studied compound is large than *p*-type one, these results are expected, because the hole effective mass is heavier than the electron effective mass.

d) As per the variation of ZT as function of carrier concentration, the figure of merit reaches its maximum at deference carrier concentration of both the *n*-type and *p*-type doped investigated compound for 300, 600, 900 and 1200 K. **Table 2.10**, concludes the maximum value of figure of merit at the same temperature and charge-carrier concentration, the maximum of ZT for the *p*-type doped studied compound is greater than that of the *n*-type

doped. The figure of merit ZT reaches a maximum of 1.77 for hole concentration of 8×10^{19} cm^{-3} at 300 K. Also, can note figure of merit is large than 1 next to considering concentration for 300, 600, 900 and 1200 K. while for *n*-type compound, ZT< 1.

Table 2.10: Maximum values of figure of merit at differences temperature and charge-carrier concentration for the *p*-type and *n*-type doped Ba_2ZnP_2 compound.

	Ba_2ZnP_2							
	Hole				**Electron**			
T(K)	1200	900	600	300	1200	900	600	300
ZT	1.15	1.24	1.36	1.77	0.89	0.93	0.93	0.85
cc (cm^{-3})	7.10^{19}	6.10^{19}	1.10^{20}	8.10^{19}	1.10^{19}	1.10^{18}	1.10^{18}	1.10^{18}

Table 2.11: Calculated Seebeck coefficient values at 300 K and charge-carrier concentration of 10^{19} cm^{-3} for Ba_2ZnP_2 compound compared with those of Ba_2ZnSb_2 and Ba_2ZnBi_2 Zintl phases compounds.

	[a] **Ba_2ZnP_2**		[b] **Ba_2ZnSb_2**		[b] **Ba_2ZnBi_2**	
Doping type	***n***	***p***	***n***	***p***	***n***	***p***
S (μV/K)	190	450	~360	~290	~220	~200

[a] Present work.

[b] Ref. [57].

e) The TE quality of compounds regarded as important factors to estimate Seebeck coefficient and figure of merit (ZT), we compared Ba_2ZnP_2 Zintl phase one to Ba_2ZnSb_2 and Ba_2ZnBi_2 [54] are listed in **Table 2.11**.

From this table, we can note the following:

- Generally, Seebeck coefficient of studied compound has the largest values for *p*-type doped.

- Under the same conditions, the values of Seebeck coefficient for Ba_2ZnP_2 is greater than values of the traditional thermoelectric Bi_2Te_3 material (>313 μV/K for the *p*-type and >196 μV/K for the *n*-type [55]).

So, one can propose that the Zintl phase Ba_2ZnP_2 *p*-type as probable candidate for thermoelectric applications, particularly, if one can further reduce their thermal conductivities by alloying, nano-structuring, superlattice growth or other techniques [36].

References

[1] J. P. Perdew *et al.*, "Restoring the Density-Gradient Expansion for Exchange in Solids and Surfaces," *Phys. Rev. Lett.*, vol. 100, no. 13, p. 136406, Apr. 2008, doi: 10.1103/PhysRevLett.100.136406.

[2] S. J. Clark *et al.*, "First principles methods using CASTEP," *Z. Für Krist. - Cryst. Mater.*, vol. 220, no. 5–6, pp. 567–570, May 2005, doi: 10.1524/zkri.220.5.567.65075.

[3] F. Tran and P. Blaha, "Accurate Band Gaps of Semiconductors and Insulators with a Semilocal Exchange-Correlation Potential," *Phys. Rev. Lett.*, vol. 102, no. 22, p. 226401, Jun. 2009, doi: 10.1103/PhysRevLett.102.226401.

[4] D. Koller, F. Tran, and P. Blaha, "Merits and limits of the modified Becke-Johnson exchange potential," *Phys. Rev. B*, vol. 83, no. 19, p. 195134, May 2011, doi: 10.1103/PhysRevB.83.195134.

[5] P. Blaha, K. Schwarz, F. Tran, R. Laskowski, G. K. H. Madsen, and L. D. Marks, "WIEN2k: An APW+lo program for calculating the properties of solids," *J. Chem. Phys.*, vol. 152, no. 7, p. 074101, Feb. 2020, doi: 10.1063/1.5143061.

[6] D. Vanderbilt, "Soft self-consistent pseudopotentials in a generalized eigenvalue formalism," *Phys. Rev. B*, vol. 41, no. 11, pp. 7892–7895, Apr. 1990, doi: 10.1103/PhysRevB.41.7892.

[7] H. J. Monkhorst and J. D. Pack, "Special points for Brillouin-zone integrations," *Phys. Rev. B*, vol. 13, no. 12, pp. 5188–5192, Jun. 1976, doi: 10.1103/PhysRevB.13.5188.

[8] T. H. Fischer and J. Almlof, "General methods for geometry and wave function optimization," *J. Phys. Chem.*, vol. 96, no. 24, pp. 9768–9774, Nov. 1992, doi: 10.1021/j100203a036.

[9] C. Ambrosch-Draxl and J. O. Sofo, "Linear optical properties of solids within the full-potential linearized augmented planewave method," *Comput. Phys. Commun.*, vol. 175, no. 1, pp. 1–14, Jul. 2006, doi: 10.1016/j.cpc.2006.03.005.

[10] S. Z. Karazhanov, P. Ravindran, A. Kjekshus, H. Fjellvag, and B. G. Svensson, "Electronic structure and optical properties of ZnX (X=O, S, Se, Te)," *Phys. Rev. B*, vol. 75, no. 15, p. 155104, Apr. 2007, doi: 10.1103/PhysRevB.75.155104.

[11] G. K. H. Madsen and D. J. Singh, "BoltzTraP. A code for calculating band-structure dependent quantities," *Comput. Phys. Commun.*, vol. 175, no. 1, pp. 67–71, Jul. 2006, doi: 10.1016/j.cpc.2006.03.007.

[12] M. A. Blanco, E. Francisco, and V. Luaña, "GIBBS: isothermal-isobaric thermodynamics of solids from energy curves using a quasi-harmonic Debye model," *Comput. Phys. Commun.*, vol. 158, pp. 57–72, Mar. 2004, doi: 10.1016/j.comphy.2003.12.001.

[13] A. Balvanz, S. Baranets, and S. Bobev, "Synthesis, structural characterization, and electronic structure of the novel Zintl phase Ba_2ZnP_2," *Acta Crystallogr. Sect. C Struct. Chem.*, vol. 76, no. Pt 9, pp. 869–873, Sep. 2020, doi: 10.1107/S2053229620010827.

[14] P. Pichanusakorn and P. Bandaru, "Nanostructured thermoelectrics," *Mater. Sci. Eng. R Rep.*, vol. 67, no. 2–4, pp. 19–63, Jan. 2010, doi: 10.1016/j.mser.2009.10.001.

[15] M. Ya. Rudysh *et al.*, "First-principles analysis of physical properties anisotropy for the Ag_2SiS_3 chalcogenide semiconductor," *J. Alloys Compd.*, vol. 826, p. 154232, Jun. 2020, doi: 10.1016/j.jallcom.2020.154232.

[16] A. Balvanz, J. Qu, S. Baranets, E. Ertekin, P. Gorai, and S. Bobev, "New n-Type Zintl Phases for Thermoelectrics: Discovery, Structural Characterization, and Band Engineering of the Compounds A_2CdP_2 (A = Sr, Ba, Eu)," *Chem. Mater.*, vol. 32, no. 24, pp. 10697–10707, Dec. 2020, doi: 10.1021/acs.chemmater.0c03960.

[17] J. Feng and B. Xiao, "Crystal Structures, Optical Properties, and Effective Mass Tensors of $CH_3NH_3PbX_3$ (X = I and Br) Phases Predicted from HSE06," *J. Phys. Chem. Lett.*, vol. 5, no. 7, pp. 1278–1282, Apr. 2014, doi: 10.1021/jz500480m.

[18] M. Born and K. Huang, *Dynamical Theory of Crystal Lattices*. in Oxford Classic Texts in the Physical Sciences. Oxford, New York: Oxford University Press, 1998.

[19] B. B. Karki, L. Stixrude, S. J. Clark, M. C. Warren, G. J. Ackland, and J. Crain, "Structure and elasticity of MgO at high pressure," *Am. Mineral.*, vol. 82, no. 1–2, pp. 51–60, 1997.

[20] W. Y. Ching, S. Aryal, P. Rulis, and W. Schnick, "Electronic structure and physical properties of the spinel-type phase of BeP${}_{2}$N${}_{4}$ from all-electron density functional calculations," *Phys. Rev. B*, vol. 83, no. 15, p. 155109, Apr. 2011, doi: 10.1103/PhysRevB.83.155109.

[21] A. Bedjaoui, A. Bouhemadou, and S. Bin-Omran, "Structural, elastic and thermodynamic properties of tetragonal and orthorhombic polymorphs of Sr_2GeN_2: an ab initio investigation," *High Press. Res.*, vol. 36, no. 2, pp. 198–219, Apr. 2016, doi: 10.1080/08957959.2016.1167202.

[22] P. Ravindran, L. Fast, P. A. Korzhavyi, B. Johansson, J. Wills, and O. Eriksson, "Density functional theory for calculation of elastic properties of orthorhombic crystals: Application to $TiSi_2$," *J. Appl. Phys.*, vol. 84, no. 9, pp. 4891–4904, Nov. 1998, doi: 10.1063/1.368733.

[23] P. Lloveras, T. Castán, M. Porta, A. Planes, and A. Saxena, "Influence of Elastic Anisotropy on Structural Nanoscale Textures," *Phys. Rev. Lett.*, vol. 100, no. 16, p. 165707, Apr. 2008, doi: 10.1103/PhysRevLett.100.165707.

[24] S. I. Ranganathan and M. Ostoja-Starzewski, "Universal Elastic Anisotropy Index," *Phys. Rev. Lett.*, vol. 101, no. 5, p. 055504, Aug. 2008, doi: 10.1103/PhysRevLett.101.055504.

[25] P. Mao, B. Yu, Z. Liu, F. Wang, and Y. Ju, "First-principles investigation on mechanical, electronic, and thermodynamic properties of Mg2Sr under high pressure," *J. Appl. Phys.*, vol. 117, no. 11, p. 115903, Mar. 2015, doi: 10.1063/1.4915339.

[26] D. H. Chung and W. R. Buessem, "The Elastic Anisotropy of Crystals," *J. Appl. Phys.*, vol. 38, no. 5, pp. 2010–2012, Jun. 2004, doi: 10.1063/1.1709819.

[27] C. M. Kube, "Elastic anisotropy of crystals," *AIP Adv.*, vol. 6, no. 9, p. 095209, Sep. 2016, doi: 10.1063/1.4962996.

[28] J. F. Nye, *Physical Properties of Crystals: Their Representation by Tensors and Matrices*. Oxford, New York: Oxford University Press, 1985.

[29] H. Amamou, B. Ferhat, and A. Bois, "Calculation of the Voigt Function in the Region of Very Small Values of the Parameter <i>a</i> Where the Calculation Is Notoriously Difficult," *Am. J. Anal. Chem.*, vol. 04, no. 12, pp. 725–731, 2013, doi: 10.4236/ajac.2013.412087.

[30] G. Kipkemei Chirchir, W. Mueni Mulwa, and B. Ibrahim Adetunji, "Structural, Electronic and Mechanical Properties of Re Doped $FeMnP_{0.67}A_{0.33}$ (A=Ga and Ge): A DFT Study," *Int. J. Phys.*, vol. 10, no. 1, pp. 70–78, Feb. 2022, doi: 10.12691/ijp-10-1-6.

[31] R. Hill, "The Elastic Behaviour of a Crystalline Aggregate," *Proc. Phys. Soc. Sect. A*, vol. 65, no. 5, p. 349, May 1952, doi: 10.1088/0370-1298/65/5/307.

[32] O. Boudrifa, A. Bouhemadou, Ş. Uğur, R. Khenata, S. Bin-Omran, and Y. Al-Douri, "Structural, electronic, optical and elastic properties of the complex K2PtCl6-structure hydrides $ARuH_6$ (A = Mg, Ca, Sr and Ba): first-principles study," *Philos. Mag.*, vol. 96, no. 22, pp. 2328–2361, Aug. 2016, doi: 10.1080/14786435.2016.1198874.

[33] E. Schreiber, O. L. Anderson, N. Soga, and J. F. Bell, "Elastic Constants and Their Measurement," *J. Appl. Mech.*, vol. 42, no. 3, pp. 747–748, Sep. 1975, doi: 10.1115/1.3423687.

[34] O. L. Anderson, "A simplified method for calculating the debye temperature from elastic constants," *J. Phys. Chem. Solids*, vol. 24, no. 7, pp. 909–917, Jul. 1963, doi: 10.1016/0022-3697(63)90067-2.

[35] S. F. Pugh, "XC2. Relations between the elastic moduli and the plastic properties of polycrystalline pure metals," *Lond. Edinb. Dublin Philos. Mag. J. Sci.*, vol. 45, no. 367, pp. 823–843, Aug. 1954, doi: 10.1080/14786440808520496.

[36] A. Bouhemadou *et al.*, "Electronic, optical, elastic, thermoelectric and thermodynamic properties of the spinel oxides $ZnRh_2O_4$ and $CdRh_2O_4$," *J. Alloys Compd.*, vol. 774, pp. 299–314, Feb. 2019, doi: 10.1016/j.jallcom.2018.09.338.

[37] V. Natarajan *et al.*, "Crystal Growth, Thermal, Mechanical and Optical Properties of a New Organic Nonlinear Optical Material: Ethyl P-Dimethylamino Benzoate (EDMAB)," *J. Miner. Mater. Charact. Eng.*, vol. 10, no. 01, pp. 1–11, 2011, doi: 10.4236/jmmce.2011.101001.

[38] M. Fox, *Optical Properties of Solids*, Second Edition, Second Edition. in Oxford Master Series in Physics. Oxford, New York: Oxford University Press, 2010.

[39] M. Alouani and J. M. Wills, "Calculated optical properties of Si, Ge, and GaAs under hydrostatic pressure," *Phys. Rev. B*, vol. 54, no. 4, pp. 2480–2490, Jul. 1996, doi: 10.1103/PhysRevB.54.2480.

[40] D. R. Penn, "Wave-Number-Dependent Dielectric Function of Semiconductors," *Phys. Rev.*, vol. 128, no. 5, pp. 2093–2097, Dec. 1962, doi: 10.1103/PhysRev.128.2093.

[41] D. Cherrad *et al.*, "Ultra soft pseudo potential investigation of fundamental physical properties of $CaXO_3$ (X=Sn and Hf) distorted perovskites: A reference study to the perfect perovskites," *Phys. B Condens. Matter*, vol. 429, pp. 95–105, Nov. 2013, doi: 10.1016/j.physb.2013.08.002.

[42] S. M. Kauzlarich, S. R. Brown, and G. J. Snyder, "Zintl phases for thermoelectric devices," *Dalton Trans.*, no. 21, pp. 2099–2107, May 2007, doi: 10.1039/B702266B.

[43] T. J. Seebeck, "Magnetic polarization of metals and minerals," *Abh. Dtsch. Akad. Wiss.*, vol. 265, 1823.

[44] J. C. Peltier, "Nouvelle experieces sur la caloricite des courans electrique," *Ann Chim*, vol. 371, 1834.

[45] M. K. Yadav and B. Sanyal, "First principles study of thermoelectric properties of Li-based half-Heusler alloys," *J. Alloys Compd.*, vol. C, no. 622, pp. 388–393, 2015, doi: 10.1016/j.jallcom.2014.10.025.

[46] G. J. Snyder and E. S. Toberer, "Complex thermoelectric materials," *Nat. Mater.*, vol. 7, no. 2, pp. 105–114, Feb. 2008, doi: 10.1038/nmat2090.

[47] J. Bardeen and W. Shockley, "Deformation Potentials and Mobilities in Non-Polar Crystals," *Phys. Rev.*, vol. 80, no. 1, pp. 72–80, Oct. 1950, doi: 10.1103/PhysRev.80.72.

[48] G. A. Slack, "The Thermal Conductivity of Nonmetallic Crystals," vol. 34, pp. 1–71, 1979, doi: 10.1016/S0081-1947(08)60359-8.

[49] D. G. Cahill, S. K. Watson, and R. O. Pohl, "Lower limit to the thermal conductivity of disordered crystals," *Phys. Rev. B*, vol. 46, no. 10, pp. 6131–6140, Sep. 1992, doi: 10.1103/PhysRevB.46.6131.

[50] J.R. Chelikowsky and S.G. Louie. Quantum Theory of Real Materials. Kluwer Press, Amsterdam, 1996.

[51] Y. L. Yan, Y. X. Wang, and G. B. Zhang, "Electronic structure and thermoelectric performance of Zintl compound $Ca_5Ga_2As_6$," *J. Mater. Chem.*, vol. 22, no. 38, pp. 20284–20290, Sep. 2012, doi: 10.1039/C2JM32945J.

[52] M. C. Chen, "A quick thermoelectric technique for typing HgCdTe at liquid nitrogen temperature," *J. Appl. Phys.*, vol. 71, no. 7, pp. 3636–3638, Apr. 1992, doi: 10.1063/1.350926.

[53] Q. Shi, Z. Feng, Y. Yan, and Y. X. Wang, "Electronic structure and thermoelectric properties of Zintl compounds A_3AlSb_3 (A = Ca and Sr): first-principles study," *RSC Adv.*, vol. 5, no. 80, pp. 65133–65138, Jul. 2015, doi: 10.1039/C5RA09804A.

[54] J. Sun and D. J. Singh, "Thermoelectric properties of AMg_2X_2, AZn_2Sb_2 (A = Ca, Sr, Ba; X = Sb, Bi), and Ba_2ZnX_2 (X = Sb, Bi) Zintl compounds," *J. Mater. Chem. A*, vol. 5, no. 18, pp. 8499–8509, May 2017, doi: 10.1039/C6TA11234J.

[55] S. K. Mishra, S. Satpathy, and O. Jepsen, "Electronic structure and thermoelectric properties of bismuth telluride and bismuth selenide," *J. Phys. Condens. Matter*, vol. 9, pp. 461–470, Jan. 1997, doi: 10.1088/0953-8984/9/2/014.

GENERAL CONCLUSION

In this work, the equilibrium crystal structure, elastic modules and related properties, electronic structures, linear optical properties and thermoelectric properties of the ternary Zintl phases Sr_3GaAs_3, Ba_3GaAs_3 and dibarium zinc diphosphide (Ba_2ZnP_2) are studied using DFT-based first-principles calculations within the pseudopotential plane-wave (PP-PW) and the Full Potential-Linearized Augmented Plane Wave (FP-LAPW) method as implemented in the WIEN2k code and CASTEP package, with the Generalized Gradient Approximation by Perdew-Burke-Ernzerhof for solids (GGA-PBEsol) and Tran-Blaha modified Becke-Johnson (TB-mBJ) potential. The main obtained results can be summarized as follows:

1. **Structural properties**
   - The ternary Zintl-phase compounds Sr_3GaAs_3 and Ba_3GaAs_3 have an orthorhombic structure, space group *pnma* Ba_3GaSb_3-type structure (no. 62) and the ternary Zintl-phase dibarium zinc diphosphide compound Ba_2ZnP_2 has an orthorhombic structure, space group *Ibma* (no. 72)
   - The equilibrium lattice parameters, internal coordinates of atoms and bond lengths are in excellent agreement with experimental data for the title compounds, where the relative deviations between calculated lattice parameters (*a* and *c*) and the corresponding experimental ones are less than 1%.
2. **Electronic properties**
   - Sr_3GaAs_3 and Ba_3GaAs_3 are semiconductors, our calculation yielded a direct band gap located at the Γ point. The mBJ (GGA-PBEsol) fundamental bandgap value is equal to 1.271 eV (0.655 eV) for Sr_3GaAs_3 and 1.285 eV (0.572 eV) for Ba_3GaAs_3 between the valence band maximum and the conduction band minimum. Also, Ba_2ZnP_2 is a semiconductor with an indirect band gap located between T at VBM and X at CBM points of 1.24 and 0.57 eV for TB-mBJ and PBEsol, respectively.
   - The hole effective mass at the valence band maximum is heavier than that of the electron at the conduction band minimum and the hole effective mass along z-axis larger than the corresponding ones along a- and y-axes directions for Sr_3GaAs_3 Ba_3GaAs_3 and Ba_2ZnP_2 compounds.
   - The calculated band effective masses show a noticeable anisotropy of electronic properties.
   - The conduction bands, ranging from the CBM up, consists mainly of the *AE*-n*d* (Sr/Ba) states for AE_3GaAs_3 and the Ba-5d states for Ba_2ZnP_2. Hence, the 4d-Ba

electrons would play an important role in the electrical conductivity for the Ba_2ZnP_2 compound.

3. Elastic properties

- Sr_3GaAs_3 and Ba_3GaAs_3 compounds appear large resistant to versus the external stress along the [100] crystallographic direction comparing that along the other directions ([010] and [001]). Ba_2ZnP_2 compound appears large resistant against versus the external stress along the [001] and [010] crystallographic direction comparing that along the other directions [100].
- Based on Born and Huang mechanical stability criteria, Sr_3GaAs_3, Ba_3GaAs_3 and Ba_2ZnP_2 compounds are mechanically stable.
- Calculated value of universal index (A^U) for Sr_3GaAs_3 and Ba_3GaAs_3 compounds is equal to 0.037 and 0.158 respectively, denoting that Sr_3GaAs_3 is characterized by a feeble elastic anisotropy, whereas Ba_3GaAs_3 is characterized by a noticeable elastic anisotropy, so its degree increases when substitution *Strontium* by *Barium* atoms in A_3GaAs_3 system. For Ba_2ZnP_2 is equal to 0.35, denoting that is Ba_2ZnP_2 characterized by a noticeable elastic anisotropy.
- The computed B/G ratio values, Sr_3GaAs_3, Ba_3GaAs_3 equal to 1.58 and 1.66 indicating the brittle nature of the considered compounds. For Ba_2ZnP_2, B/G= 1.82, this result indicating the ductile nature of the considered compound.
- For the chemical bonding in title compounds, in Sr_3GaAs_3 and Ba_3GaAs_3 it is equal to 0.24 and 0.25. So, has a dominant covalent character. Poisson's ratio of Ba_2ZnP_2 is 0.27. So, the chemical bonding has a dominant ionic character.

4. Optical properties

- The imaginary part of the dielectric function; $\varepsilon_2(\omega)$, exhibits a well pronounced anisotropy in the energy range ~1.5 to ~7.5 eV and it is almost isotropic in the rest of the considered energy range for both AE_3GaAs_3. Ba_2ZnP_2 exhibits a well distinct anisotropy in the energy range 0-20 eV and it is nearly isotropic in the rest energy range for considered compound.
- The maximum magnitude of $\varepsilon_1(\omega)$ corresponding to $\boldsymbol{E}\|\boldsymbol{b}$ polarization is ~12.83 at ~1.84 eV for Sr_3GaAs_3 and ~13.00 at ~2.22 eV for Ba_3GaAs_3, The magnitude of ε^{zz} curve equal to 11.8 at 2.1 eV for Ba_2ZnP_2.
- AE_3GaAs_3 compounds have a band gap about 1.3 eV, so, the strong absorption of the electromagnetic wave occurs in the Near-UV region. Ba_2ZnP_2 has a high

absorptivity with direct proportion of the electromagnetic wave in the visible spectrum (1.6 to 3.1 eV) and Near-UV region (3.1 to 6.0 eV), suggests that these compounds are possible candidates for optoelectronic applications in the aforementioned energy ranges.

- The reflectivity coefficient R (ω) of AE_3GaAs_3 materials is characterized by an average value that these are reaches approximately 45% for a photon energy equal to ~6.5 eV. Whereas the static reflectivity coefficient R (0) has a value for a maximum of 0.26. The magnitude of *R*(ω) is higher than 23.5 (24.5) in an energy range 0–12.6 eV (0–9.6 eV) for Sr_3GaAs_3 (Ba_3GaAs_3), and *R*(ω) curve exhibits some maxima and humps in the aforementioned energy range. For photon energy higher than 12.5 (9.6 eV) for Sr_3GaAs_3 (Ba_3GaAs_3). The reflectivity coefficient R (ω) of Ba_2ZnP_2 is characterized by an average its values, where it reaches approximately ~ 44% for a photon energy equal to ~6.9 eV. Whereas the static reflectivity coefficient R (0) has a value for a maximum of 25% along [001] direction. The magnitude of *R*(ω) along [001] is higher than [100] and [010] directions, viz. it exhibits obvious anisotropy.

5. Thermoelectric properties.

- Seebeck coefficient, the power factor and the thermal conductivity have a directly proportional to the temperature at the same carrier concentration for all compounds.
- For the Seebeck coefficient efficiency, the effect of *p*-type doping at Ba_2ZnP_2 compound is slightly larger than *n*-type, because the hole effective mass is heavier than the electron effective mass.
- For the carrier concentration equal $10^{18}cm^{-3}$, Seebeck coefficient of *p*-type Sr_3GaAs_3 (Ba_3GaAs_3) equal to 560 μV/K (650 μV/K) at 300K. Meanwhile, Seebeck coefficient of *n*-type title compounds equal to 450 μV/K (540 μV/K) corresponding to same conditions. The efficient of *p*-type and *n*-type doped Ba_3GaAs_3 is more considerable than Sr_3GaAs_3 one. For Ba_2ZnP_2, at the carrier concentration equal to $10^{18}cm^{-3}$, Seebeck coefficient of *p*-type title compound equal to 720 μV/K at 900K. Meanwhile, Seebeck coefficient of *n*-type studied compound equal to 603 μV/K corresponding to same conditions.
- The maximum of figure of merit (ZT) for the *p*-type doped AE_3GaAs_3 compounds are slightly less than that of the *n*-type doped ones and the *p*-type and *n*-type doped

Ba_3GaAs_3 is often large than Sr_3GaAs_3 one. The figure of merit ZT reaches a maximum of 1.02 (1.00) for an electron concentration of 7×10^{18} (3×10^{16}) cm^{-3} of Ba_3GaAs_3 (Sr_3GaAs_3) compound at 900k. where the maximum of ZT for the *p*-type doped Ba_2ZnP_2 compound is greater than that of the *n*-type doped. The figure of merit ZT reaches a maximum of 1.77 for hole concentration of 8×10^{19} cm^{-3} at 300k. Also, can note figure of merit is large than 1 at considering concentration for 300, 600, 900 and 1200 k. while for *n*-type compound, ZT< 1.

- The minimum lattice thermal conductivity is calculated $k_{l,min}$ within Cahill's model for Ba_2ZnP_2 is equal to 0.53 W/m.K, which indicates that Ba_2ZnP_2 might be a good thermoelectric material. The lattice thermal conductivity within Slack's relationship become smaller than $\kappa_{l,min}$ of Cahill's model afterward ~900K.